

INFORMATION TO USERS

This manuscript has been reproduced from the microfilm master. UMI films the text directly from the original or copy submitted. Thus, some thesis and dissertation copies are in typewriter face, while others may be from any type of computer printer.

The quality of this reproduction is dependent upon the quality of the copy submitted. Broken or indistinct print, colored or poor quality illustrations and photographs, print bleedthrough, substandard margins, and improper alignment can adversely affect reproduction.

In the unlikely event that the author did not send UMI a complete manuscript and there are missing pages, these will be noted. Also, if unauthorized copyright material had to be removed, a note will indicate the deletion.

Oversize materials (e.g., maps, drawings, charts) are reproduced by sectioning the original, beginning at the upper left-hand corner and continuing from left to right in equal sections with small overlaps. Each original is also photographed in one exposure and is included in reduced form at the back of the book.

Photographs included in the original manuscript have been reproduced xerographically in this copy. Higher quality 6" x 9" black and white photographic prints are available for any photographs or illustrations appearing in this copy for an additional charge. Contact UMI directly to order.

UMI

A Bell & Howell Information Company
300 North Zeeb Road, Ann Arbor MI 48106-1346 USA
313/761-4700 800/521-0600

**Remote Sensing of Surface Albedo and Cloud Properties in the Arctic
from AVHRR Measurements**

A
THESIS

Presented to the Faculty
of the University of Alaska Fairbanks
in Partial Fulfillment of the Requirements
for the Degree of

DOCTOR OF PHILOSOPHY

By

Wei Han, B.S., M.S.

Fairbanks, Alaska

December 1996

UMI Number: 9701144

**UMI Microform 9701144
Copyright 1996, by UMI Company. All rights reserved.**

**This microform edition is protected against unauthorized
copying under Title 17, United States Code.**

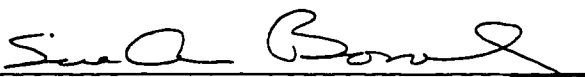
UMI
300 North Zeeb Road
Ann Arbor, MI 48103

Remote Sensing of Surface Albedo and Cloud Properties in the Arctic
from AVHRR Measurements

by

Wei Han

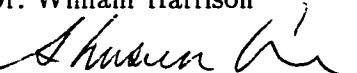
RECOMMENDED:



Dr. Sue Ann Bowling



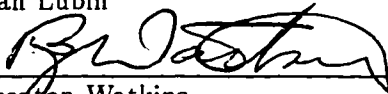
Dr. William Harrison



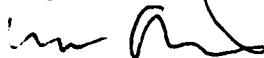
Dr. Shusun Li



Dr. Dan Lubin



Dr. Brenton Watkins



Dr. Knut Stamnes, Chairman, Advisory Committee



Dr. John Morack, Head, Physics Department

APPROVED:



Dr. Paul Reichardt, Dean, College of Natural Sciences



Dr. Joseph Kan, Dean of the Graduate School

4-4-96

Date

Abstract

Based on a comprehensive radiative transfer model, algorithms suitable for arctic conditions are developed to retrieve broadband surface albedo and water cloud properties from National Oceanic and Atmospheric Administration (NOAA) Advanced Very High Resolution Radiometer (AVHRR) narrowband measurements. Reflectance anisotropy of snow surfaces is first simulated by a discrete ordinates radiative transfer formulation, and is then included in the comprehensive model for the retrieval. Ground-based irradiance measurements made by NOAA Climate Monitoring and Diagnostics Laboratory (CMDL) in Barrow, Alaska are compared with retrieved albedo and downwelling irradiances computed from retrieved cloud optical depth and effective radius. The good agreement found between satellite estimates and ground-based measurements indicates that the retrieval algorithms proposed in this thesis are suitable for arctic conditions. It is found that the effects of snow bidirectional reflectance on the retrieval of the broadband albedo are significant, and that the Lambertian approximation could lead to a 30% underestimate of the surface albedo. It is also found that cloud effective radius in the Arctic is generally smaller as compared with mid- and low-latitudes.

Contents

Abstract	iii
List of Figures	vii
List of Tables	xv
Acknowledgments	xvi
1 Introduction	1
2 Background	7
2.1 Definitions	7
2.2 AVHRR Instrumentation	9
2.2.1 General Information	9
2.2.2 Calibration and Accuracy	11
2.2.3 Atmospheric Attenuation in AVHRR Channels	13
2.3 Instrumentation for Ground-based Irradiance Measurements	15
2.4 Previous Work on Remote Sensing of Surface Albedo	17
2.5 Previous work on Remote Sensing of Liquid Water Cloud Parameters	18

3	A Model Study on Bidirectional Reflectances	21
3.1	Radiative Transfer Equation	23
3.2	Hapke's Bidirectional Reflectance Model	26
3.3	Hapke's Treatment of the Opposition Effect	28
3.4	Generalization of Hapke's Model to Allow for Anisotropic Multiple Scattering	30
3.5	Computation of the Bidirectional Reflectance Based on the Discrete- Ordinate Radiative Transfer Code	31
3.6	Comparisons of Bidirectional Reflectance Derived from Hapke's and Our Models	33
3.7	Summary	39
4	Retrieval of Surface Albedo in the Arctic from AVHRR Clear-sky Measurements	43
4.1	Satellite and Field Data in the Arctic	45
4.2	Radiative Transfer Model	46
4.2.1	Arctic Haze	49
4.2.2	Stratospheric Aerosols	51
4.2.3	Tropospheric Aerosols	52
4.2.4	Boundary Conditions	54
4.3	Retrieval Procedures	57
4.4	Retrieval Results	62
4.4.1	Comparison of Satellite-inferred and Ground-based Results	62
4.4.2	Effect of Bidirectional Reflectance of Snow	66

4.5	Discussion	69
4.6	Summary	71
5	Remote Sensing of Water Cloud Parameters in the Arctic from AVHRR Measurements	73
5.1	The Principles of Cloud Remote Sensing	75
5.1.1	Radiative Transfer Model	75
5.1.2	Water Cloud over Ocean or Tundra	77
5.1.3	Water Cloud over Snow or Ice	81
5.2	Description of Retrieval Algorithm	84
5.2.1	Water Cloud over Ocean or Tundra	84
5.2.2	Water Cloud over Snow or Ice	90
5.3	Uncertainty Analysis	92
5.3.1	Uncertainty in the Retrieval of Optical Depth	92
5.3.2	Uncertainty in the Retrieval of Effective Radius	95
5.4	Applications and Results	98
5.4.1	Data	98
5.4.2	Testing	99
5.4.3	Retrieval Results	104
5.5	Summary	114
6	Summary and Discussion	119
	References	124

List of Figures

1.1	Interaction mechanisms between electromagnetic radiation and the atmosphere	4
2.1	Irradiance and radiance	8
2.2	AVHRR spectral response functions. [Adapted from <i>Kidwell</i> (1995)]	10
2.3	Atmospheric transmission in the visible and infrared regions. Gases responsible for atmospheric absorption are shown. [Adapted from <i>Sabins</i> (1987)]	14
3.1	(a) Geometry of a plane-parallel medium (top); (b) Reflection geometry (bottom). F^s is incident solar irradiance, I is reflected radiance, θ_0 is solar zenith angle, θ is viewing zenith angle, ϕ is relative azimuth angle between incident solar beam and viewing direction, and Θ is scattering angle	24

3.2	Computed bidirectional reflectances as a function of viewing angle θ in the principal plane for three different incident zenith angles and four different asymmetry factors. The solid lines are results computed by our model, and the dotted lines are those by Hapke's model. The single scattering albedo a is assumed to be 0.5, opposition effect parameters $S(0)$ to be 2.0, and h to be 0.6	34
3.3	Same format as Figure 3.2 but in the plane perpendicular to the principal plane	36
3.4	Same format as Figure 3.2 but for different single scattering albedo a . The asymmetry factor g is fixed as 0.6. The solar zenith angle θ_0 is assumed to be 40° . The opposition effect is not included	37
3.5	Same as Figure 3.4 but in the plane perpendicular to the principal plane. The opposition effect is not included	38
3.6	Deviations on bidirectional reflectance between our model and Hapke's model as a function of viewing angle in the principal plane for various asymmetry factors and single scattering albedos. Solar zenith angle θ_0 is assumed to be 60° , opposition effect parameters $S(0)$ to be 2.0, and h to be 0.6	40

4.1	The wavelength dependence of the extinction coefficient, single scattering albedo and asymmetry factor in the solar spectral region for Arctic haze at 70% relative humidity (solid line) from <i>Tsay et al.</i> 's (1989) parameterizations, fresh volcanic ash (dotted line) and tropospheric aerosol at 70% relative humidity (dashed line) from the <i>Shettle and Fenn</i> (1976) models. Note that the extinction coefficient shown is the value at 2 km for Arctic haze, at 19 km for volcanic ash and at 4 km for tropospheric aerosol, where the extinction coefficient reaches the maximum	50
4.2	The particulate extinction coefficient profile at 0.5 μm from the <i>Shettle and Fenn</i> (1976) models and <i>Tsay et al.</i> 's (1989) parameterizations. The solid line represents summer conditions and the dashed line spring conditions	53
4.3	Contour plots of simulated bidirectional anisotropy factor in AVHRR Channel 1 (for $\theta_0 = 70^\circ$) at (a) snow surface without atmosphere, (b) the TOA over snow surface for clear-sky conditions in the absence of haze, and (c) the TOA over snow surface for clear-sky conditions in the presence of haze with optical depth 0.16. Snow grain size is 200 μm	56
4.4	Flow chart of retrieval algorithm for tundra surface	59

4.5	Simulation of reflected solar radiances in AVHRR channel 1 as a function of the mass-fraction of soot and snow grain size with the condition of solar zenith angle $\theta_0=60^\circ$, satellite zenith angle $\theta =10^\circ$, relative azimuth angle between the Sun and the satellite $\phi =50^\circ$ and 5.74 cross-section area per unit mass for soot	60
4.6	Simulation of reflected solar radiances in AVHRR channel 2 as a function of the mass-fraction of soot and snow grain size with the condition of solar zenith angle $\theta_0=60^\circ$, satellite zenith angle $\theta =10^\circ$, relative azimuth angle between the Sun and the satellite $\phi =50^\circ$ and 5.74 cross-section area per unit mass for soot	61
4.7	Flow chart of retrieval algorithm for snow surface	63
4.8	Scatter plots of satellite estimates versus ground-based CMDL measurements for (a) albedo, (b) upward irradiance, (c) downward irradiance, and (d) net irradiance at Earth surface for all 19 cloud-free cases (tundra and snow)	64
4.9	Scatter plots of satellite estimates versus CMDL field measurements for (a) albedo, (b) upward irradiance, (c) downward irradiance, and (d) net irradiance at Earth surface for snow with bidirectional reflectances (solid point) and with Lambertian assumption (circle) . .	67

5.1	Reflected radiance for (a) AVHRR channel 1, and (b) AVHRR channel 3 for various effective radius as a function of cloud optical depth. Calculations are for the azimuth angle of $\phi=50^\circ$, satellite zenith angle $\theta=10^\circ$ and solar zenith angle $\theta_0=60^\circ$, respectively. Lambertian visible surface albedo is 0.1	78
5.2	Simulated radiances of AVHRR channel 3 as a function of cloud optical depth in the case of (1) no thermal radiation, (2) with ground thermal radiation, (3) with cloud thermal radiation, and (4) with both ground and cloud thermal radiation, for a surface temperature $T_g=288.2$ K, cloud top temperature $T_c=275.2$ K, and surface albedo $A_g=0.0$	80
5.3	Brightness temperature of AVHRR channel 4 for various cloud top temperature and effective radius as a function of cloud optical depth for a surface temperature of 273 K (lower panel) and 283 K (upper panel)	82
5.4	Simulated radiances of AVHRR channel 1 as a function of cloud optical depth and surface albedo A_g	83
5.5	Reflected radiance for (a) AVHRR channel 2, and (b) AVHRR channel 3 for various effective radius as a function of cloud optical depth. Calculations are for the azimuth angle of $\phi=50^\circ$, satellite zenith angle $\theta=10^\circ$ and solar zenith angle $\theta_0=70^\circ$, respectively. Snow grain size is assumed to be $100 \mu\text{m}$ which corresponds to a surface visible albedo of 0.95	85

5.6	Reflected radiance in AVHRR channel 2 as a function of cloud optical depth. Calculations are for the azimuth angle of $\phi=50^\circ$, satellite zenith angle $\theta=10^\circ$ and solar zenith angle $\theta_0=70^\circ$, respectively. Snow grain size is assumed to be $100 \mu\text{m}$ which corresponds to a surface albedo of 0.87 in AVHRR channel 2. Solid line represents the calculations from the model that accounts for bidirectional reflectance of snow, and dotted line represents the calculations from the model that assumes Lambertian reflector for snow. Cloud effective radius is $8 \mu\text{m}$	86
5.7	Flow chart of retrieval algorithm for water cloud over ocean and tundra. Note that A_g is fixed to be 0.06 for ocean	89
5.8	Flow chart of retrieval algorithm for water cloud over snow and ice	91
5.9	Error in retrieval of cloud optical depth over ocean and tundra as a function of optical depth for an uncertainty in surface albedo of 0.06 ± 0.04 (upper panel), and a $\pm 5 \%$ or $\pm 10 \%$ error in measured AVHRR channel 1 cloud radiance (lower panel)	94
5.10	Error in retrieval of cloud optical depth over snow and ice as a function of optical depth for an uncertainty in snow/ice grain size of $1000 \pm 100 \mu\text{m}$ (upper panel), and a $\pm 2 \%$ and $\pm 4 \%$ error in measured AVHRR channel 2 cloud radiance (lower panel)	96

5.11	Cloud properties are retrieved in three different areas of $1^\circ \times 1^\circ$ each. Areas I, II, and III have ocean, snow/ice, and tundra as their underlying surface, respectively. The black point indicates the location of Barrow, Alaska where ground observations are made and the data are used for validation	100
5.12	Scatter plot of satellite estimates versus ground-based CMDL measurements for solar downwelling irradiance over tundra. The satellite estimates of solar irradiance use the retrieved cloud parameters as input	102
5.13	Same as Figure 5.12 but for clouds over snow	103
5.14	Profiles of temperature (solid line in the left panel), dew point temperature (triple-dot line in the left panel), and relative humidity (solid line in the right panel) at 0000 UTC 24 September 1992. The dashed line indicates the cloud top obtained from temperature inversion and relative humidity variation. The black point indicates the cloud top temperature obtained from the satellite estimate . . .	105
5.15	Scatter plot of satellite estimates versus ground-based sounding results for cloud top temperature	106
5.16	Derived images of cloud optical depth, effective radius (in μm), and cloud top temperature (in K) for area I as shown in Figure 5.11. The three images are derived from a cloudy image at 0013 UTC 23 July 1992. The underlying surface is ocean	107

5.17	Derived images of snow grain size in (μm), cloud optical depth, effective radius (in μm), and cloud top temperature (in K) for area I as shown in Figure 5.11. The snow grain size is derived from a clear-sky satellite image at 2313 UTC 27 July 1992. The remaining three images are derived from a cloudy images at 0013 UTC 23 July 1992. The underlying surface is snow/ice. The black areas in the plots of optical depth, effective radius and top temperature represent clear sky	110
5.18	Same as Figure 5.16 except it is for area III with tundra as underlying surface and the upper-left panel represents surface albedo in channel 1	111
5.19	Scatter plots of retrieved cloud effective radius versus optical depth for areas I, II, and III with ocean (middle), snow (lower), and tundra (upper) as underlying surfaces, respectively	113
5.20	Frequency distributions of cloud effective radius (in μm) based on the data shown in Figure 5.15-5.17 for tundra, ocean, and snow as underlying surfaces, respectively	115

List of Tables

2.1	Spectral band widths (μm) of the AVHRR	9
4.1	Observing conditions of AVHRR measurements	47

Acknowledgments

I would like to thank Professor Knut Stamnes, my thesis advisor in the University of Alaska, Fairbanks. His continuous advice and encouragement made the completion of this thesis possible. I am grateful for this opportunity to work with him. My sincere appreciation also goes to other members of my graduate advisory committee: Professors Shusun Li, Dan Lubin, Sue Ann Bowling, William Harrison, and Brenton Watkins. Their concerns and helpful suggestions improved my research work and the quality of my thesis.

I would also like to thank everybody in our group (T. Zhang, Elena, Jin, Fan, Rune, Hans, Mike, ...) for helpful discussions; Dr. Si-Chee Tsay and Dr. Jeffrey Key with whom I have had many stimulating and inspiring conversations and e-mails; Robert Whritner and Elizabeth Nelson for their work on AVHRR data collection and processing.

Finally, I would like to thank my husband Dr. Ming Yan, whose love and support encouraged me to finish this thesis.

This thesis work was supported by the National Science Foundation through Grant OPP91-140010 to the University of Alaska, by the Environmental Sciences Division of the U.S. Department of Energy under contract 091574-A-QL to the University of Alaska as part of the Atmospheric Radiation Measurement Program, and by the Center for Global Change and Arctic System Research of University of Alaska through a student research grant.

Chapter 1

Introduction

It is well known that clouds strongly modulate the energy balance of the Earth-atmosphere system through their interaction with solar and terrestrial radiation. Clouds reflect part of the solar energy back to space and thus have a cooling effect on the Earth-atmosphere system. On the other hand, clouds can also have a greenhouse effect. They absorb part of the longwave radiation from the Earth's surface, re-emit about half of the absorbed energy back to the Earth's surface and thus warm the Earth's surface and lower atmosphere. The polar regions constitute a radiative energy sink whereas the equatorial region is a source. The persistent presence of snow/ice cover in the Arctic may change the cooling effect of clouds to a slight heating due to the generally higher albedo of snow/ice as compared with clouds (*Tsay et al.*, 1989).

Surface albedo controls the amount of incident solar energy absorbed by the ground surface. While remaining high for much of the year, the surface albedo in the Arctic decreases dramatically during the spring and summer and becomes

highly variable both spatially and temporally.

Surface albedo and cloud properties are of great interest for understanding the global radiation budget and climate change. The arctic region has received more and more attention by climate researchers because it is believed to be particularly sensitive to climate change due to greenhouse warming.

However, the spatial coverage of ground-based radiation measurements in the arctic is sparse as compared with mid- and low-latitudes. Cloud measurements by aircraft are also sparse. With their considerable spatial and temporal variability, clouds are among the most difficult components of the climate system to study. Satellite-borne sensors, on the other hand, can, at least in principle, provide continuous and global measurements with high temporal and spatial resolution.

The Earth's lower atmosphere is composed of gas molecules, cloud droplets and aerosol particles. The interaction between solar radiation and the Earth-atmosphere system includes absorption, scattering, and reflection. Figure 1.1 illustrates the most important physical processes occurring when solar radiation interacts with the Earth-atmosphere system. The radiation from the Sun is partly absorbed by aerosols, clouds, and molecules (mainly H_2O and O_3), on its way through the atmosphere. Part of the solar radiation is scattered back to space by clouds, aerosols and molecules in the atmosphere. The rest of the solar radiation reaches the Earth surface. The surface absorbs part of the incident energy and reflects the remainder. The solar radiation reflected by the surface also interacts with the molecules, cloud droplets and aerosol particles in the atmosphere which transmits a fraction of it to space, reflects another fraction of it back to the surface, and absorbs the remaining portion. The Earth surface emits thermal radiation,

which is partly absorbed by molecules, mainly H_2O , CO_2 , and O_3 , and partly scattered and absorbed by cloud droplets and aerosol particles before it reaches the top of the atmosphere. Clouds, aerosols and molecules in the atmosphere also absorb and emit thermal radiation.

Satellites sensors detect a combination of radiation emitted and reflected from the surface of the earth and transmitted by the atmosphere, as well as radiation emitted by the atmosphere or scattered into the field of view of the satellite sensor by particles and molecules in the atmosphere. The task is to determine what part of the radiation comes from the ground and what part comes from various regions in the atmosphere, and to use this information to deduce surface and atmospheric conditions from satellite measurements.

The above physical processes of absorption, emission and scattering determine the transport of radiation throughout the Earth-atmosphere system. This transport of solar and terrestrial radiation is described quantitatively by the radiative transfer equation. The radiance measured by satellite sensors can be used in conjunction with radiative transfer calculations to infer some important features of the underlying surface and cloud particles.

Based upon radiative transfer theory, the purpose of this thesis is to study the reflectance anisotropy of snow surfaces under arctic conditions, and further to develop retrieval algorithms, suitable for arctic conditions, to infer surface albedo and water cloud properties from Advanced Very High Resolution Radiometer (AVHRR) measurements. The retrieved results are tested against ground-based field measurements.

Rather than relying on the Lambertian (isotropic) approximation which is com-

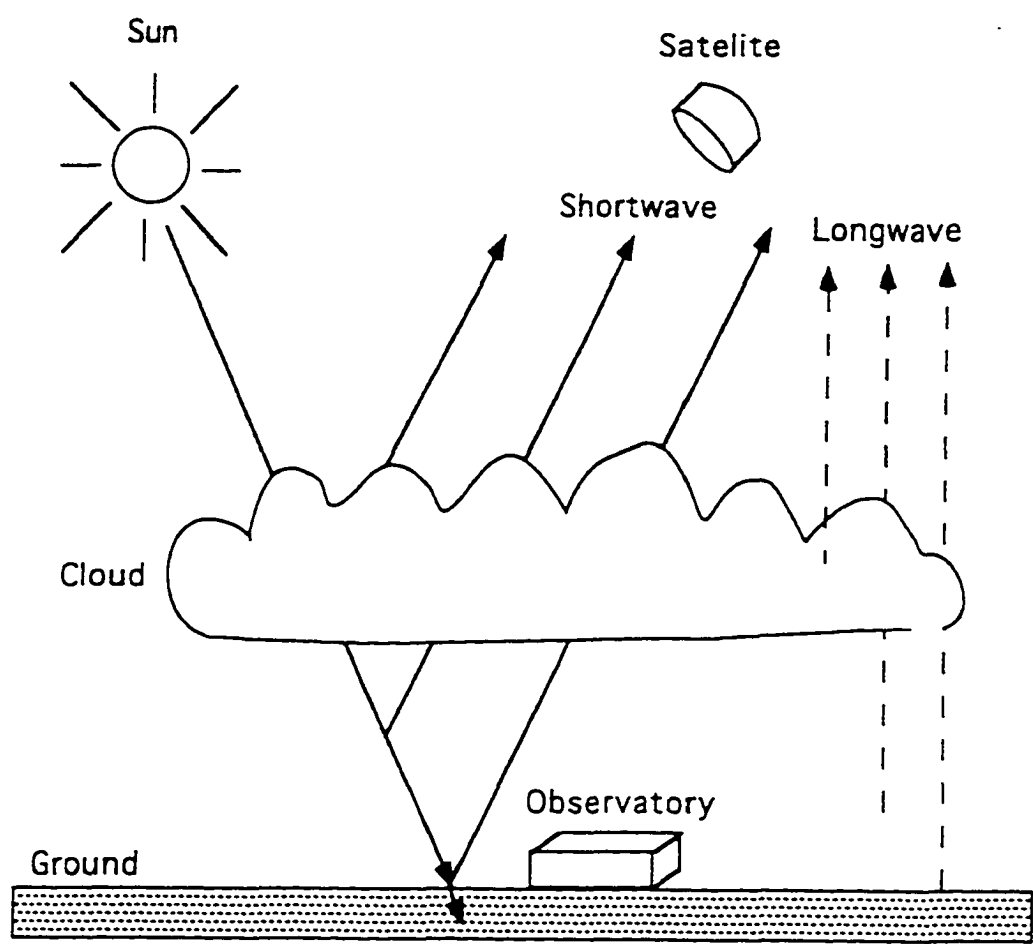


Figure 1.1 Interaction mechanisms between electromagnetic radiation and the atmosphere.

monly used in the remote sensing of surface and cloud properties from satellite measurements, the bidirectional reflectance of snow is taken into account in this thesis, based on Mie theory which assumes (1) spherical snow particles and (2) well separated snow particles. Although these assumptions may not be representative of natural snow surfaces on some occasions, the retrieval results show that this snow model offers a clear advantage over the Lambertian approximation.

In chapter 2, background information is briefly reviewed, including AVHRR instrumentation, field irradiance measurements, and existing knowledge about remote sensing of surface albedo and water cloud parameters.

In chapter 3, an improved physical model is developed to compute bidirectional reflectance based on the radiative transfer code DISORT (DIScrete Ordinate Radiative Transfer), which precisely accounts for multiple scattering processes. A comparison is made between it and Hapke's model which relies on a simplified treatment of multiple scattering. The results show that the improved model performs much better than Hapke's model for media with large single scattering albedo and asymmetry factor.

In chapter 4, an algorithm is developed to infer broadband surface albedo using NOAA AVHRR channel 1 and 2 measurements over arctic snow and tundra under cloud-free conditions. This algorithm obviates the need for "anisotropic corrections" which are also commonly used for retrieval of the surface albedo from AVHRR data. Comparisons of satellite-retrieved surface albedo, upward, downward and net irradiance with ground-based field measurements made by NOAA CMDL in Barrow, Alaska show good agreement. It is also found that the Lambertian approximation can lead to an underestimation of surface albedo by as much

as 30 %.

In chapter 5, algorithms are developed to retrieve visible optical depth, effective radius and cloud top temperature for liquid water clouds in the Arctic using NOAA AVHRR images obtained under overcast conditions. For water clouds over dark surfaces (tundra and ocean), channel 1 ($0.64 \mu\text{m}$), channel 3 ($3.75 \mu\text{m}$) and channel 4 ($11 \mu\text{m}$) are used. For water cloud over bright surfaces (snow and ice), the reflectance in channel 1 is not sensitive to cloud optical depth due to the multiple reflection between cloud base and the underlying surface, so that channel 2 ($0.85 \mu\text{m}$) is used, together with channel 3 and 4 to infer cloud optical depth, effective radius and cloud top temperature. As shown in chapter 5, the snow model adopted in this thesis does not yield multiple solutions as the Lambertian approximation does at large solar zenith angles. Downwelling irradiances at the surface computed using the retrieved cloud optical depth and effective radius agree well with field irradiance measurements.

Finally, a summary of the thesis is given in chapter 6.

Chapter 2

Background

In this chapter, the definitions used in discussions of radiation, AVHRR instrumentation, field irradiance measurements, and existing knowledge about remote sensing of surface albedo and water cloud parameters will be briefly reviewed.

2.1 Definitions

In a radiation field where the light is uncollimated, the amount of power at position \mathbf{r} crossing unit area perpendicular to the direction of propagation Ω , traveling into unit solid angle about Ω , is called the *radiance* and will be denoted by $I(\mathbf{r}, \Omega)$. Radiance is often also called *specific intensity*, or simply *intensity*, or *brightness*. Note the difference between *irradiance* F , which refers to power per unit area of a beam, and *radiance* I , which is the power per unit area per solid angle (Figure 2.1). F is simply a flow of energy, and it may or may not have an implied direction. Irradiance F is given by the integration of the normal component of radiance

$I(\mathbf{r}, \Omega)$ over the entire solid angle Ω

$$F = \int I(\mathbf{r}, \Omega) \cos(\theta) d\Omega \quad (2.1)$$

where θ is the zenith angle of the beam, which is the angle between the normal direction of the area and the beam. For an isotropic (Lambertian) radiation field, I is independent of angle Ω , so that $F = \pi I$. Satellite sensors measure reflected or emitted radiances (I) by Earth-atmosphere system. The ground based instruments, described in section 2.3 measure irradiances (F).

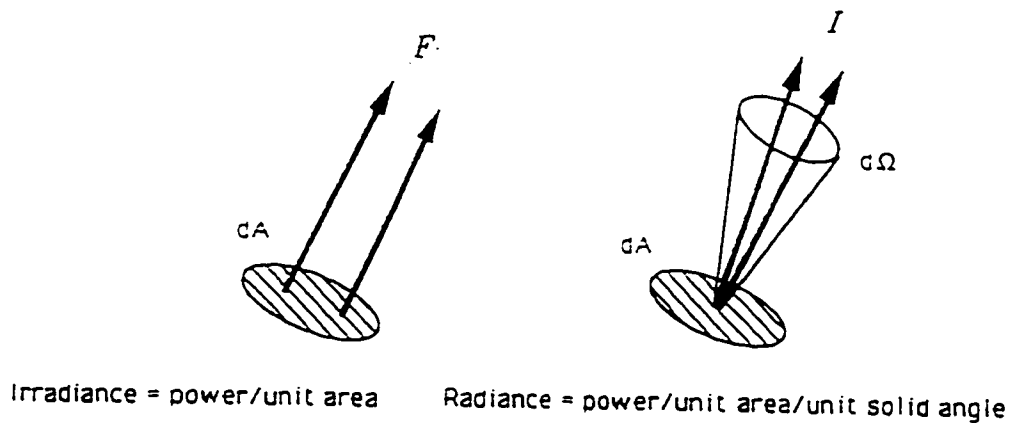


Figure 2.1 Irradiance and radiance.

Table 2.1 Spectral band widths (μm) of the AVHRR .

Channel	NOAA-6, -8, -10	NOAA-7, -9, -11, -12, -14	IFOV (mr)
1	0.58-0.68	0.58-0.68	1.39
2	0.725-1.10	0.725-1.10	1.41
3	3.55-3.93	3.55-3.93	1.51
4	10.5-11.5	10.3-11.3	1.41
5	10.5-11.5	11.5-12.5	1.30

2.2 AVHRR Instrumentation

2.2.1 General Information

Since 1978, regular satellite coverage of the polar regions has been provided by the National Oceanic and Atmospheric Administration (NOAA) polar orbiters equipped with AVHRR instruments. The NOAA series satellites were designed to operate in a near-polar, sun-synchronous orbit (with an inclination of around 99°). The orbital period is about 102 minutes which produces 14.1 orbits per day. The sub-orbital tracks do not repeat on a daily basis because the number of orbits per day is not an integer, while the satellite passes at the same local solar time for any latitude.

The AVHRR is a cross-track scanning system, featuring four or five channels. The spectral band widths (in μm) of the AVHRR channels are shown in Table 2.1. In addition, the Instantaneous Field of View (IFOV) in milliradians is included for each channel in Table 2.1. According to Table 2.1, the IFOV of each channel is approximately 1.4 milliradians leading to a resolution at the satellite subpoint

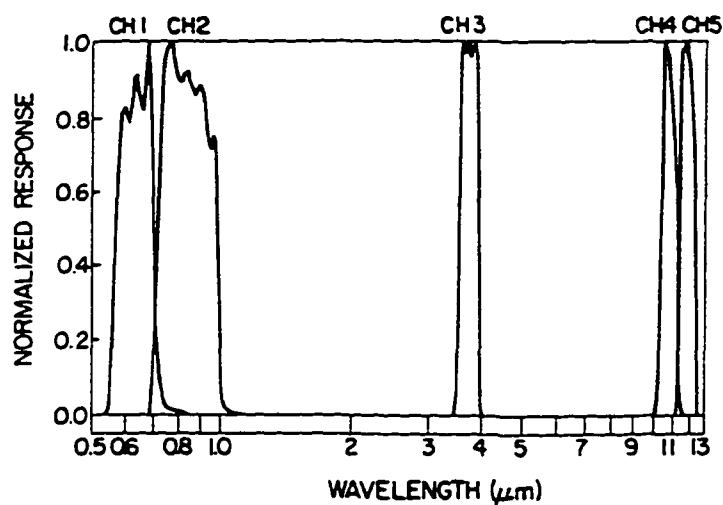


Figure 2.2 AVHRR spectral response functions. [Adapted from *Kidwell* (1995)].

of 1.1 km for a nominal altitude of 833 km. The spectral response functions for NOAA-9 AVHRR are shown in Figure 2.2. The two-wavelength descriptions in Table 2.1 indicate the range of wavelengths to which a radiometer is sensitive. By convention, these wavelengths are specified by the half-power points of the response functions.

All meteorological data on the NOAA series satellites are continually broadcast to Earth. These direct broadcasts are called high-resolution picture transmission (HRPT). In addition to the HRPT mode, about ten minutes of data may be selectively recorded on each of two recorders on board the satellite for later playback. These recorded data are referred to as LAC (Local Area Coverage) data. LAC and

HRPT data have identical formats. The full resolution data is also processed on board the satellite into GAC (Global Area Coverage) data. GAC data contains only one out of three original AVHRR lines and the data volume and resolution are further reduced by averaging every four adjacent samples and skipping the fifth sample along the scan line. HRPT data are used in this thesis. They are archived digitally at the Arctic and Antarctic Research Center (AARC) at the Scripps Institution of Oceanography, and processed by the TeraScan software (SeaSpace, Inc.) installed at the Alaska Data Visualization and Analysis Laboratory.

More details on the AVHRR instrumentation are given by *Kidwell* (1995).

2.2.2 Calibration and Accuracy

AVHRR channel 1 and 2 are calibrated in the laboratory before launch by comparison with a known input. Twelve matched, quartz-iodide lamps, which emit known radiance, are used. By turning on combinations of the lamps, a plot of radiance versus output digital count is constructed for each channel. The slope S_i and intercept L_i of the straight line that best fits this plot is used to linearly convert digital counts C returned by the satellite into albedo (percent) A_i at the top of the atmosphere

$$A_i = S_i C + L_i. \quad (2.2)$$

A spectrally averaged radiance can be calculated by

$$I = A \frac{F}{100\pi W} \quad (2.3)$$

where F is integrated solar spectral irradiance, weighted by the spectral response function of the channel, and W is equivalent width of the spectral response func-

tion. Until now, there are no on-board calibration capabilities. There is evidence that pre-launch calibration coefficients (the slope S_i and intercept L_i in equation (2.2)) of the AVHRR visible (channel 1) and near-infrared (channel 2) channels have changed in orbit. Many attempts have been made to estimate the degradation rates through ground-based experimental techniques (*Brest and Rossow, 1992; Kaufman and Holben, 1993; Rao and Chen, 1995*). As part of NASA's AVHRR Pathfinder program, investigations of Rao and Chen indicated that the relative annual degradation rates for the two channels are 1.2 % and 2.0 % (NOAA-11), respectively.

AVHRR channel 3, 4, and 5 are calibrated in flight by viewing hot and cold objects. During each rotation of a mirror, a telescope views both cold space and the instrument housing, which is painted black and equipped with platinum resistance thermometers to accurately measure the housing temperature (roughly 290 K). The radiance of the instrument housing (calculated from its measured temperature) plus the digital counts for the housing and for space (essentially zero radiance) allow digital counts for Earth scenes to be linearly converted to radiance (*Lauritson et al., 1979*). The equivalent blackbody temperature of the scene can then be determined from the Planck function. Due to instrument aging and the variation of thermal environment in the orbit, the linearity of response may change slightly. To account for nonlinearities, NOAA National Environmental Satellite, Data, and Information Service (NESDIS) provides corrections in channel 4 and 5 using a quadratic function of radiance.

NOAA specifications for AVHRR channels 3-5 require the equivalent blackbody temperature of a 300 K scene to be determined within ± 0.12 K. This is equivalent

to radiance errors of 2.1, 16.9, and 14.6 $mWm^{-2}sr^{-1}\mu m^{-1}$ at 3.7, 11, and 12 μm , respectively. Because the sensors measure radiance, the radiance error for each channel is approximately constant. The temperature error, however, varies with scene temperature as specified by the Planck function. At 250 K, for example, the temperature error will be approximately 1.1, 0.20, and 0.18 K at 3.7, 11, and 12 μm , respectively.

2.2.3 Atmospheric Attenuation in AVHRR Channels

The interaction of electromagnetic waves with the atmosphere involves different processes in different spectral regions. The scattering by particles which are small compared with the wavelength of the light is called Rayleigh scattering. Rayleigh scattering by molecules depends inversely on the fourth power of the wavelength and is therefore important for solar radiation ($\lambda < 3.5 \mu m$), but negligible for thermal infrared radiation ($\lambda > 3.5 \mu m$). When the scattering particle is comparable to or larger than the wavelength of the light, a diffraction peak is formed in the forward direction. In this case, the interaction of light with the particle is described in terms of Maxwell's equations. Solutions to Maxwell's equation for the electromagnetic wave interacting with a spherical dielectric particle is usually referred to as Mie Scattering. Scattering of solar radiation by aerosols and cloud droplets is characterized by strong forward scattering.

Figure 2.3 illustrates a diagram of atmospheric transmission in the visible and infrared regions. Gases responsible for atmospheric absorption are also shown in Figure 2.3. In AVHRR channel 1 and 2, absorption by H_2O , CO_2 , O_2 , and O_3

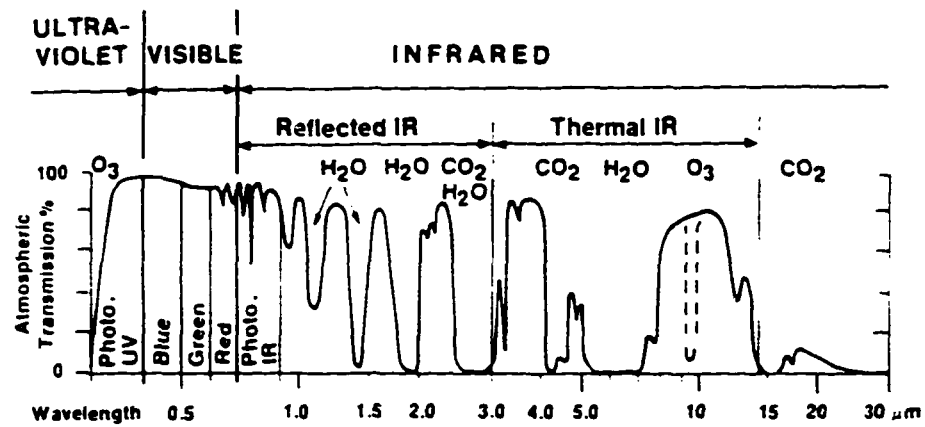


Figure 2.3 Atmospheric transmission in the visible and infrared regions. Gases responsible for atmospheric absorption are shown. [Adapted from *Sabins* (1987)].

are weak, while Rayleigh scattering by molecules and Mie scattering by aerosols are significant. For channel 3 water vapor line absorption is the principal mechanism but several minor constituents, notably CO_2 as well as the water vapor continuum, also have a significant effect on the attenuation of solar radiation. Mie scattering by aerosols is highly variable depending on the turbidity of the atmosphere. AVHRR channel 4 and 5 are located within an atmospheric window where the atmospheric transmittance is high. The water vapor continuum absorption is the main absorption mechanism. Rayleigh Scattering by molecules is negligible in channel 4 and 5. CO_2 has a significant absorption band in channel 4.

2.3 Instrumentation for Ground-based Irradiance Measurements

Surface solar radiation measurements in Barrow, Alaska ($71^{\circ}18' N$, $156^{\circ}47' W$) provided by the NOAA Climate Monitoring and Diagnostics Laboratory (CMDL) are utilized in this thesis for the testing of satellite-inferred albedo and irradiance at the surface. Broadband solar radiation measurements by Eppley pyranometers, covering the wavelength range $0.3 - 2.8 \mu m$, include upward and downward global solar irradiances. The thermopile detector of the Eppley pyranometer is made from a coiled constantan wire which is partially plated with copper to produce a set of junctions. Half of the junctions are thermally connected to the blackened detector surface and half to the instrument body which acts as a heat sink. The detector is covered with a double glass dome arrangement which serves two pur-

poses. Firstly it protects the surface of the thermopile, and secondly it defines the operating wavelength range. The inner dome improves the stability of the instrument by reducing the longwave radiation exchange between the outer dome and the thermopile. A removable dessicant holder contains silica gel to keep the inside of the instrument dry, thus avoiding condensation on the inside of the dome.

The sensitivity of the thermopile is temperature-dependent and the manufacturers incorporate a thermistor-resistor compensation circuit. According to the Eppley data this reduces the variation to better than ± 1 % for the sink temperature range 233 K to 303 K.

The decrease of sensitivity for clear sky downwelling radiation with the angle of incidence of direct radiation on the pyranometer is well known from laboratory measurements (e.g. *Foot et al.*, 1986). Differences of up to 10 % arise for zenith angle of 80° but are $< 2\%$ for zenith angle of $< 60^\circ$. A variation in sensitivity with azimuth angle exists in the instrument because its sensitivity is not isotropic. Ground-based laboratory measurements have shown the effect to be less than 1 % for $\theta < 60^\circ$. All these effects become negligible in conditions of diffuse illumination which applies to upwelling radiative irradiance measurements and downwelling irradiance measurements under an overcast sky. An annual calibration is necessary to measure any significant changes in zenith angle and azimuth angle dependences of the sensitivity under clear skies.

A recent estimate of the accuracy of the shortwave irradiance measurements is 2% according to *Saunders et al.* (1991).

2.4 Previous Work on Remote Sensing of Surface Albedo

Previous investigators have developed techniques for retrieving surface albedo and solar irradiances from satellite-measured radiances (e.g. *Saunders*, 1990; *Stuhlmann and Bauer*, 1991; *Pinker and Laszlo*, 1992; *De Abreu et al.*, 1994). Most of this work, however, has concentrated on lower latitudes. On the other hand, most methods (*Pinker and Laszlo*, 1992; *Stuhlmann and Bauer*, 1991; *De Abreu et al.*, 1994) apply an “anisotropic correction” to TOA bidirectional reflectance to account for target-Sun-satellite geometry. The anisotropic correction depends on solar zenith angle, satellite zenith angle, and relative azimuth angle between the Sun and the satellite. This is usually done by multiplying the TOA albedo obtained by assuming that the reflected radiation is isotropic, with an anisotropic correction factor. *Taylor and Stowe* (1984) determined anisotropic correction factors for the TOA reflectances over various surface types, using broadband NIMBUS 7 Earth Radiation Budget (ERB) data. The investigation by *De Abreu et al.* (1994) revealed that estimated visible and near-infrared AVHRR albedo values at the TOA derived from *Taylor and Stowe’s* (1984) anisotropic coefficients are about 25 % larger than those derived under the assumption that the TOA radiation field is isotropic over snow-covered sea ice in the Arctic. This study also indicated that the accuracy of surface albedo values derived from AVHRR data is very sensitive to the anisotropic coefficient employed. However, it is difficult to assess the accuracy of *Taylor and Stowe’s* (1984) anisotropic coefficients. Besides the anisotropic cor-

rection, it is also customary to assume that the underlying surface is a Lambertian (isotropic) reflector (*Stuhlmann and Bauer, 1991*).

2.5 Previous work on Remote Sensing of Liquid Water Cloud Parameters

Liquid water path (LWP), effective particle radius and cloud top temperature are three important parameters for liquid water clouds. In the visible the optical depth is proportional to the ratio of the liquid water content, LWC, and the effective radius. Thus, knowledge of LWC and effective radius allows us to infer the optical depth. Optical properties of water clouds depend almost exclusively on their liquid water path and effective radius (*Hu and Stamnes, 1993*). In addition, outgoing longwave radiation is mainly determined by the temperature at cloud top.

The climatic effects of clouds are difficult to estimate due to their temporal and spatial variability. Cloud microphysical properties are usually measured through field experiments. Satellite remote sensing techniques are also needed for a global knowledge of these parameters. Field experiments can provide necessary tests of the satellite retrieval algorithms. Several investigators have attempted to determine cloud optical depth and effective particle radius from visible and near-infrared measurements using radiometer deployed on aircraft (*Hansen and Pollack, 1970; Twomey and Cocks, 1982, 1989; King, 1987; Foot, 1988; Rawlins and Foot, 1990; Nakajima and King, 1990; Nakajima et al., 1991*) and satellites, such as AVHRR onboard the NOAA polar orbitors (*Curran and Wu, 1982; Arking and Childs, 1985;*

Durkee, 1989; Rossow et al., 1989; Platnick and Twomey, 1994; Han et al., 1994; Nakajima and Nakajima, 1995; and Platnick and Valero, 1995). The principle behind these techniques is based on the fact that the reflection function of clouds at a nonabsorbing channel in the visible wavelength range is primarily a function of the cloud optical depth, whereas the reflection function at a water absorbing channel in the near-infrared is primarily a function of cloud droplet size. The channel at $3.7 \mu\text{m}$ on AVHRR is ideal for inferring cloud particle size because the water absorption is greater as compared with shorter near-infrared wavelengths, although the thermal component at this channel has to be taken into account. However, AVHRR becomes more and more popular due to its long-time availability.

A number of field observations of clouds, aerosols, and radiation have been conducted since 1986, such as FIRE-I/II Cirrus (First ISCCP Regional Experiments, 1986 and 1991, respectively), ASTEX (Atlantic Stratocumulus Transition Experiment, 1992). Most of these cloud retrieval algorithms and field experiments, however, have focused on low- and mid-latitudes. To date only a few studies have been carried out for high latitudes. Field observations include the Arctic Stratus Cloud Experiment (1980), Leads Experiment (LEADDEX) in the Beaufort Sea north of Alaska during April 1992, Beaufort and Arctic Storms Experiment (BASE), and the Arctic Radiation Measurements in Column Atmosphere-surface System (ARMCAS) conducted on the North Slope of Alaska and over the Beaufort Sea area during June, 1995.

At high latitudes, the surface is covered by snow/ice most of the time throughout a year. Solar elevation is low so that the solar zenith angle is generally greater than 50° . Precipitation is mainly in the form of snow, which implies that the atmo-

spheric humidity is low. Temperature inversions occur over snow/ice surfaces even in summertime. Solar radiation reflected by clouds in the visible is not sensitive to cloud optical depth for clouds overlying snow/ice surfaces because of the low contrast between cloud and surface albedo, and the multiple reflections between cloud base and the underlying snow/ice surface.

Key (1995) used the AVHRR near-infrared channel 2 ($0.85 \mu\text{m}$) to infer water cloud optical depth for clouds over snow/ice surfaces, based on the premise that the reflected solar radiation at $0.85 \mu\text{m}$ is primarily a function of water cloud optical depth which is nearly independent on wavelength in the visible and near-infrared regions. Because of the weak wavelength dependence, the value of cloud optical depth inferred from channel 2 is almost the same as that inferred in the visible. The Lambertian approximation is adopted for snow surfaces under cloudy conditions in *Key's* (1995) algorithm. *Key* (1995) found that multiple solutions occur at small optical depths and large solar zenith angles. This method was applied to AVHRR images over the Beaufort Sea in the Arctic. The reflected solar radiation at channel 3 ($3.7 \mu\text{m}$) was used by *Key* (1995) to retrieve cloud effective radius over snow/ice surfaces, while the thermal component at channel 3 was removed by using the measurement of channel 4. *Lubin et al.* (1994) proposed an empirical parameterization for cloud optical depth as a function of the brightness temperature difference between AVHRR channel 3 and 4 ($11 \mu\text{m}$), which was derived for cloud fields over the ocean and applied to nearby cloud fields over snow and ice. This technique was applied to three test AVHRR images over Antarctica.

Chapter 3

A Model Study on Bidirectional Reflectances

Virtually all natural surfaces are now known to exhibit reflectance anisotropy. Some highly-reflecting materials, such as snow and ice, have relatively strong reflectance anisotropy. In particular, snow and ice surfaces in the Arctic show strong bidirectional reflectance due to large solar zenith angles. A satellite sensor collects reflected radiances within a small field-of-view. There is evidence that the visible and near-infrared radiances at the top of the atmosphere are sensitive to surface reflectance anisotropy and its diurnal variation (*Roujean et al.*, 1992). To retrieve surface and cloud properties from satellite radiance measurements, as we will in chapters 3 and 4, it is important to estimate the effect of surface bidirectional reflectance precisely. On the other hand, accurate values of hemispherical reflectances or albedos are needed to assess the net earth radiation budget and climate change. Computation of albedo also requires complete knowledge of the

angular reflectance characteristics of the surface.

In recent years several models have been constructed for the computation of the bidirectional reflectance (see *Barnsley et al.*, 1994 for a review). Among them Hapke's physical model (*Hapke*, 1981; *Hapke*, 1984; *Hapke*, 1986; *Hapke*, 1993) is popular and has been applied to a variety of planetary surfaces, such as vegetation canopies and soil surfaces (*Pinty et al.*, 1989; *Verstraete et al.*, 1990). The basic assumption is that the surface can be treated as a scattering and absorbing semi-infinite medium in much the same way that we treat the atmosphere (discussed later in chapter 4 and 5). Thus, the surface is described in terms of a semi-infinitely deep slab which is assigned a single scattering albedo and a phase function. The bidirectional reflectance can then be computed by solving the corresponding radiative transfer problem. Based on fundamental radiative transfer theory, Hapke developed a simple analytical approach which calculates single scattering exactly, but assumes an isotropic phase function for multiple scattering based on the two-stream approximation.

However, for surfaces with strong bidirectional reflectance like snow and ice, a model which treats multiple scattering accurately is needed. In the early 1980's, a rigorous numerical multiple scattering code DISORT (DIScrete Ordinate Radiative Transfer) was developed by Stamnes and colleagues (*Stamnes and Swanson*, 1981; *Stamnes and Dale*, 1981; *Stamnes and Conklin*, 1984). It allows for an arbitrary phase function and an accurate multi-stream approximation and thus removes the restrictions inherent in Hapke's model. Its abilities to return flux as well as radiance at arbitrary user-defined zenith and azimuth angles make it a useful tool for computing surface bidirectional reflectance.

In this chapter, we develop an accurate bidirectional reflectance model based on DISORT, which is suitable for handling snow and ice surfaces in the Arctic. We start with the pertinent radiative transfer theory in section 3.1. Hapke's bidirectional reflectance model and the opposition effect are described in section 3.2 and 3.3, respectively. In section 3.4, Hapke's model is generalized to allow for anisotropic multiple scattering. Our model is introduced in section 3.5. In section 3.6, bidirectional reflectances computed with our model are compared with those resulting from Hapke's model.

3.1 Radiative Transfer Equation

Consider a plane parallel medium (Figure 3.1a) containing irregular, randomly oriented, absorbing particles which are large compared with the wavelength. The lower boundary z_1 extends to minus infinity so that the medium becomes semi-infinite. Initially, it is assumed that the particles are so far apart that shadowing of one particle by another can be neglected. This assumption will be relaxed in section 3.3. It is also assumed that the medium in which the particles are imbedded has a refractive index equal to unity. The medium is illuminated by collimated light of flux F^s (normal to the beam) traveling in a direction which makes an angle θ_0 (incident zenith angle) with the vertical direction. The medium is observed by a detector making an angle θ (viewing zenith angle) with the vertical direction. In Figure 3.1b, ϕ is the relative azimuth angle between the incident beam and the viewing direction, Θ is the scattering angle and $\cos \Theta = \cos \theta \cos \theta_0 + \sin \theta \sin \theta_0 \cos \phi$.

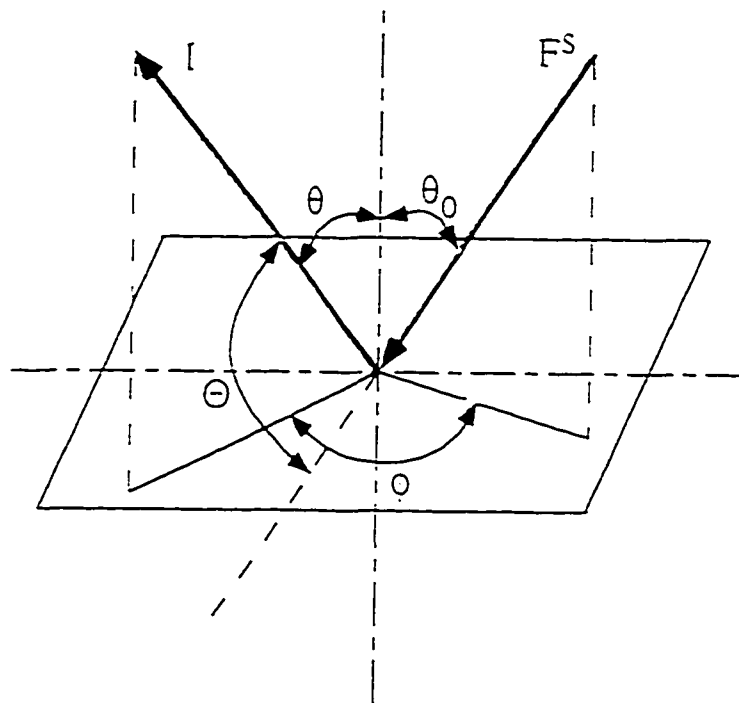
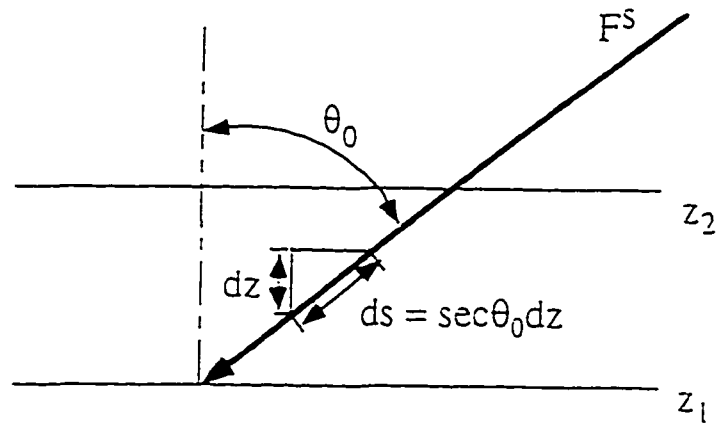


Figure 3.1 (a) Geometry of a plane-parallel medium (top); (b) Reflection geometry (bottom). F^s is incident solar irradiance, I is reflected radiance, θ_0 is solar zenith angle, θ is viewing zenith angle, ϕ is relative azimuth angle between incident solar beam and viewing direction, and Θ is scattering angle.

In Figure 3.1b $I(\tau; \theta, \phi)$ is the spectral radiance. I is defined as the radiant energy per unit wavelength interval at level τ passing in unit time through unit area perpendicular to direction of travel per unit solid angle. I can be separated into the direct incident radiance I_{dir} and diffused radiance I_{dif} . I_{dir} obeys Lambert's law, which states that the extinction along the path ds is linearly dependent on the radiance and on the amount of matter, provided that the physical state (i.e., temperature, pressure, composition) is held constant

$$dI_{dir} = -kI_{dir}ds \quad (3.1)$$

where k is the extinction coefficient. Integrating over the path $ds = \sec \theta_0 dz$ (see Figure 3.1a), for a plane-parallel slab of thickness $\delta z = z_2 - z_1$ orthogonal to the vertical direction, we have

$$I_{dir} = F^s \delta(\theta - \theta_0) \delta(\phi - \phi_0) e^{-\frac{\tau}{\mu_0}} \quad (3.2)$$

where $\mu_0 = \cos \theta_0$, $\phi_0 (= 0)$ is the azimuth of the incident beam, and τ is the vertical extinction optical depth or opacity defined as $\tau = \int_{z_1}^{z_2} k dz$. Thus τ/μ_0 , the optical distance along the path s is a measure of the extinction strength per particle and number of optically active particles along a beam.

The behavior of the diffuse or scattered intensity I_{dif} in a scattering and absorbing plane-parallel medium for the case of no sources imbedded in the medium is described by the following radiative transfer equation (*Chandrasekhar, 1960; Stamnes et al., 1988; Thomas and Stamnes, 1996*):

$$\begin{aligned} \mu \frac{dI(\tau; \mu, \phi)}{d\tau} = & I(\tau; \mu, \phi) - \frac{a}{4\pi} \int_0^{2\pi} \int_{-1}^1 I(\tau; \mu', \phi') p(\mu, \phi; \mu', \phi') d\mu' d\phi' \\ & - \frac{a}{4\pi} F^s p(\mu, \phi; -\mu_0, 0) e^{-\frac{\tau}{\mu_0}} \end{aligned} \quad (3.3)$$

where $\mu = \cos \theta$. The vertical extinction optical depth τ of a medium consisting of a mixture of absorbing/scattering molecules and particles is the sum of the individual scattering optical depth, τ_{sc} , and the absorption optical depth, τ_a .

$$\tau = \tau_{sc} + \tau_a. \quad (3.4)$$

a in equation (3.3) is the single scattering albedo, which is defined as

$$a = \frac{\tau_{sc}}{\tau} = \frac{\tau_{sc}}{\tau_{sc} + \tau_a}. \quad (3.5)$$

In equation (3.3) $p(\mu, \phi; \mu', \phi')$ is the scattering phase function, which describes the probability that a photon traveling in direction (μ', ϕ') will be scattered into direction (μ, ϕ) . The second term on the right side in equation (3.3) is due to multiple scattering, the third is a consequence of the diffuse-direct distinction and is called the solar pseudo-source. The subscript '*dif*' is omitted in equation (3.3).

The bidirectional reflectance $r(\mu_0, \mu, \phi)$ (in unit sr^{-1}) is the ratio of the total reflected radiance I in the direction of (θ, ϕ) to the incident irradiance F^s , that is

$$\rho(\mu_0, \mu, \phi) = \frac{I(\mu_0, \mu, \phi)}{F^s}. \quad (3.6)$$

A variety of techniques exists for solving equation (3.3). A review of such methods is given by *Stamnes* (1986) and *Thomas and Stamnes* (1996). An analytical solution based on the two-stream approximation used by *Hapke* (1981) and an accurate solution based on the discrete ordinate method described by *Stamnes et al.* (1988) are briefly reviewed in sections 3.2 and 3.5, respectively.

3.2 Hapke's Bidirectional Reflectance Model

Hapke (1981) derived an analytical equation for the bidirectional reflectance of

a medium composed of particles. The total radiance I is the sum of the singly-scattered radiance I_s and the multiply-scattered radiance I_m , i.e. $I = I_s + I_m$. The singly-scattered radiance is given by

$$I_s = \frac{a}{4\pi} \int_{-\infty}^0 \left[\int_0^{2\pi} \int_{-1}^1 I_{dir}(\tau; \mu', \phi') p(\Theta) d\mu' d\phi' \right] e^{-(\tau-t)/\mu} \frac{dt}{\tau} \quad (3.7)$$

and the multiply-scattered radiance is given by

$$I_m = \frac{a}{4\pi} \int_{-\infty}^0 \left[\int_0^{2\pi} \int_{-1}^1 I_{dif}(\tau; \mu', \phi') p(\Theta) d\mu' d\phi' \right] e^{-(\tau-t)/\mu} \frac{dt}{\tau}. \quad (3.8)$$

By substituting (3.2) into (3.7), we may solve directly for I_s

$$I_s = F^s \frac{a}{4\pi} \frac{\mu_0}{\mu_0 + \mu} p(\Theta). \quad (3.9)$$

The multiple-scattered radiance I_m is evaluated by solving equation (3.3) through a two-stream approximation and the assumption that the particles making up the surface medium scatter isotropically ($p(\Theta) = 1$). For a semi-infinite isotropically scattered medium the total radiance may be expressed in terms of Chandrasekhar's H-function (*Chandrasekhar, 1960*) as

$$I = F^s \frac{a}{4\pi} \frac{\mu_0}{\mu_0 + \mu} H(\mu_0) H(\mu). \quad (3.10)$$

Using equation (3.9) with $p(\Theta) = 1$ and solving for $I_m = I - I_s$ we find

$$I_m = F^s \frac{a}{4\pi} \frac{\mu_0}{\mu_0 + \mu} [H(\mu_0) H(\mu) - 1]. \quad (3.11)$$

Therefore, by adding equation (3.9) and (3.11) the bidirectional reflectance can be expressed as

$$\rho(\mu_0, \mu, \phi) = \frac{a}{4\pi} \frac{\mu_0}{\mu_0 + \mu} [p(\Theta) + H(\mu_0) H(\mu) - 1]. \quad (3.12)$$

Chandrasekhar (1960) has derived the following expression for the H-function

$$H(\mu) = \frac{1}{\mu_1 \cdots \mu_n} \frac{\prod_{i=1}^N (\mu + \mu_i)}{\prod_{j=1}^N (1 + k_j \mu)} \quad (3.13)$$

where k_j are N positive roots (or eigenvalues, see section 3.5) of the associated characteristic equation and μ_i are zeros of Legendre's polynomial $P_{2N}(\mu)$. In the two-stream approximation, we have $N = 1$, $\mu_1 = 1/2$, $k_1 = \sqrt{1-a}/\mu_1$. Therefore, the H-function may be approximated by

$$H(\mu) = \frac{1 + 2\mu}{1 + 2\mu\sqrt{1-a}}. \quad (3.14)$$

Equation (3.12) is the bidirectional reflectance derived by *Hapke* (1981) and used by many investigators (e.g. *Pinty et al.*, 1989; *Vertraete et al.*, 1990) to study reflectance from planetary surfaces.

3.3 Hapke's Treatment of the Opposition Effect

So far we have assumed that the particles in the medium are far apart. Thus, shadows caused by any scattering element can be seen in any direction. However, if the dimensions of the scattering elements are considerably larger than the wavelength of the incident radiation and the elements are sufficiently close together, the scattering elements cast a shadow on each other. If such a medium is viewed for backscattered radiation from the direction of incidence (scattering angle $\Theta = \pi$), no shadow is seen since each element hides its own shadow. As a result a pronounced increase in the brightness is observed within a small angle about the

antisolar direction. This phenomenon is referred to as the shadowing effect or the opposition effect in planetary physics and as the hot spot effect in optical remote sensing.

The opposition effect applies only to singly-scattered radiation, because multiply-scattered radiation bathes all the particles in a volume element uniformly and tends to smooth out this effect, such that bright surfaces (with large a) show less anisotropy in the backscattered direction. This conclusion is supported by a numerical calculation by *Esposito* (1979), who finds that the inclusion of an opposition effect in second-order scattering has a negligible effect.

The opposition effect has been observed for powdered soil surfaces (*Pinty et al.*, 1989), vegetation canopies (*Myneni and Kanemasu*, 1988) and snow surfaces (*Tsay and King*, 1994). According to *van de Hulst* (1957), no shadows are cast if the distance between the particles is greater than about $3r$, where r is the width of the scattering element. *Hapke* (1963) was the first to model the hot spot phenomenon for the planetary surfaces. *Hapke's* formulation takes into account most of the observed surface reflectance characteristics and can be applied to a wide variety of surfaces. It characterizes the hot spot as a function of single scattering albedo, phase function and surface compactness. The model leads to a modification (*Hapke*, 1986) to equation (3.12)

$$\rho(\mu_0, \mu, \phi) = \frac{a}{4\pi} \frac{\mu_0}{\mu_0 + \mu} [(1 + B(\Theta))p(\Theta) + H(\mu_0)H(\mu) - 1] \quad (3.15)$$

where $p(\Theta)B(\Theta)$ gives the phase function for the hot spot

$$B(\Theta) = \frac{B(0)}{1 + \frac{1}{h} \tan\left(\frac{\pi - \Theta}{2}\right)}. \quad (3.16)$$

In equation (3.16), $B(\Theta)$ is called the shadowing function. $B(0)$ is a measure of the amplitude of the hot spot peak, which is the ratio of the near-surface contribution $S(0)$ to total scattering at $\Theta=180^\circ$; that is, $B(0) = S(0)/(ap(180^\circ))$. The amplitude is large for dark surfaces since $B(0)$ is inversely proportional to a . If the surface is completely opaque, all of the light comes from the surface; in that case, $S(0)$ reaches its maximum, $S(0) = ap(180)$ then $B(0)=1$. For a plowed field, the typical value of $S(0)$ is around 0.37 in the visible band (*Pinty et al.*, 1989). h is a measure of the angular width of the hot spot peak, and it relates to the gap in the scattering elements or interparticle spacing in the surface layer. A lower value of h implies a more loosely spaced medium, and a higher value of h corresponds to a comparatively compact surface. For a plowed field, the typical value of h is around 0.25 in visible band (*Pinty et al.*, 1989).

3.4 Generalization of Hapke's Model to Allow for Anisotropic Multiple Scattering

In general, reflected radiance at the top of the medium $I(\mu_0, \mu, \phi)$ may be expressed as

$$I(\tau = 0; \mu_0, \mu, \phi) = F^s \frac{a}{4\pi} \frac{\mu_0}{\mu_0 + \mu} R(\mu_0, \mu, \phi) \quad (3.17)$$

where $R(\mu_0, \mu, \phi)$ is the reflection function. Considering the opposition effect and relaxing the assumption of isotropic multiple scattering and use of two-stream approximation adopted in Hapke's formulation in equation (3.15), the bidirectional

reflectance may be generally expressed as

$$\begin{aligned}
 \rho(\mu_0, \mu, \phi) &= \frac{a}{4\pi} \frac{\mu_0}{\mu_0 + \mu} [(1 + B(\Theta))p(\Theta) + R(\mu_0, \mu, \phi) - p(\Theta)] \\
 &= \frac{a}{4\pi} \frac{\mu_0}{\mu_0 + \mu} [B(\Theta)p(\Theta) + R(\mu_0, \mu, \phi)] \\
 &= \frac{a}{4\pi} \frac{\mu_0}{\mu_0 + \mu} B(\Theta)p(\Theta) + I(\tau = 0; \mu_0, \mu, \phi)/F^s
 \end{aligned} \tag{3.18}$$

where $I(\tau = 0; \mu_0, \mu, \phi)$ is the radiance, including multiply-scattered and singly-scattered radiance without the correction of opposition effect, and $B(\Theta)$ is expressed as in equation (3.16).

In this chapter, the Henyey-Greenstein phase function is used for its simplicity and its reasonable approximation to an actual Mie scattering phase function

$$p(\Theta) = \frac{1 - g^2}{(1 + g^2 - 2g \cos \Theta)^{3/2}} \tag{3.19}$$

where g is asymmetry factor, ranging from -1 to 1. For $g = 0$, $p(\Theta) = 1$, which corresponds to an isotropic scattering. For $g = 1$, the Henyey-Greenstein phase function yields complete forward scattering, and for $g = -1$ it yields complete backward scattering.

3.5 Computation of the Bidirectional Reflectance Based on the Discrete-Ordinate Radiative Transfer Code

The discrete ordinate method of solving the radiative transfer equation (3.3) was developed by Chandrasekhar in the 1940's. The approach is to reduce the integro-

differential equation by means of Gaussian quadrature to a set of ordinary differential equations. However, difficulties in finding eigensolutions (*Liou, 1973; Asano, 1975*), and in finding the constants of integration for multi-layered media (*Samuelson, 1969*), were encountered. In the early 1980s, an unconditionally stable solution was developed by Stamnes and colleagues (*Stamnes and Swanson, 1981; Stamnes and Dale, 1981; Stamnes and Conklin, 1984*). Subsequently this approach was implemented into a robust computational code (*Stamnes et al., 1988*) which is referred to as DISORT (DIScrete Ordinate Radiative Transfer).

The radiance $I(\tau; \mu, \phi)$ in equation (3.3) can be expanded in a Fourier cosine series as

$$I(\tau; \mu, \phi) = \sum_{m=0}^{2N-1} I^m(\tau, \mu) \cos(m\phi) \quad (3.20)$$

where N is the number of streams. The general discrete ordinate solution for I^m at any angle is given by *Stamnes and Dale, 1981* and *Thomas and Stamnes, 1996*

$$I^m(\tau, +\mu) = \sum_{j=-N}^N G_j^m(\mu) \{e^{-k_j^m \tau} - e^{k_j^m \tau_N + (\tau_N - \tau)/\mu}\} \quad (3.21)$$

and

$$I^m(\tau, -\mu) = \sum_{j=-N}^N G_j^m(-\mu) \{e^{-k_j^m \tau} - e^{-\tau/\mu}\} \quad (3.22)$$

where $G_j^m(\mu) = L_j^m g_j^m(\mu)$ for $j \neq 0$, τ_N is the total optical depth of the medium. The k_j^m and the $g_j^m(\mu)$ are the eigenvalues and eigenvectors, and the L_j^m are constants of integration to be determined from the boundary conditions. For $j = 0$, $G_0^m(\mu) \equiv Z_0^m(\mu)$ and $k_0^m \equiv 1/\mu_0$, where $Z_0^m(\mu)e^{-\frac{\tau}{\mu_0}}$ is the particular solution. The solution of I from equation (3.20)-(3.22) therefore may be applied to equation (3.18) to obtain the bidirectional reflectance.

3.6 Comparisons of Bidirectional Reflectance Derived from Hapke's and Our Models

Figure 3.2 shows a plot of the simulated bidirectional reflectances as a function of viewing zenith angle θ in the principal plane, in which the relative azimuth angle $\phi = 0^\circ$ (as $\theta < 0$) or 180° (as $\theta > 0$). In this Figure the results from our model are represented by solid lines while those from Hapke's model are represented by dotted lines. The upper-left, upper-right, lower-left, and lower-right panels are for asymmetry factor $g = 0, 0.3, 0.6,$ and $0.9,$ respectively. Results for three different incident zenith angles are plotted in each of the panels. In the calculation, we set single scattering albedo $a = 0.5,$ opposition effect parameters $S(0) = 2.0,$ and $h = 0.6.$

A Lambertian surface yields constant reflectances for various viewing angles. As shown in Figure 3.2, the reflectance is far from uniform. Even for an isotropic scattering phase function ($g = 0$), the reflectance is not constant. The larger the value of $g,$ the more drastic is the reflectance variation. A local maximum in reflectance occurs exactly when the viewing angle equals the incident angle, which is the hot spot peak discussed in the previous section. As the viewing angle approaches $\pm 90^\circ,$ the reflectance increases to very high values.

For isotropic scattering phase functions ($g = 0$), our result is about the same as that from Hapke's model as shown in the upper-left panel. For an anisotropic scattering phase function $g \neq 0,$ the reflectance resulting from our model is different from that produced by Hapke's model. The larger the value of $g,$ the greater is

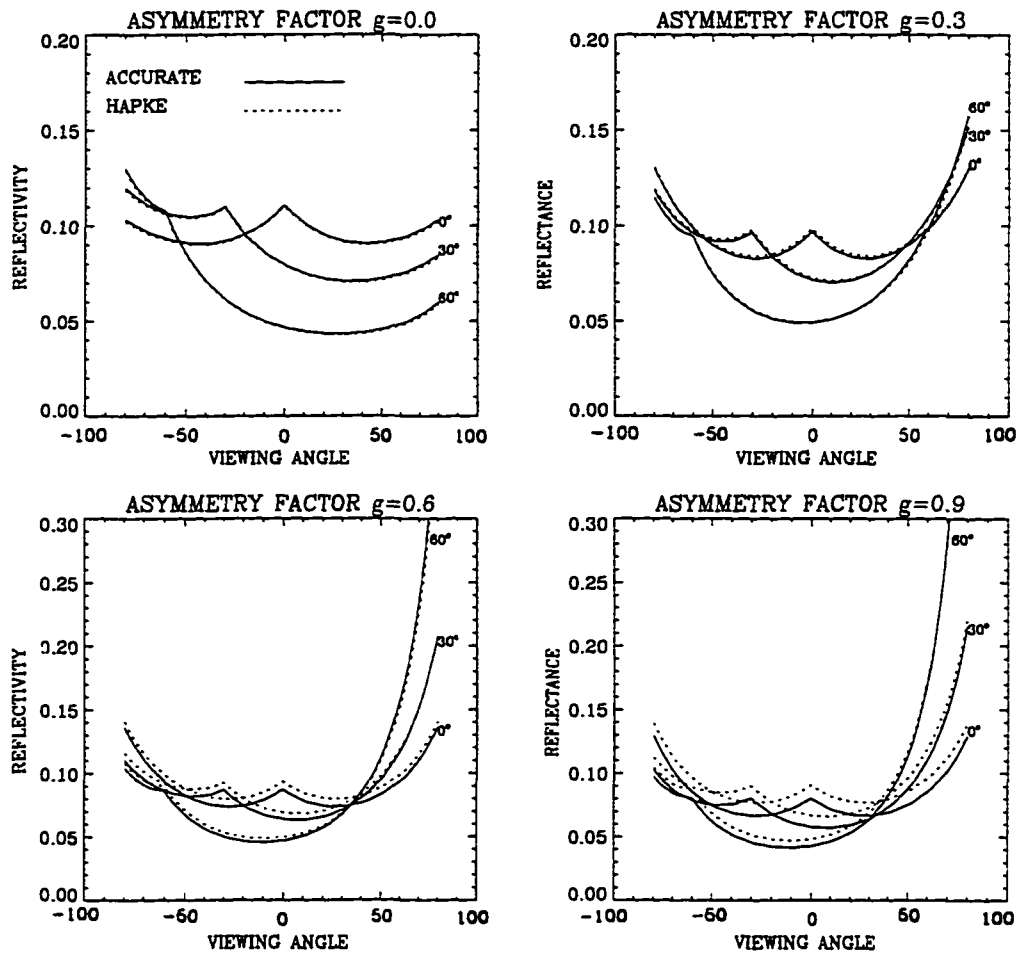


Figure 3.2 Computed bidirectional reflectances as a function of viewing angle θ in the principal plane for three different incident zenith angles and four different asymmetry factors. The solid lines are results computed by our model, and the dotted lines are those by Hapke's model. The single scattering albedo a is assumed to be 0.5, opposition effect parameters $S(0)$ to be 2.0, and h to be 0.6.

the difference, as expected. When $g = 0.9$ as shown in the lower-right panel, the difference is over 0.01 sr^{-1} in the reflectance for some viewing angles.

In the plane perpendicular to the principal plane, the reflectance as a function of viewing angle is shown in Figure 3.3. The bidirectional reflectances are symmetric about the $\theta = 0$ line. When the incident angle is zero, the results is exactly the same as in the principal plane shown in Figure 3.2. When $g = 0$, the results from our model (dotted lines) are very close to those from Hapke's model. Otherwise, they are different. The larger the value of g , the larger is the difference.

For viewing angles away from the principal plane, there is no local maximum at $\theta = \theta_0$ (the hot spot peak) in the perpendicular plane. The variation of the reflectance is less drastic than that in the principal plane.

In order to illustrate the effects of single scattering albedo a on the difference between our model, a more complete physical model, and Hapke's model, we show in Figure 3.4 the reflectance as a function of viewing angle for various values of a in the principal plane. Our model and Hapke's model are represented by solid and dotted lines, respectively, for comparison. In the calculation, we set the asymmetry factor to $g = 0.6$, the incident zenith angle to $\theta_0 = 40^\circ$, and we ignore the opposition effect ($S(0) = 0$). It is obvious from the figure that the larger the value of a , the larger is the difference between the two models. Theoretically, this is quite understandable since the larger the value of a , the stronger is the multiple scattering effect, and the difference between our model and Hapke's model is due entirely to the treatment of multiple scattering.

In the plane perpendicular to the principal plane, the reflectance as a function of viewing angle is shown in Figure 3.5 for various values of a . In the perpendicular

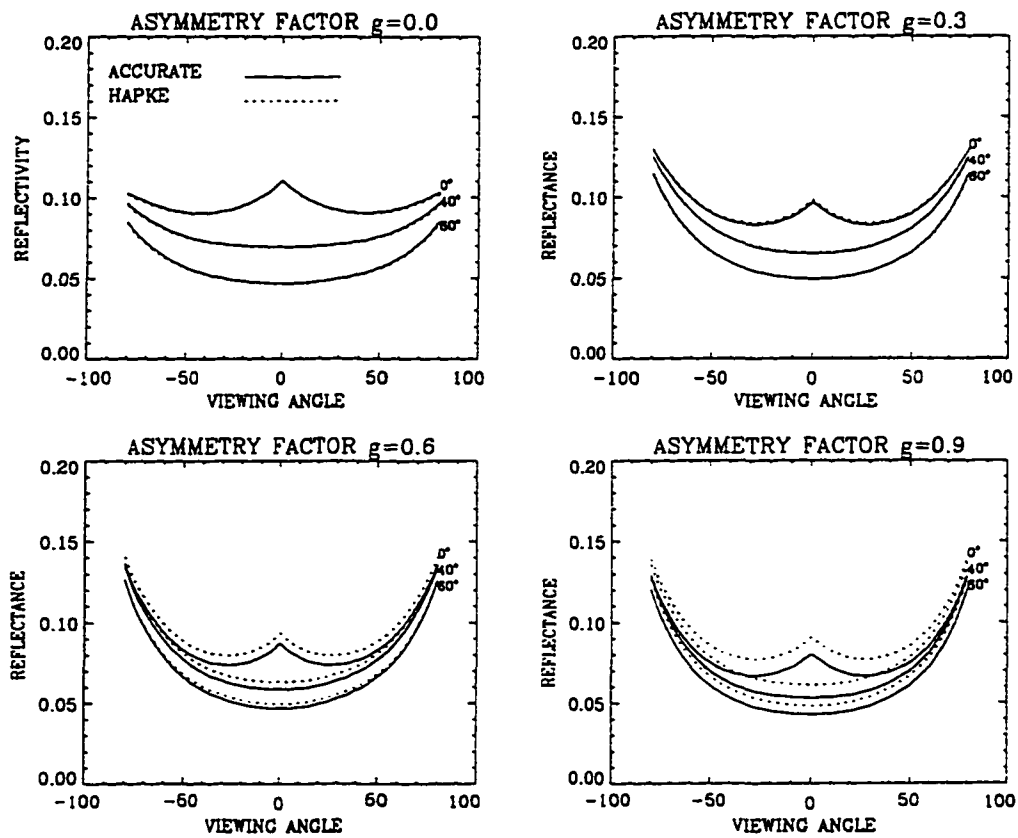


Figure 3.3 Same format as Figure 3.2 but in the plane perpendicular to the principal plane.

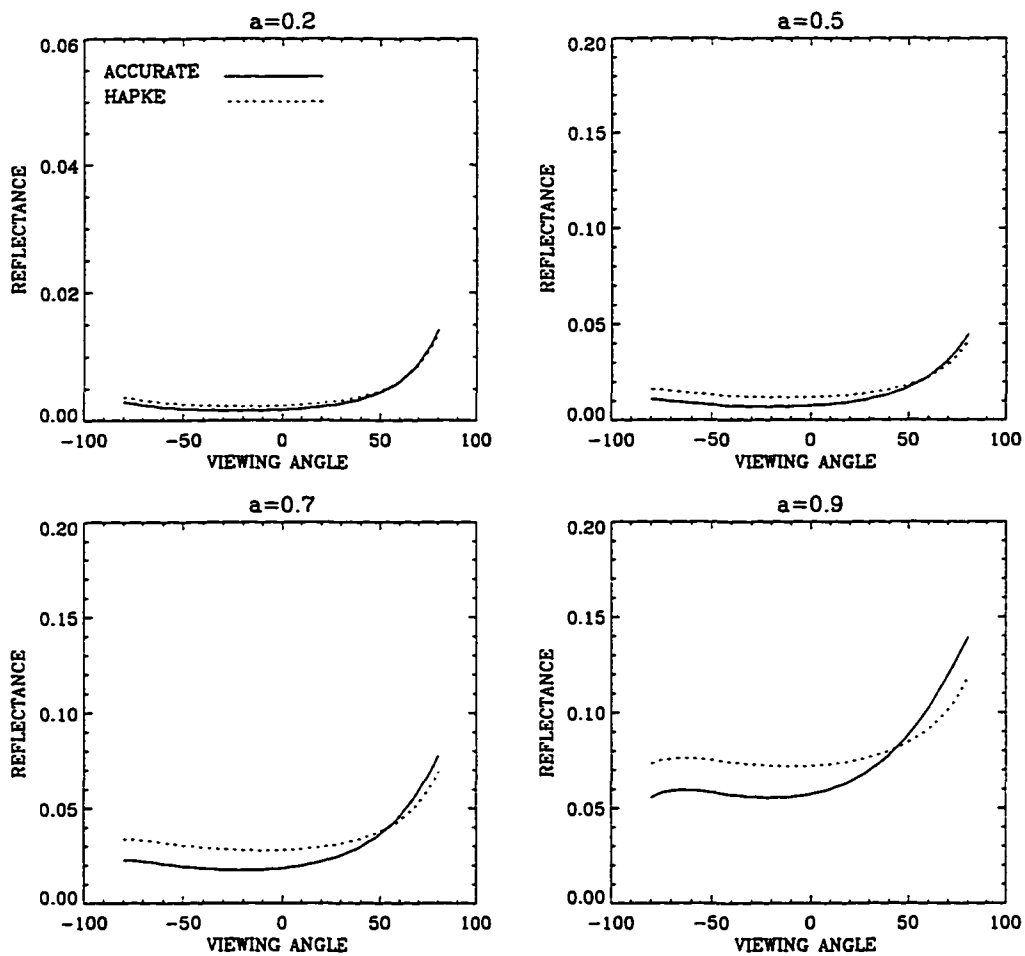


Figure 3.4 Same format as Figure 3.2 but for different single scattering albedo a . The asymmetry factor g is fixed as 0.6. The solar zenith angle θ_0 is assumed to be 40° . The opposition effect is not included.

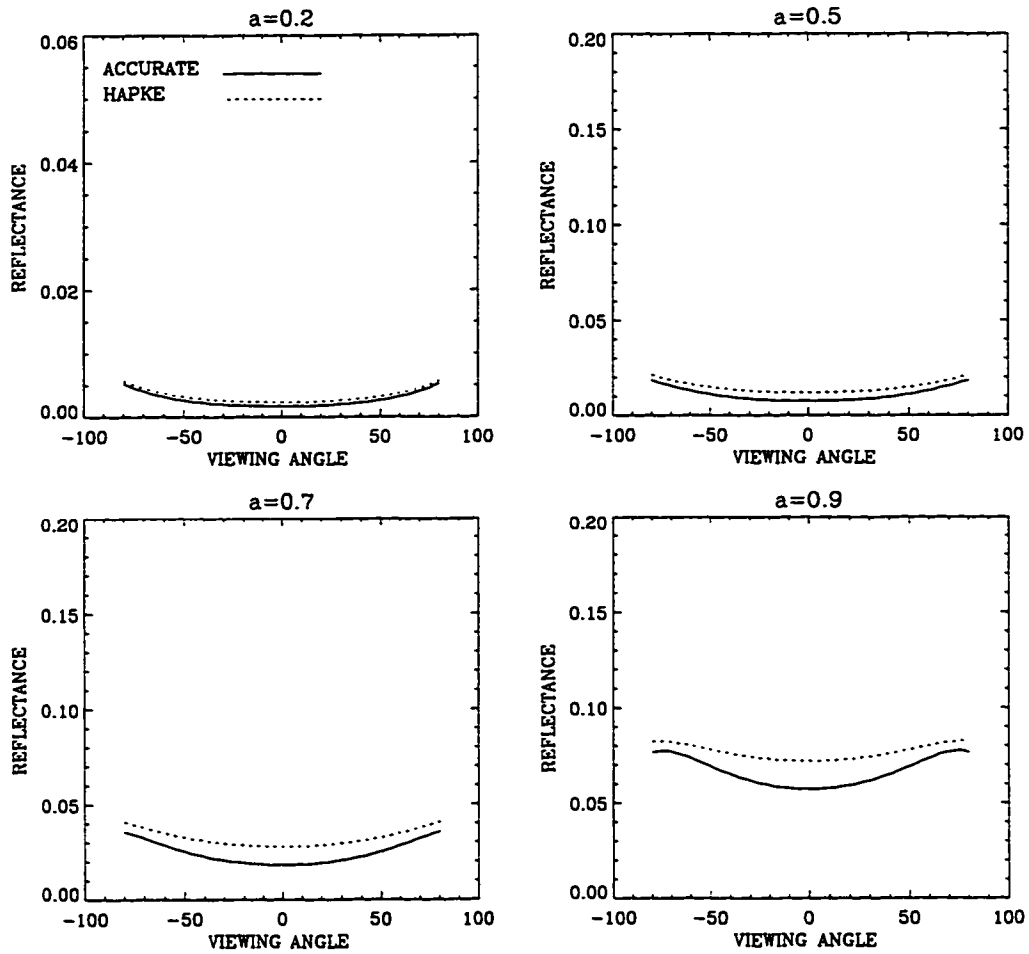


Figure 3.5 Same as Figure 3.4 but in the plane perpendicular to the principal plane. The opposition effect is not included.

plane, similar to the result in principal plane, the larger the value of a , the larger the difference between the two models. However, the difference is not as strong as in the principal plane.

The percentage deviation of reflectance in the principal plane between our model and Hapke's model is shown in Figure 3.6 for several values of the asymmetry factor g and the single scattering albedo a . In the computation, we set $\theta_0 = 60^\circ$, $S(0) = 2$, and $h = 0.6$. When a is small as in the upper-left panel where $a = 0.2$, there is not much difference between our model and Hapke's, regardless of what the value of g is. As a becomes larger, the deviation between the two models increases and the effect of increasing anisotropy (larger g) becomes significant. Thus, the larger the value of g , the larger the difference between the two models. When $a = 0.98$ and $g = 0.9$ as shown in the lower-left panel, the reflectance from our model can be more than 30% different from Hapke's model.

3.7 Summary

An extension of Hapke's bidirectional reflectance model for planetary surfaces to account more rigorously for multiple scattering effects is discussed. A numerical model based on a rigorous multiple scattering code DISORT is used to compute the bidirectional reflectances of planetary surfaces. In the model, the opposition effect is taken into account in the same way as in Hapke's bidirectional reflectance model which has been widely used in studies of vegetation canopies and soil surfaces. A comparison of bidirectional reflectance produced by the two models may be summarized as follows:

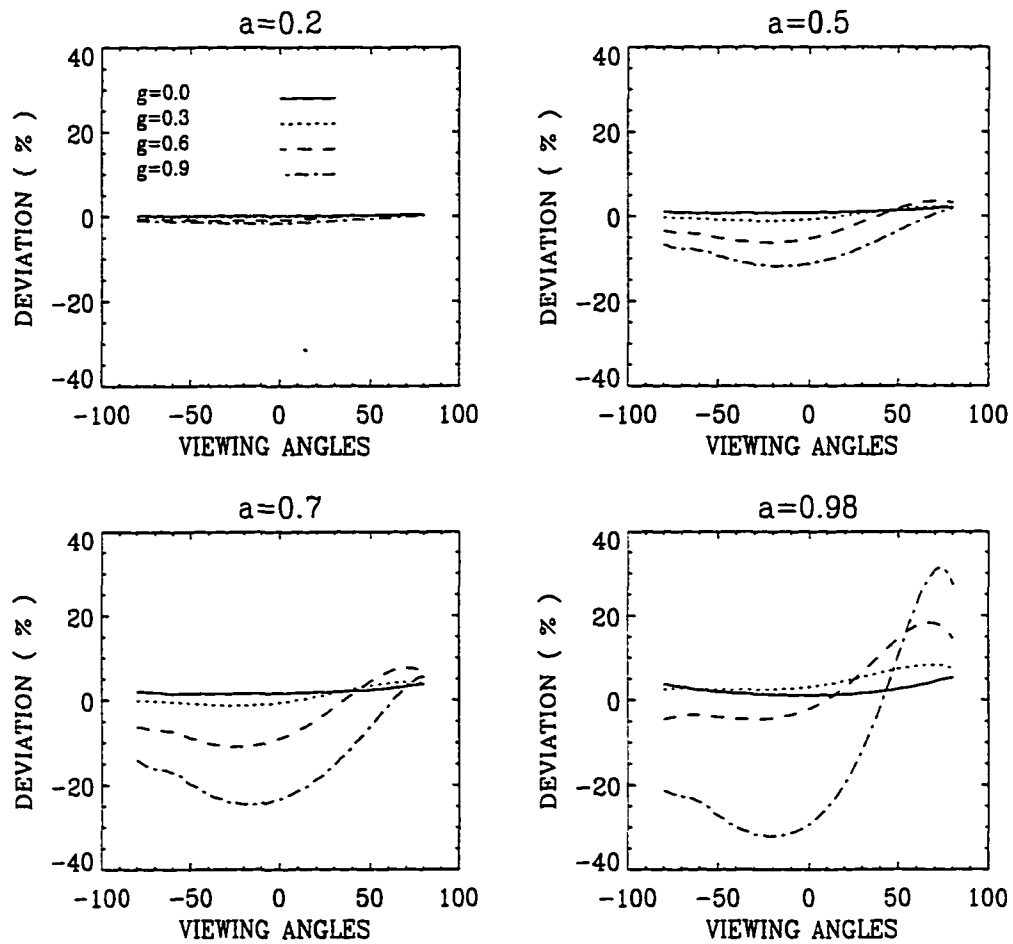


Figure 3.6 Deviations on bidirectional reflectance between our model and Hapke's model as a function of viewing angle in the principal plane for various asymmetry factors and single scattering albedos. Solar zenith angle θ_0 is assumed to be 60° , opposition effect parameters $S(0)$ to be 2.0, and h to be 0.6.

(1) The larger the single scattering albedo a , the larger the difference between the two models.

(2) The larger the asymmetry factor g , the larger the difference between the two models.

(3) The deviation between the two models is significant. When both a and g are large, which is the case for snow surfaces, the deviation can be larger than 40%.

The reason for these differences can be ascribed to different treatments of multiple scattering in the two models. In Hapke's model, the single scattering is calculated exactly, while an isotropic multiple scattering phase function is assumed to obtain an analytical expression for bidirectional reflectances in the two-stream approximation. In our formulation, the phase function and the number of streams can be arbitrary and do not have the restrictions that apply to Hapke's model. For illustration purposes, we adopted a Henyey-Greenstein phase function, and used the accurate DISORT algorithm to solve the radiative transfer problem which allows us to assess the implications of the physical (isotropic scattering) and numerical (two-stream only) shortcomings of Hapke's model.

For pure snow surfaces, both a and g are close to unity in the visible and near-infrared wavelengths (*Wiscombe and Warren, 1980*). In this parameter range, the comparison between our model and Hapke's model shows a very significant difference. The complete knowledge of the bidirectional reflectance for snow surfaces is required to retrieve surface and cloud properties in the arctic from satellite-measured radiances (see in chapters 4 and 5). We will employ the model developed in this chapter to compute bidirectional reflectance for snow surfaces in order to

allow for a more realistic treatment of the underlying surface.

Chapter 4

Retrieval of Surface Albedo in the Arctic from AVHRR Clear-sky Measurements

In chapter 3 we developed an accurate bidirectional reflectance model which is suitable for snow/ice surfaces in the Arctic. Bidirectional reflectance is a very important feature for the interpretation of satellite data because satellite sensors with narrow fields of view measure reflected radiances within only a narrow angle. The anisotropy of the reflected radiation is particularly significant for low solar elevations, which at high latitudes occur most of the time throughout the year. Previous investigators have developed techniques for retrieving surface albedo and solar irradiances from satellite-measured radiances (e.g. *Saunders, 1990; Stuhlmann and Bauer, 1991; Pinker and Laszlo, 1992; De Abreu et al., 1994*). Most methods rely on the use of an “anisotropic correction” to the TOA albedo to account for the bidi-

rectional reflectance, while the underlying surface is assumed to be a Lambertian (isotropic) reflector. The anisotropic correction is usually done by multiplying the TOA albedo obtained by assuming that the TOA reflected radiation is isotropic, with an empirical anisotropic correction factor, which is based on results from the Earth Radiation Budget Experiment (ERBE) studies of anisotropic reflectance over various surfaces (*e.g.* Taylor and Stowe, 1984; Suttles *et al.*, 1988). However, ERBE is a broadband instrument so it is assumed that the correction factor is the same in AVHRR channels 1 and 2 (*De Abreu et al.*, 1994).

In this chapter, we attempt to develop an algorithm that is specifically tailored to Arctic conditions. The bidirectional reflectance of snow surfaces is included in a comprehensive radiative transfer model instead of assuming a Lambertian reflector. This algorithm is different from the traditional methods based on empirical anisotropic corrections. Instead, it relies on a comprehensive radiative transfer model in which radiative transfer simulations are carried out by the DISORT code applicable to a plane-parallel atmosphere. This approach obviates the need for “anisotropic corrections”. The surface properties are adjusted in the model until the computed TOA radiance matches the satellite observation. In this study, we retrieve broadband albedo and upward, downward, and net solar irradiances at the surface from AVHRR-measured narrowband radiances in channel 1 and 2.

This chapter is organized as follows. In section 4.1, the related satellite data and field measurements, including their calibration and accuracy, are described. In section 4.2, we briefly describe the comprehensive radiative transfer model adopted in this study. Under cloud-free conditions, the retrieval procedures are introduced for tundra and snow surfaces in section 4.3. The retrieval results are presented in

section 4.4. The retrieval results are discussed in section 4.5. A summary is given finally in section 4.6.

4.1 Satellite and Field Data in the Arctic

AVHRR data are used to retrieve surface albedo and the surface radiation budget, and the results are compared with 1992 CMDL field measurements from Barrow, Alaska.

The satellite data used in this chapter are from channel 1 (0.58-0.68 μm) and channel 2 (0.72-1.1 μm) of the AVHRR instrument launched on NOAA polar orbiting satellites. Both NOAA-10 and NOAA-11 were in operation in 1992. More details on the AVHRR instrumentation are given in *Kidwell (1995)*.

There is evidence that pre-launch calibration coefficients of the AVHRR visible (channel 1) and near-infrared (channel 2) channels for which there are no on-board calibration capabilities, have changed in orbit. Investigations of *Rao and Chen (1995)* indicated that the relative annual degradation rates for the two channels are 1.2 % and 2.0 % (NOAA-11), respectively. In this study we adopt Rao and Chen's post-launch calibration equations, which have been recommended to users by the NOAA/NASA AVHRR Pathfinder Calibration Working Group, as follows:

$$R_1 = 0.5496(C_{10}(1) - 40)\exp(0.33 * 10^{-4} * d) \quad (4.1)$$

and

$$R_2 = 0.3680(C_{10}(2) - 40)\exp(0.55 * 10^{-4} * d) \quad (4.2)$$

where R_1 and R_2 are calibrated radiances for each channel in $Wm^{-2}sr^{-1}\mu m^{-1}$, d

is the day after launch, $C_{10}(1)$ and $C_{10}(2)$ are measured signals in 10-bit counts for channel 1 and 2, respectively. For NOAA-10, we adopt post-launch calibration coefficients proposed by *Teillet et al.* (1990) in the following formulae

$$R_1 = \frac{C_{10}(1)}{1.61} - \frac{35.3}{1.61} \quad (4.3)$$

and

$$R_2 = \frac{C_{10}(2)}{2.10} - \frac{33.8}{2.10}. \quad (4.4)$$

Surface solar radiation measurements in Barrow, Alaska ($71^{\circ}18'$ N, $156^{\circ}47'$ W) provided by the CMDL are utilized in this study. Broadband solar radiation measurements by Eppley pyranometers, covering the wavelength range 0.3 - 2.8 μm , include upward and downward global solar irradiances. The uncertainty in the measurements is less than 2.0% for solar zenith angle $\theta_0 < 60^{\circ}$ (see section 2.3). The hourly-averaged measurements from March to August 1992 are used in this study for comparison with the satellite-derived irradiances. The underlying surface changes from snow to melting snow to tundra. Clear pixels in the Barrow area are identified based on the climatological records by National Weather Services (NWS) for Barrow with cloud cover of 0. A total of 19 sets of co-located TOA AVHRR and CMDL surface measurements at Barrow, Alaska in 1992 is selected in this study. They are listed in Table 4.1.

4.2 Radiative Transfer Model

We use a comprehensive radiative transfer model that considers radiative interactions with atmospheric gases, such as CO_2 , O_3 , O_2 , and water vapor, and scat-

Table 4.1 Observing conditions of AVHRR measurements.

No	Day	Date	θ_0^1	θ^2	ϕ^3	Surface Type
1*	107	April 16	67.5	5.1	186.4	Snow
2*	117	April 26	69.5	24.7	159.8	Snow
3*	118	April 27	68.2	32.3	6.5	Snow
4	159	June 7	75.7	21.5	50.6	Melting Snow
5	160	June 8	52.7	38.3	33.3	Melting Snow
6	181	June 29	49.4	2.4	35.4	Tundra
7*	181	June 29	66.2	20.3	22.3	Tundra
8	187	July 5	50.9	18.8	35.7	Tundra
9	189	July 7	50.2	4.5	37.0	Tundra
10*	189	July 7	67.6	25.9	21.5	Tundra
11*	190	July 8	62.2	38.8	43.1	Tundra
12*	191	July 9	56.6	5.4	178.1	Tundra
13*	191	July 9	63.9	2.7	176.5	Tundra
14	197	July 15	51.4	6.8	36.7	Tundra
15*	209	July 27	61.9	12.6	1.8	Tundra
16	209	July 27	52.7	18.1	139.5	Tundra
17	209	July 27	56.3	37.1	34.8	Tundra
18	242	August 29	62.9	17.2	141.3	Tundra
19	242	August 29	66.7	38.3	34.9	Tundra

* NOAA-10 data, the rest is from NOAA-11.

1 solar zenith angle

2 satellite zenith angle

3 relative azimuth angle

tering and absorption/emission by stratospheric aerosols, haze particles, and tropospheric aerosols. Radiative transfer simulations are carried out by a discrete-ordinates method (DISORT) applicable to a plane-parallel vertically inhomogeneous atmosphere-Earth system (*Stamnes et al.*, 1988), which has previously been used for rigorous theoretical studies of both the troposphere and stratosphere (*e.g.* *Tsay et al.*, 1989; *Stamnes and Tsay*, 1990; *Wang and Lenoble*, 1994; *Zeng et al.*, 1994; *Forster and Shine*, 1995). For computational efficiency the exponential-sum fitting of transmissions (ESFT) method (*Tsay et al.*, 1989) is adopted to simulate the gaseous absorption in a multiple scattering atmosphere. Molecular scattering is computed from Rayleigh scattering theory (*Penndorf*, 1957). In this study, the sub-arctic summer and winter atmospheric profiles (*McClatchey et al.*, 1971) are employed. The atmosphere is divided into 33 layers vertically. For snow-free conditions (tundra) an albedo is assigned to the surface, while an additional layer is added at the bottom of the atmosphere to represent snow overlying tundra. The solar spectrum from 0.28 to 4 μm is divided into 24 bands with unequal spectral widths which vary from 240 to 3040 cm^{-1} . By this model, irradiance and radiance at any layer can be computed, for any combination of individual bands as well as for the entire solar spectral range. For irradiance computations integrated across the solar spectrum, it has been shown that the accuracy of this broadband model is a few Wm^{-2} compared with a narrowband model for which the spectral width is less than 100 cm^{-1} (*Tsay et al.*, 1990).

4.2.1 Arctic Haze

Arctic haze is an important feature in the Arctic. It has been reported since the 1950s and can reduce downward shortwave fluxes at the surface by 10-12 Wm^{-2} and upward fluxes at the TOA by 6 Wm^{-2} in summertime under cloud-free conditions with low relative humidity (*Tsay et al.*, 1989). Its concentration varies seasonally with a maximum in late spring and a minimum in late summer (*Shaw*, 1982). It appears vertically distributed in multiple layers within 3 km above the surface (*Valero et al.*, 1983). Observations indicate that Arctic haze contains a substantial amount of anthropogenic compounds like sulphuric acid and soot. *Blanchet and List* (1983) built a sophisticated physical model to calculate the optical properties of Arctic haze by Mie theory. Based upon available observations, this model assumes a 3-mode (2 accumulation modes and 1 coarse mode) lognormal size distribution. For computational efficiency, the optical properties of Arctic haze were parameterized as a function of relative humidity through a least squares fitting based on *Blanchet and List's* haze model (*Tsay et al.*, 1989).

Figure 4.1 shows the wavelength dependence of the extinction coefficient, single scattering albedo and asymmetry factor for Arctic haze (solid line) calculated by *Tsay's* parameterizations for dry conditions (70% relative humidity). In the present study the optical depth is limited to lie between 0.06 and 0.16 at 0.50 μm , for summer and spring, respectively, to agree with available measurements (*Shaw*, 1982).

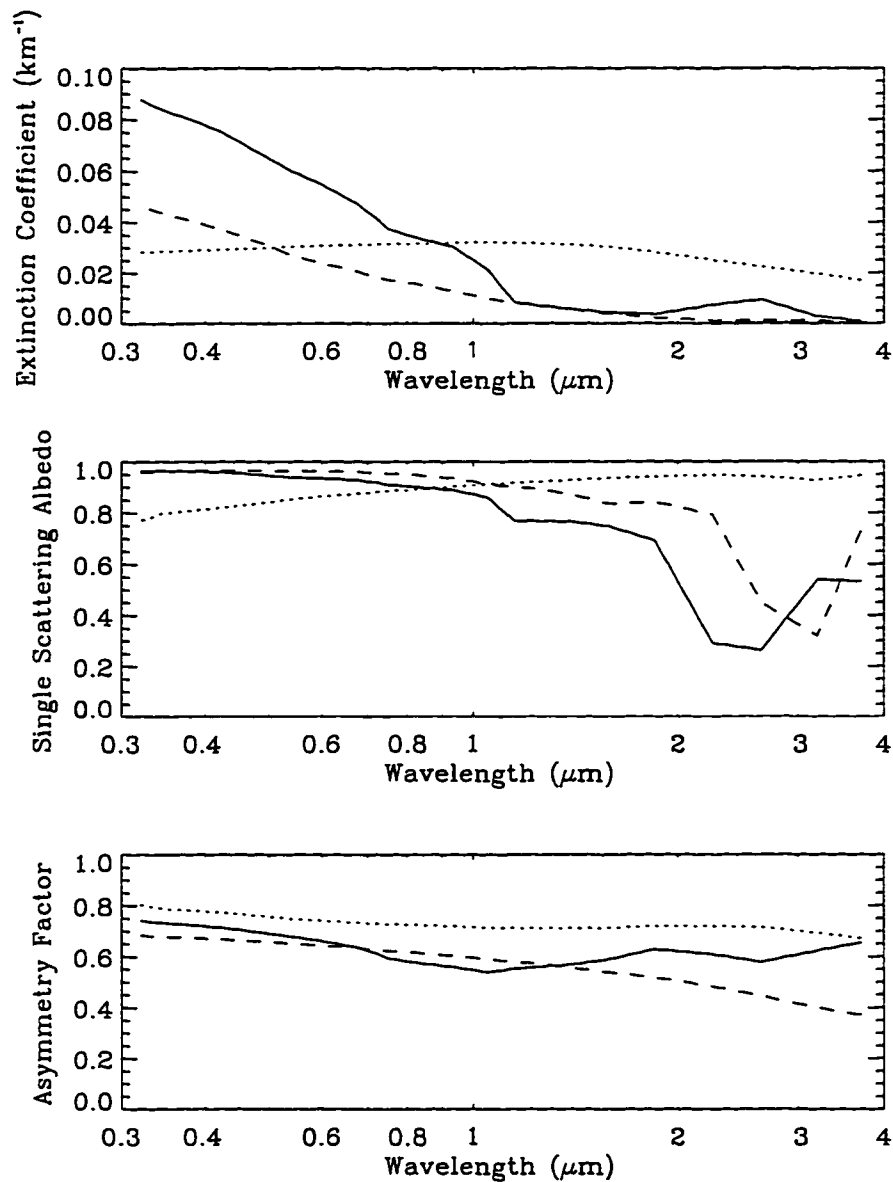


Figure 4.1 The wavelength dependence of the extinction coefficient, single scattering albedo and asymmetry factor in the solar spectral region for Arctic haze at 70% relative humidity (solid line) from *Tsay et al.'s* (1989) parameterizations, fresh volcanic ash (dotted line) and tropospheric aerosol at 70% relative humidity (dashed line) from the *Shettle and Fenn* (1976) models. Note that the extinction coefficient shown is the value at 2 km for Arctic haze, at 19 km for volcanic ash and at 4 km for tropospheric aerosol, where the extinction coefficient reaches the maximum.

4.2.2 Stratospheric Aerosols

Following the eruptions of Mt. Pinatubo (June 14, 1991), decreases of 25 to 30% in direct solar irradiance were recorded by the CMDL pyrhelimeters, and the derived monthly average aerosol optical depth anomalies at Barrow reached nearly 0.3 during summer of 1992 (*Dutton and Christy, 1992*). Being mainly of volcanic origin, the stratospheric aerosol layer is usually situated between 10 and 30 km and is composed primarily of sulfuric acid solution droplets, which are produced through photochemical reactions (*Turco et al., 1982*). *Shettle and Fenn (1976)* summarized four different vertical profiles of the extinction coefficients for background, moderate, high, and extreme volcanic aerosol loading situations which represent various stages in the evolution of the stratospheric aerosol layer after a volcanic eruption. The size distributions are represented by a modified gamma distribution specified by a “Fresh Volcanic Model” and a “Aged Volcanic Model”, which represent the situation within one year or more after a volcanic eruption. Also shown in Figure 4.1 is the wavelength dependence of the extinction coefficient, single scattering albedo and asymmetry factor for fresh volcanic (dotted line) conditions from the *Blanchet and List (1983)* models. We have chosen the profile corresponding to doubled high volcanic aerosol loading and the “fresh” volcanic model, to represent the stratospheric aerosols over Barrow, Alaska after the eruption of Mt. Pinatubo. These choices lead to an optical depth of the stratospheric aerosols over Barrow, Alaska of 0.19 at 0.55 μm , in agreement with CMDL measurements during 1992.

4.2.3 Tropospheric Aerosols

In the troposphere between 3 km and 10 km, a tropospheric aerosol model proposed by *Shettle and Fenn* (1976) is adopted. These aerosols are assumed to have the composition of 70% water-soluble and 30% dust-like. They are partly produced from reactions between various gases in the troposphere, and partly due to dust particles picked up from the surface. Larger aerosol particles are dropped during the long residence of aerosols above the ground. This leaves the log-normal size distribution with the small particle component. The wavelength dependence of the extinction coefficient, single scattering albedo and asymmetry factor for tropospheric aerosol in summer/spring conditions with 23 km visibility and 70% relative humidity is displayed in Figure 4.1 (dashed line). The corresponding optical depth of the tropospheric aerosol is 0.07 at $0.55 \mu\text{m}$.

The aerosol extinction coefficient profile at $0.55 \mu\text{m}$ used in this study is shown in Figure 4.2. The total optical depth of the aerosol is 0.42 for spring and 0.32 for summer. These values are higher than normal due to the eruption of Mt. Pinatubo. The evidence of the effect of the eruption of Mt. Pinatubo on arctic aerosols is also found in Resolute Passage in the Canadian Archipelago, where the optical depth of aerosol derived through a Sun photometer and model calculations for May 13, 1992 is 0.303 (*De Abreu et al.*, 1994).

For lack of better knowledge the Henyey-Greenstein phase function is adopted in this paper to represent Arctic haze, volcanic aerosol and tropospheric aerosols.

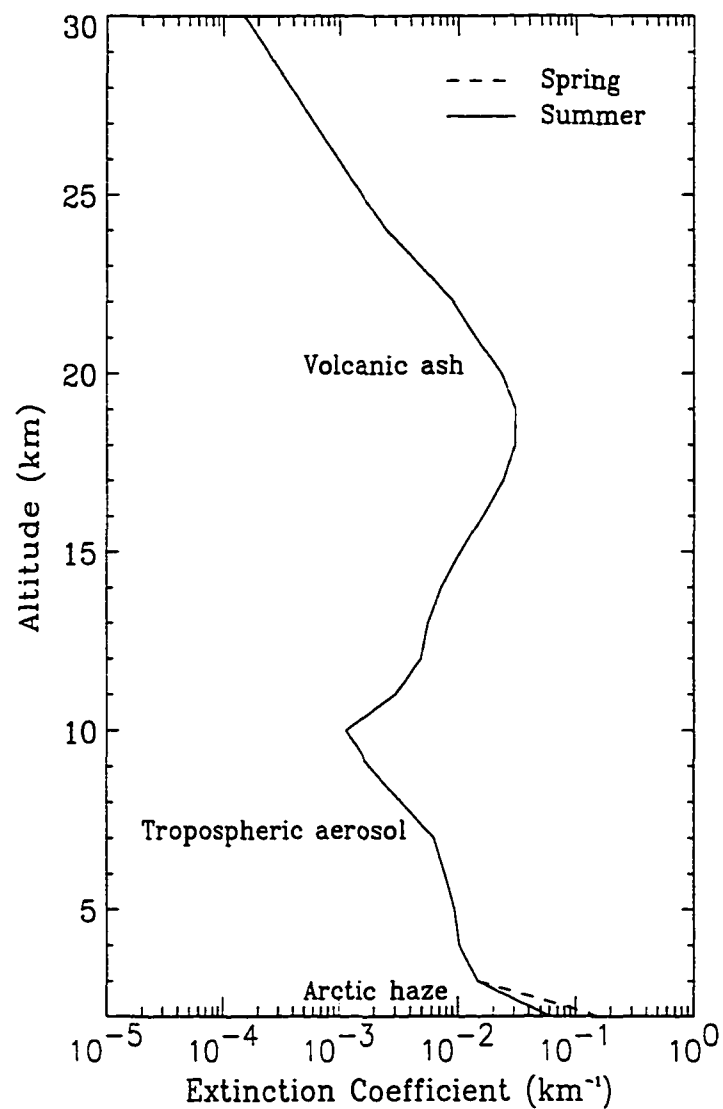


Figure 4.2 The particulate extinction coefficient profile at $0.5 \mu\text{m}$ from the *Shettle and Fenn* (1976) models and *Tsay et al.*'s (1989) parameterizations. The solid line represents summer conditions and the dashed line spring conditions.

4.2.4 Boundary Conditions

Field measurements and model simulations indicate that snow exhibits significant bidirectional reflectance properties, which are more pronounced at larger solar zenith angles (e.g., *Warren et al.*, 1986; *Han et al.*, 1993, *Li*, 1982). Because snow is a highly anisotropic reflector, the Lambertian approximation could lead to substantial errors. Therefore, we employ the optical properties of pure snow obtained by *Wiscombe and Warren* (1980), *Warren and Wiscombe* (1980) through Mie computations, and treat snow as one additional vertical layer when we carry out the radiative transfer calculations. The most important variable controlling snow albedo is the mean grain size. The average grain radii are in the range 20-100 μm for new snow, 100-300 μm for fine-grained older snow, and 1000-1500 μm for old snow near the melting point. In the visible region, *Warren and Wiscombe* (1980) introduced trace amounts of absorptive impurities such as graphitic carbon for soot contaminated snow. In the infrared region the albedo of pure snow remains the same as that for soot contaminated snow due to the high imaginary refractive index for ice throughout the infrared. For a mixture of snow/ice and soot, the optical properties are obtained by properly weighting each component. The mass-fraction of soot ranges from 0.01 to 0.06 ppmw (parts per million by weight) for Arctic snow/ice based on observations (*Warren*, 1982). The albedo of tundra is low, around 20% in solar spectral band (*Grenfell and Perovich*, 1984). Lacking knowledge of the bidirectional reflectance for tundra, we thus adopt the Lambertian approximation.

To characterize the anisotropy it is customary to use a bidirectional anisotropy

factor defined as follows:

$$R_\lambda(\theta_0, \theta, \phi) = \frac{\pi I_\lambda(\theta_0, \theta, \phi)}{F_\lambda} \quad (4.5)$$

where $I_\lambda(\theta_0, \theta, \phi)$ is the radiance backscattered in a direction specified by the viewing zenith angle θ and the relative azimuth angle ϕ between the viewing direction and solar beam. θ_0 is the solar zenith angle, and F_λ is the upward irradiance at the TOA. By definition the bidirectional anisotropy factor represents the extent to which the backscattered radiation field departs from isotropy. Its value should be unity when the radiation field is isotropic.

Figure 4.3 shows the patterns of the bidirectional anisotropy factor in AVHRR channel 1 computed by the radiative transfer model described above for (i) a bare snow surface (no atmosphere), and (ii) at the TOA over a snow surface under clear-sky conditions (no clouds and/or aerosols) and (iii) at the TOA over a snow surface under cloud-free conditions in the presence of haze. The solar zenith angle was taken to be 70° . For a bare snow surface (Figure 4.3a) the values of the contours range from 0.22 to 5.50, far from unity, indicating that the radiation reflected by the snow surface is highly anisotropic in the visible band, which is consistent with observations. In Figure 4.3b the range is smaller than that at the bare snow surface, showing that the TOA radiation field in a clear-sky situation in the absence of haze is less anisotropic than that for the bare snow surface case (no atmosphere). But the minimum and the maximum values range from 0.70 to 3.11, still far from unity. So the TOA radiation field under clear sky conditions in the absence of haze is highly anisotropic. Figure 4.3c shows that the addition of haze slightly reduces the degree of anisotropy in the TOA radiation field over a

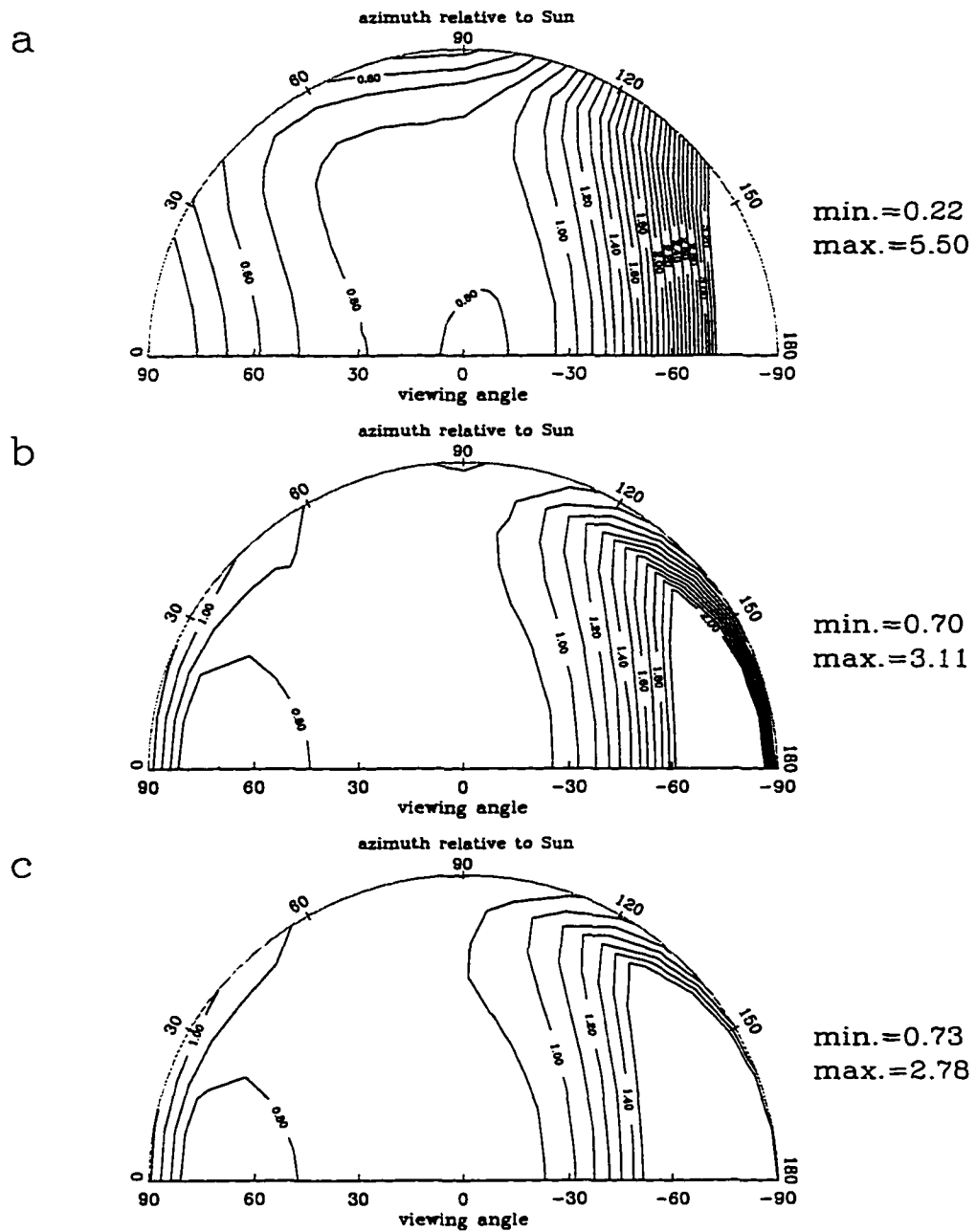


Figure 4.3 Contour plots of simulated bidirectional anisotropy factor in AVHRR Channel 1 (for $\theta_0 = 70^\circ$) at (a) snow surface without atmosphere, (b) the TOA over snow surface for clear-sky conditions in the absence of haze, and (c) the TOA over snow surface for clear-sky conditions in the presence of haze with optical depth 0.16. Snow grain size is $200 \mu\text{m}$.

snow surface so that the anisotropy factor ranges from 0.73 to 2.78. Thus, in the presence of haze the radiation field remains highly anisotropic.

4.3 Retrieval Procedures

The rationale behind our retrieval procedure is to start by determining the surface properties through the comparison of computed and measured (AVHRR) narrow-band TOA radiance as the first step. Then the next step is to compute the solar radiation budget at the surface using the retrieved surface properties obtained in step 1. Two different procedures are designed depending on the underlying surface type. Figure 4.4 provides a flow chart of the retrieval algorithm for tundra, and Figure 4.7 shows the corresponding flow chart for snow.

Raw counts of NOAA-11 AVHRR measurements are converted into radiances at the TOA by *Rao and Chen's* calibration procedures (Equations (4.1) and (4.2)) for channel 1 and channel 2. Otherwise, the post-launch calibration procedures (Equations (4.3) and (4.4), *Teillet et al.* (1990)) are applied to NOAA-10 data to convert counts into radiances. The geometry information including the solar zenith angle θ_0 , the satellite zenith angle θ and the relative azimuth angle ϕ between the Sun and the satellite that are imbedded in the HRPT data can be obtained by one of the TeraScan algorithms.

In the case of tundra, the surface albedo for each channel is given an initial value based on field measurements made by *Grenfell and Perovich* (1984) at Barrow, Alaska. Then the TOA radiance is computed by the radiative transfer model described in section 4.2 with the sun-satellite geometry information as in-

put parameters. This process is repeated by adjusting the surface albedo until the computed radiance matches the observed TOA radiance of channel 1 and channel 2 from AVHRR, respectively. We then compute the albedo in the solar region using the following narrowband-to-broadband conversion equation proposed by *Key* (1996)

$$\alpha = 0.00341505 + 0.342583\alpha_1 + 0.571224\alpha_2 \quad (4.6)$$

where α is the broadband surface albedo for clear sky over snow-free land, α_1 and α_2 are narrowband surface albedo for each channel. Once the broadband surface albedo is estimated, the downward and upward irradiances at the surface over the solar spectral region can be computed from the radiative transfer model. The procedures are illustrated in Figure 4.4.

Figure 4.5 & 4.6 illustrate the reflected radiance in channel 1 and 2 as a function of the mass-fraction of soot and snow grain size, respectively. Figure 4.6 shows that the TOA radiance in channel 2 is generally not sensitive to the amount of soot embedded in the snow when the mass-fraction of soot is less than 1 ppmw. According to *Warren* (1982), the mass-fraction of soot was estimated ranging from 0.01 to 0.06 ppmw for arctic snow/ice based on observations. Therefore, in the case of snow, the first step is to adjust the snow grain size until the computed TOA radiance in channel 2 agrees with the measured one. In the second step after the grain size is determined, the mass-fraction of soot in the snow is estimated by the same procedure using the radiance of Channel 1. Using the derived snow grain size and the mass-fraction of soot as input, the upward and downward solar irradiances at the air-snow interface can be computed from the radiative transfer

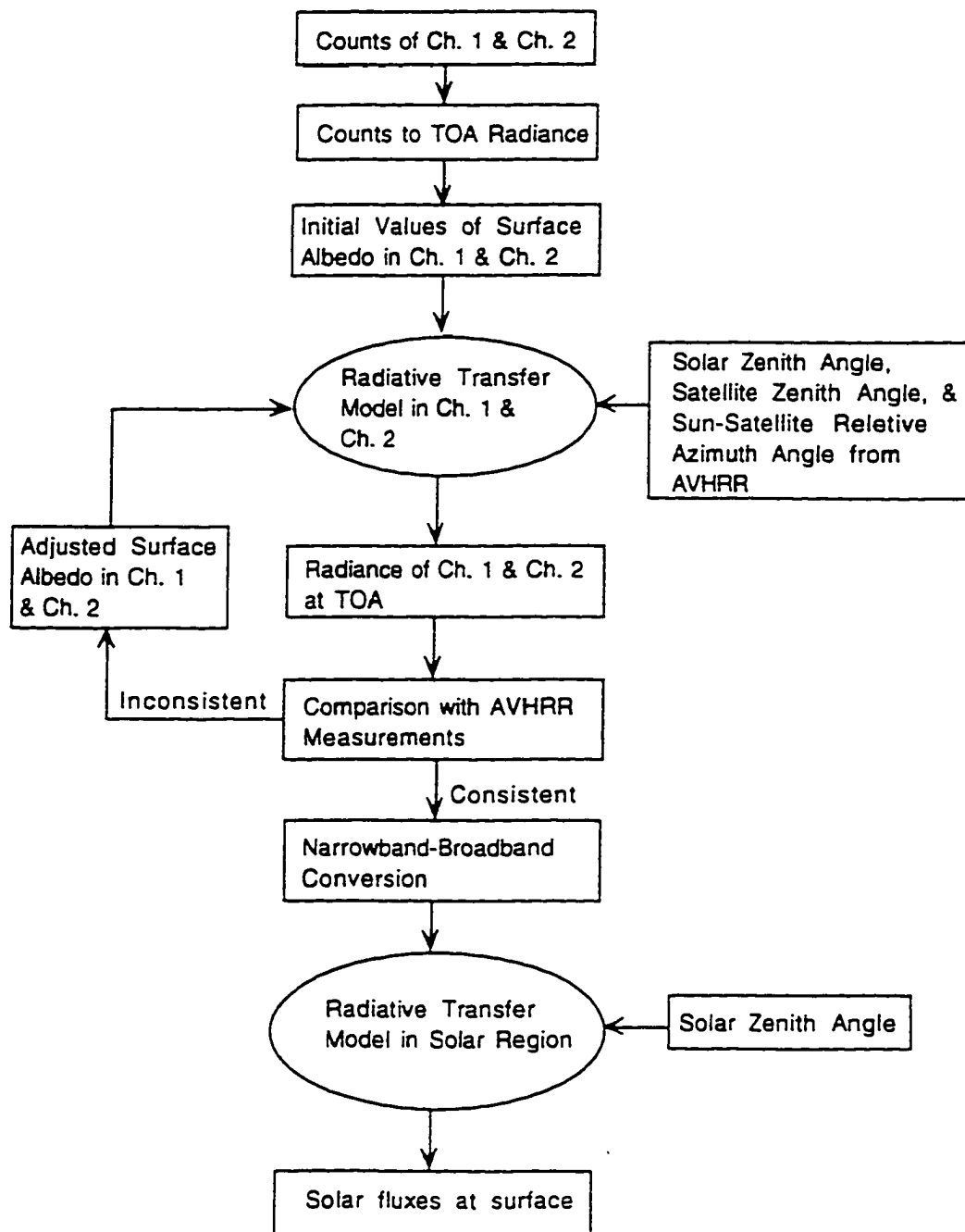


Figure 4.4 Flow chart of retrieval algorithm for tundra surface.

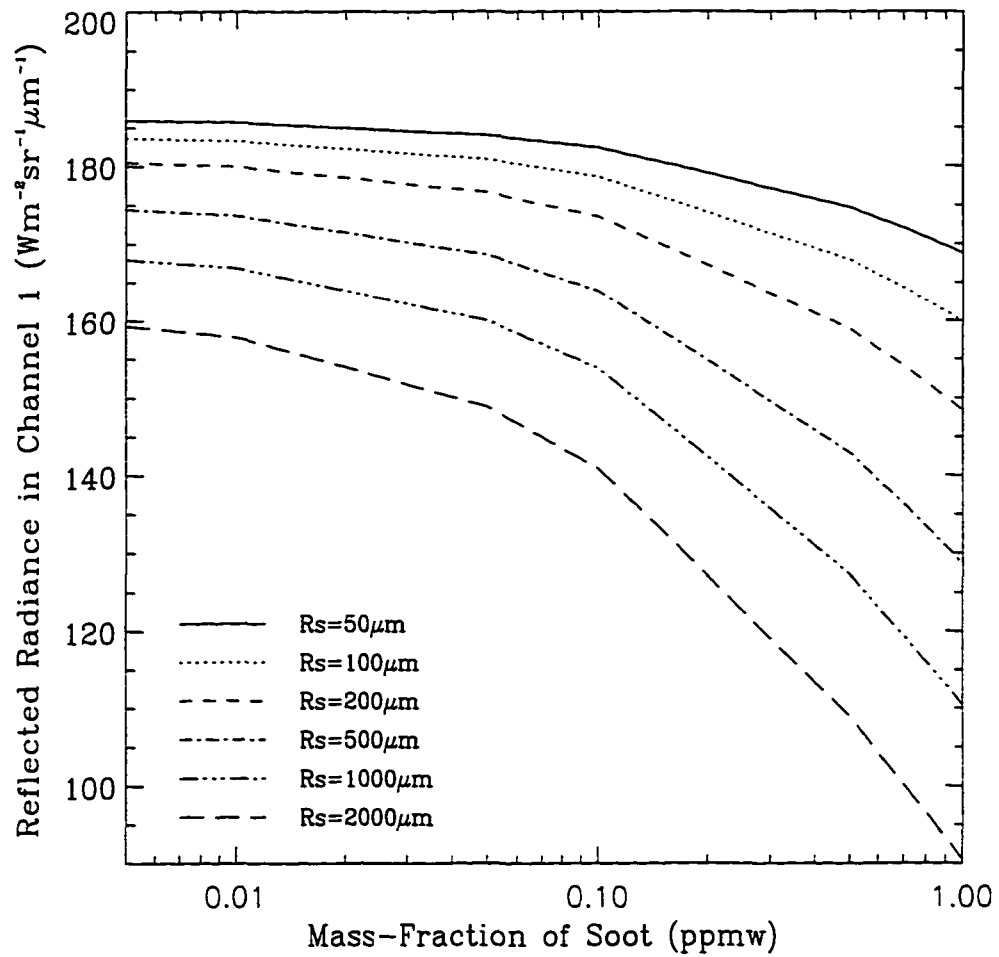


Figure 4.5 Simulation of reflected solar radiances in AVHRR channel 1 as a function of the mass-fraction of soot and snow grain size with the condition of solar zenith angle $\theta_0=60^\circ$, satellite zenith angle $\theta=10^\circ$, relative azimuth angle between the Sun and the satellite $\phi=50^\circ$ and 5.74 cross-section area per unit mass for soot.

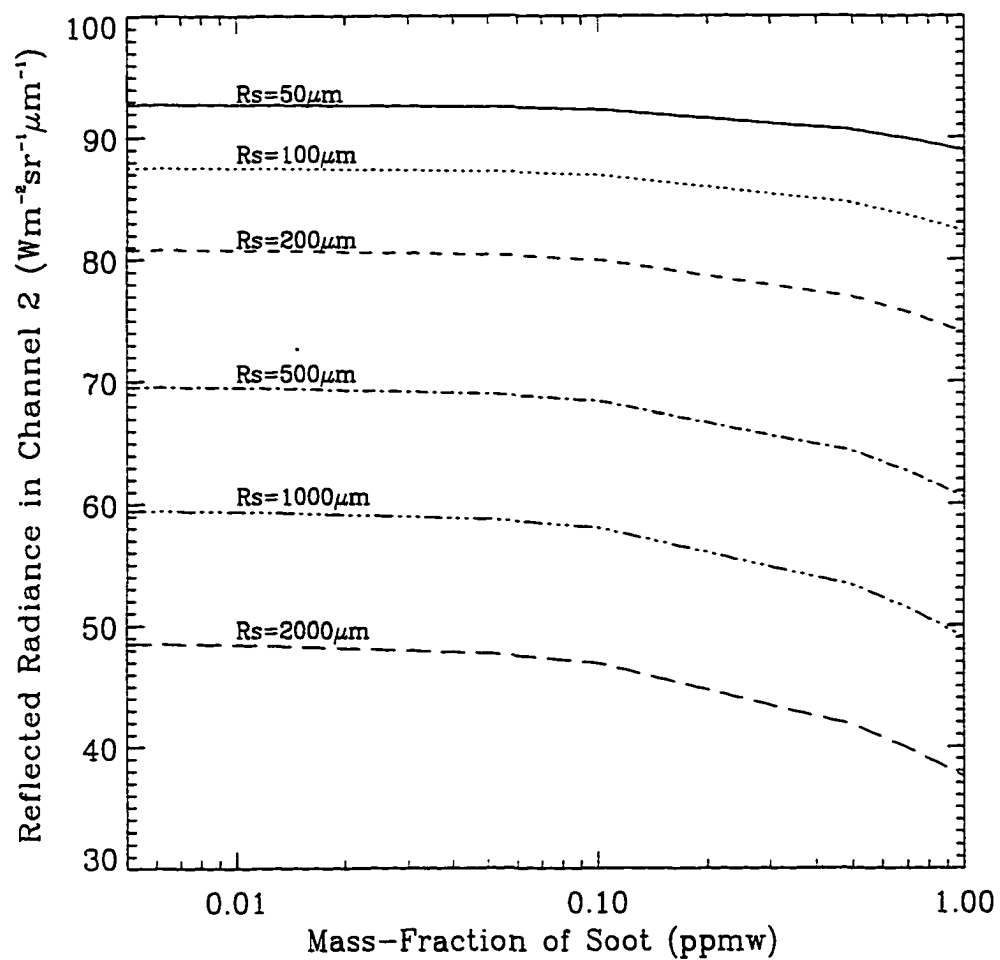


Figure 4.6 Simulation of reflected solar radiances in AVHRR channel 2 as a function of the mass-fraction of soot and snow grain size with the condition of solar zenith angle $\theta_0 = 60^\circ$, satellite zenith angle $\theta = 10^\circ$, relative azimuth angle between the Sun and the satellite $\phi = 50^\circ$ and 5.74 cross-section area per unit mass for soot.

model. The ratio of upward to downward solar irradiance yields the broadband albedo of snow. The procedures are shown in Figure 4.7.

Note that the mass-fraction of soot is usually higher than 0.1 ppmw during the snow melting season, and that the independence of the radiance in channel 2 on the mass-fraction of soot is not valid (see Figure 4.6). To retrieve snow grain size and mass-fraction of soot, the above procedures for channel 1 and channel 2 should be repeated until the calculated radiances in channel 1 & 2 agree with the satellite measurements. This can also be applied to snow surfaces in mid-latitudes where the amount of soot embedded in snow is usually higher than that in the polar regions.

In this study we also test the validity of the Lambertian assumption over snow (see section 4.4.2). Treating snow as a Lambertian surface, we use the same retrieval procedure as for tundra to determine the narrowband albedo of channel 1 and channel 2 of snow. The broadband albedo is determined by the conversion

$$\alpha = 0.04228 + 0.661\alpha_1 + 0.208\alpha_2 \quad (4.7)$$

given in *Key* (1996) based on measurements made by others on the Greenland ice sheet.

4.4 Retrieval Results

4.4.1 Comparison of Satellite-inferred and Ground-based Results

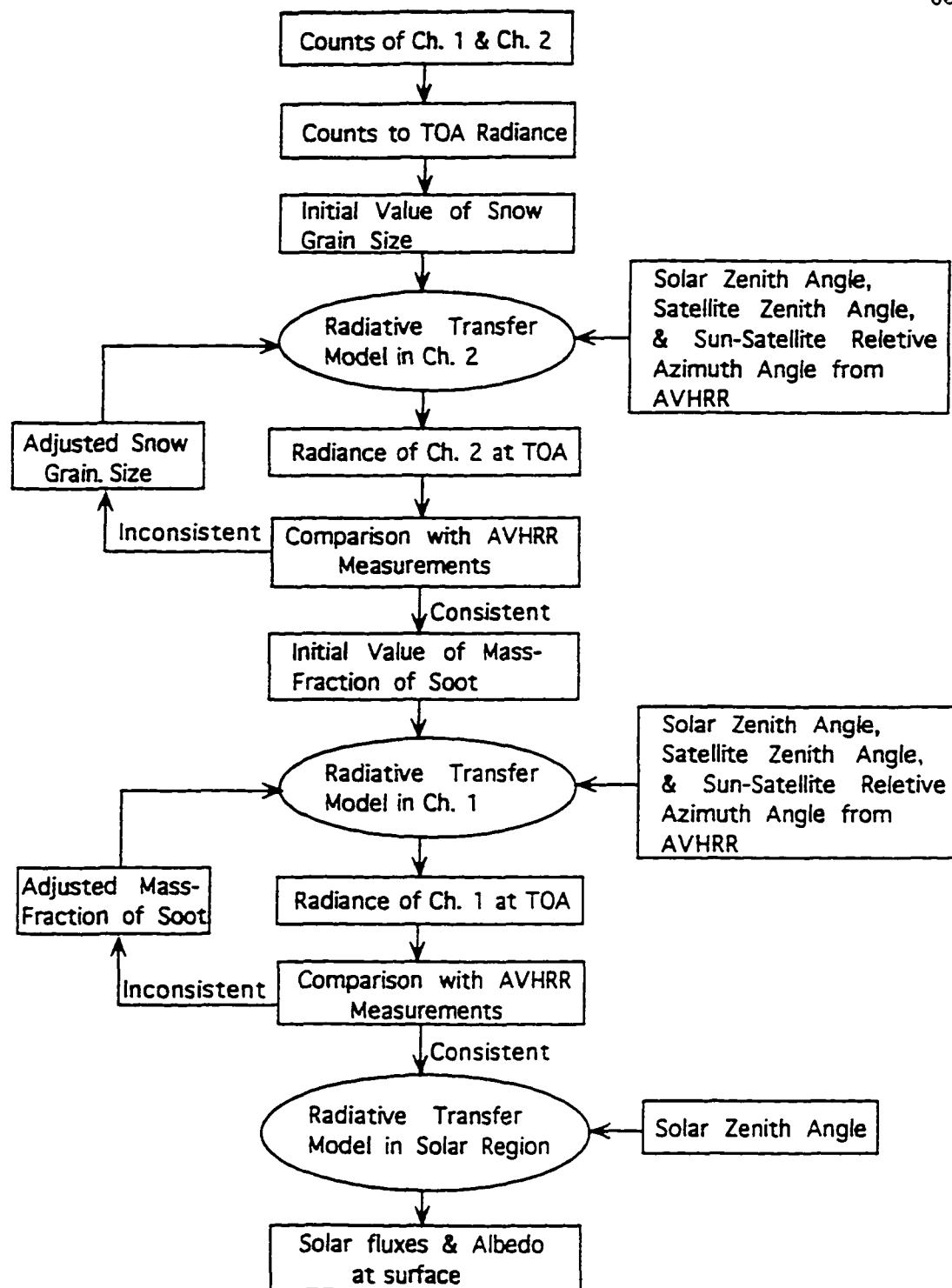


Figure 4.7 Flow chart of retrieval algorithm for snow surface.

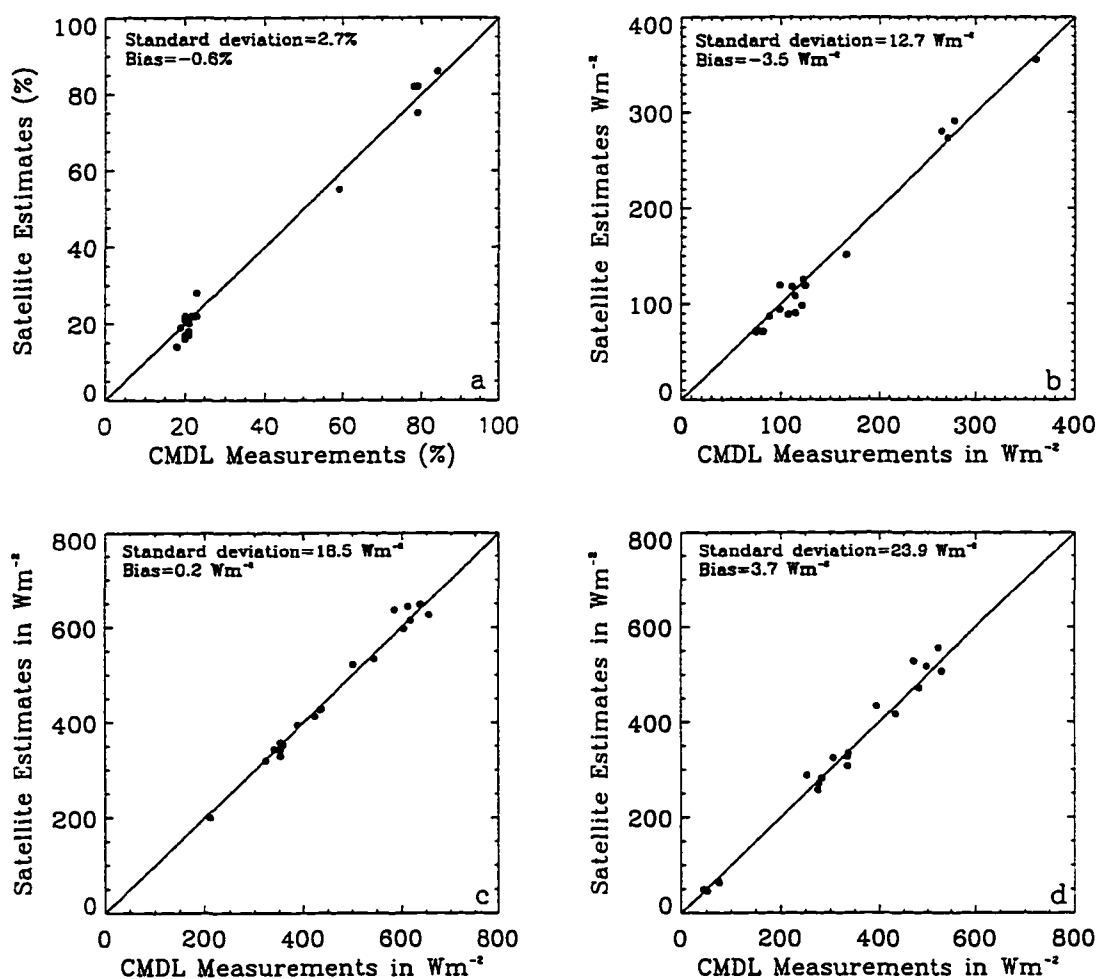


Figure 4.8 Scatter plots of satellite estimates versus ground-based CMDL measurements for (a) albedo, (b) upward irradiance, (c) downward irradiance, and (d) net irradiance at Earth surface for all 19 cloud-free cases (tundra and snow).

Figure 4.8 compares the retrieval results (vertical axes) with field measurements (horizontal axes) for a total of 19 cloud-free cases.

Figure 4.8a compares satellite derived surface albedos to those obtained by CMDL at the surface. In this figure, a group of 11 data points has an albedo close to 20%. Another group of 4 has a much higher value of albedo around 60-80%. Obviously the group with low surface albedo comes from summer when the underlying surface is tundra, whereas the high albedo group comes from winter when the underlying surface is covered by snow. The data point with an intermediate value of albedo (around 60%) comes from a time when snow is in the process of melting.

As we can see from Figure 4.8a, the bias is very small (0.6%) while there is some scatter between the retrieval results and the surface measurements, the standard deviation being 2.7%. The scatter is partly due to the Lambertian approximation for tundra surfaces, and the narrowband-to-broadband conversion (equation (4.6)) for tundra surfaces. Equation (4.6) is derived for vegetation, not specifically for tundra. Lacking information on tundra we use equation (4.6) in this study. In addition, part of the scatter is due to the different field of view between satellite sensors and pyranometers.

A small bias also appears in Figure 4.8b, c and d in which the upward, downward, and net (downward minus upward) irradiances, respectively, are plotted. Over the 19 cases, the bias is -3.5 Wm^{-2} for upward irradiance, 0.2 Wm^{-2} for downward irradiance and 3.7 Wm^{-2} for net irradiance.

Some scatter is also shown in Figure 4.8b and d, the standard deviation being 12.7 Wm^{-2} for upward irradiance and 23.9 Wm^{-2} for net irradiance. As discussed

by *Li et al.* (1993), the scatter is partly due to temporal mismatch between satellites and field measurements. The latter is hourly averaged, thus the averaged value of the solar zenith angle within the hour may be different from the value of the solar zenith angle when the satellite measurement was taken. Also, part of the scatter is introduced by the error of retrieved surface albedo. The temporal mismatches between satellite and field measurements cause random errors, which could be substantially reduced by averaging over a large number of measurements. Figure 4.8c shows a small standard deviation of 18.5 Wm^{-2} for downward irradiance. Since downward irradiance is dominated by the solar zenith angle and the state of atmosphere, and is relatively insensitive to surface albedo, the standard deviation for the downward irradiance primarily reflects the temporal mismatch between satellite and surface measurements.

4.4.2 Effect of Bidirectional Reflectance of Snow

Figure 4.9 has the same format as Figure 4.8 but focuses on only the 5 out of the 19 cases for which the underlying surface is snow-covered. The solid points represent results for a snow surface with bidirectional reflectance properties, while the circles display similar results based on the Lambertian assumption. Because snow is known to have strongly bidirectional reflectance, the Lambertian assumption is invalid. In spite of this, the assumption is widely used for computational simplicity.

Figure 4.9 shows that the retrieval results become worse under the Lambertian assumption. When bidirectional reflectances of snow is accounted for, the bias is very small for albedo (Figure 4.9a), upward (Figure 4.9b), downward (Fig-

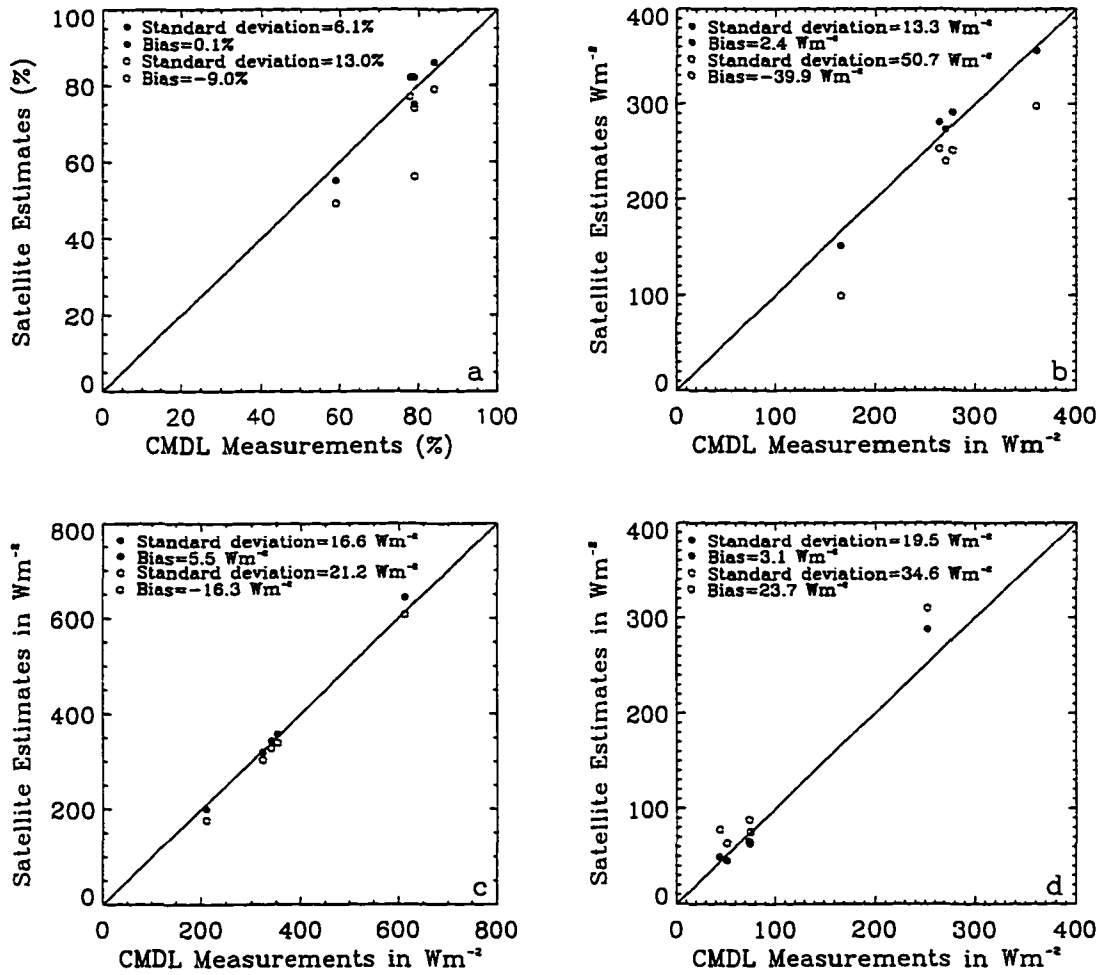


Figure 4.9 Scatter plots of satellite estimates versus CMDL field measurements for (a) albedo, (b) upward irradiance, (c) downward irradiance, and (d) net irradiance at Earth surface for snow with bidirectional reflectances (solid point) and with Lambertian assumption (circle).

ure 4.9c) and net irradiances (Figure 4.9d), being 0.1%, 2.4 Wm^{-2} , 5.5 Wm^{-2} and 3.1 Wm^{-2} , respectively. The bias increases dramatically when the Lambertian (isotropic) assumption is invoked, being 9.0% for albedo (Figure 4.9a), -39.9 Wm^{-2} for upward irradiance (Figure 4.9b), -16.3 Wm^{-2} for downward irradiance (Figure 4.9c) and 23.7 Wm^{-2} for net irradiance (Figure 4.9d), respectively. It is also evident from Figure 4.9a, b, c and d that the standard deviation for the inferred albedo, upward, downward and net irradiances, obtained when the surface is treated properly as a bidirectional reflector (6.1%, 13.3, 16.6, and 19.5 Wm^{-2} , respectively) is much smaller than when it is taken to be a Lambertian (isotropic) reflector (13.0%, 50.7, 21.2, and 34.6 Wm^{-2}).

In Figure 4.9a, surface albedo is underestimated by as much as 30% with the Lambertian assumption compared to a snow surface with bidirectional reflectance properties. This is consistent with the results derived by *De Abreu et al.* (1994) over snow-covered sea ice. This can also be explained by the patterns of the anisotropy factor shown in Figure 4.3. Figure 4.3c reveals that neglecting anisotropy will lead to an overestimation (the value of the anisotropy factor larger than 1.0) for a satellite zenith angle larger than 30° , if measured in the forward-scattered direction, while an underestimation (the value of the anisotropy factor less than 1.0) can be expected for the backscattered direction or near vertical observations. According to Table 4.1, the 3rd, 4th and 5th points have the relative azimuth angle ϕ less than 90° , which means the measurement was taken in the backscattered direction, so the surface albedos retrieved from the three measurements are expected to be underestimated. Also in Table 4.1, the 1st and 2nd measurements were taken in the forward-scattered direction ($\phi > 90^\circ$), while the

satellite zenith angles are smaller than 30° . Thus, the surface albedos inferred from the two measurements are expected to be underestimated. As a result, the upward flux is underestimated by as much as 40% (Figure 4.9b), and the net flux is overestimated by as much as 75% (Figure 4.9d) compared to those obtained over surfaces with bidirectional reflectance properties. Figure 4.9c shows that the downward flux has the smallest change because it is mainly determined by the solar elevation and the state of atmosphere and is insensitive to surface conditions.

4.5 Discussion

Mie theory relies on the assumption that individual snow grains scatter as spheres in each other's far field. In real situation, snow grains are rarely spheres. *Wiscombe and Warren* (1980) pointed out that the details of the angular scattering pattern (phase function) are the most sensitive to nonsphericity, whereas the cross section for absorption and scattering are likely to be much less sensitive to nonsphericity than is the phase function at specific angles. *Mugnai and Wiscombe* (1980) have studied these cross sections theoretically for randomly oriented moderately nonspherical particles and find them to be quite close to those for equal-volume spheres. Thus, *Wiscombe and Warren* (1980) have argued that it is reasonable to assume spherical snow grains, because the scattering of irregularly shaped particles can be mimicked by spheres of appropriate size. This assumption may be not representative of natural snow layers on some occasions, for example, a snow surface with vertically oriented frost needles or plates, or a snow surface that is wet or has refrozen after being wetted. *Wiscombe and Warren* (1980) also argued that

near-field effects or close packing are unlikely to be important for visible or near-infrared spectral regions because the distance between snow particles is generally larger than the wavelength of incident radiation. Figure 4.9a shows that the inferred snow surface albedo obtained by including snow bidirectional reflectance in the radiative transfer model agrees very well with the ground-based measurements.

The opposition effect is not included for snow surfaces. Figure 3.2 in chapter 3 shows that the amplitude of the hot spot ($B(\Theta)$ given in equation (3.16)) depends on solar zenith angle, and it becomes small when θ_0 is large ($\theta_0 > 60^\circ$). Moreover, *Ahmad and Deering* (1992) found that $B(\Theta)$ strongly depends on the incident zenith angle from observations. They modify the Hapke shadowing function by multiplying $B(\Theta)$ by θ_0 in equation (3.16). θ_0 is greater than 60° in most of cases in this study. Large solar zenith angles also occur frequently in the Arctic. Thus, neglecting the opposition effect may only lead to minor errors in the retrieval of arctic surface albedo from AVHRR data.

Figure 4.8 shows there is some scatter between inferred tundra surface albedo and ground-based measurements. Part of the scatter is probably due to the Lambertian approximation for tundra surfaces. *Saunders* (1990) found that albedos of snow-free land inferred from AVHRR data assuming isotropy were within 1% of those calculated applying the *Taylor and Stowe* (1984) anisotropic correction factor, when solar zenith angle and satellite zenith angle both are less than 45° . It was also found by *Saunders* (1990) that when the Taylor and Stowe factors were applied to the cases with $\theta_0 > 65^\circ$, large discontinuities in the resultant surface albedo were obtained. As discussed by *Saunders* (1990), the Taylor and Stowe factors are derived from a much smaller set of observations (less than 25 per angular

bin) for $\theta_0 > 60^\circ$, whereas for $\theta_0 < 53^\circ$ there are usually well over 100 observations per angular bin. So the Taylor and Stowe factors for large solar zenith angles are not so representative as for the smaller solar zenith angles. Uncertainties in the anisotropic scattering of land surfaces will only be resolved by measurements from a satellite or aircraft radiometer which is able to view the surface from a variety of different viewing angles and for a wide range of solar zenith angles. Once the optical properties of land surfaces, e.g., single scattering albedo and phase function, are estimated, the bidirectional reflectance can be simulated by our model described in chapter 3 and further be included in the comprehensive radiative transfer model to infer surface albedo correctly with no need for the anisotropic correction.

4.6 Summary

An algorithm is developed to retrieve broadband surface albedo and solar irradiances from satellite observed narrowband radiances. The algorithm is different from the traditional methods based on empirical anisotropic corrections. Instead, it relies on a comprehensive radiative transfer model in which radiative transfer simulations are carried out by the DISORT code applicable to a plane-parallel atmosphere. The surface property is adjusted in the model calculation until the resultant TOA radiance matches the satellite observations. No *ad hoc* “anisotropic correction” is necessary. The algorithm is specifically designed for arctic conditions. Bidirectional reflectance is correctly accounted for when the underlying surface is covered by snow.

The retrieved surface albedo and irradiances are compared with ground-based

observations. Good agreement exists generally between the retrieval results and the observations. It is found that accounting for the bidirectional reflectance of the underlying snow surface significantly improves the quality of the overall retrieval results. For a snow surface, accounting for the bidirectional reflectance appears to give a clear advantage over the Lambertian assumption that is commonly adopted.

Cloud-free images of satellite radiances are very difficult to find in the Arctic because of the persistent occurrence of clouds in Arctic summer and winter. However, inspection of large volumes of satellite data over the Arctic will reveal relatively frequent cloud-free areas within images. In this study we were able to identify 19 cloud-free areas over Barrow, Alaska, that could be co-located with surface CMDL measurements. Although only 19 cloud-free cases are used for testing purposes in this study, they represent two different surface types characterized as tundra in summer and snow in winter, and they cover the period of snow melt. The favorable comparison of our retrievals with the surface measurements gives us confidence that the algorithm presented in this study can be applied to cloud-free AVHRR scenes throughout the Arctic.

Chapter 5

Remote Sensing of Water Cloud Parameters in the Arctic from AVHRR Measurements

Liquid water path (LWP), effective particle radius and cloud top temperature are three important parameters for water clouds. In the shortwave the optical depth is proportional to the ratio of the liquid water content (LWC), and the effective radius. Thus, knowledge of LWC and effective radius allows us to infer the optical depth.

These parameters of clouds are difficult to estimate due to their temporal and spatial variability. Satellite remote sensing techniques are necessary for a global knowledge of these parameters. There are a number of investigations aimed at determining cloud optical depth and effective particle radius from visible and near-infrared measurements using radiometers deployed on satellites. Recent works

include *Platnick and Twomey, (1994)*, *Han et al., (1994)*, *Nakajima and Nakajima, (1994)*, and *Platnick and Valero, (1994)*. The principle behind these techniques is based on the fact that the reflection function of clouds at a nonabsorbing channel in the visible wavelength region is primarily a function of the cloud optical depth, whereas the reflection function at a water absorbing channel in the near-infrared is primarily a function of cloud droplet size.

At high latitudes, the surface is covered by snow/ice most of the time throughout a year. Solar radiation reflected by clouds over snow/ice surfaces in the visible is not sensitive to cloud optical depth because of the low contrast between cloud and surface albedo, and the multiple reflections between cloud base and the underlying snow/ice surface.

Key (1995) used the AVHRR near-infrared channel 2 at $0.85 \mu\text{m}$ to infer water cloud optical depth for cloud over snow/ice surfaces, based on the premise that the reflected solar radiation at $0.85 \mu\text{m}$ is primarily a function of water cloud optical depth. The reflected solar radiation at channel 3 ($3.7 \mu\text{m}$) was used by *Key (1995)* to retrieve cloud effective radius, while the thermal component at channel 3 was removed by using the measurement of channel 4. The Lambertian approximation is adopted for snow surfaces under cloudy conditions in *Key's (1995)* algorithm. *Lubin et al. (1994)* proposed an empirical parameterization for cloud optical depth as a function of the brightness temperature difference between AVHRR channel 3 and 4 ($11 \mu\text{m}$), which was derived for cloud fields over the ocean and applied to nearby cloud fields over snow and ice in Antarctica.

The objective of the present study is to develop algorithms, suitable for Arctic conditions, to infer water cloud optical depth, effective particle radius and cloud

top temperature. The combination of channels 1, 3 and 4 is selected for the retrieval over dark ground surfaces like ocean and tundra, while the combination of channel 2, 3 and 4 is selected for bright ground surfaces like snow and ice. The bidirectional reflectance of snow surfaces is taken into account in the same way as in chapter 4. The Lambertian approximation is not used. We begin with a discussion of the principle of cloud remote sensing in section 5.1. The retrieval algorithms are described in section 5.2 followed by a sensitivity analysis in section 5.3. In section 5.4 we apply the algorithms to AVHRR images over North Slope of Alaska for validation, and then present the retrieved cloud optical depth, effective radius and cloud top temperature over arctic ocean, tundra and snow/ice surfaces. A discussion and summary are given in section 5.5.

5.1 The Principles of Cloud Remote Sensing

5.1.1 Radiative Transfer Model

Radiative transfer models form the theoretical basis of cloud retrieval algorithms. In our study, we adopt the discrete-ordinate radiative transfer code (DISORT) developed by *Stamnes et al.* (1988). Aerosol loading includes Arctic haze (0-3 km), tropospheric aerosol (3-10 km) and stratospheric aerosol (10-30 km). In our plane-parallel model, the atmosphere is divided vertically into 33 layers: below 8 km local radiosonde sounding profiles are used, and a sub-arctic summer and winter model atmosphere *McClatchey et al* (1971) is employed for atmospheric layers above 8 km. 3 spectral intervals are used for channel 1, 4 for channel 2, 9 for channel 3,

and 7 for channel 4. The calculated radiance is weighted by the spectral response function of each channel (*Kidwell, 1995*). Surface types include ocean, tundra and snow/ice. Ocean and tundra surfaces are treated as Lambertian (isotropic) reflectors while snow/ice surfaces are treated as one additional vertical layer when we carry out radiative transfer calculations. We employ the optical properties of snow obtained by *Wiscombe and Warren (1980)*; *Warren and Wiscombe (1980)*. The most important variable controlling snow albedo is the mean grain size. More details about the radiative transfer model are given at section 4.3.

Cloud effective radius (r_e , μm) is defined as

$$r_e = \frac{\int n(r)r^3 dr}{\int n(r)r^2 dr} \quad (5.1)$$

where $n(r)$ is the cloud droplet size distribution. We use the generalized gamma distribution as follows:

$$n(r) = \frac{N_0}{\Gamma(\gamma)r_m} \left(\frac{r}{r_m}\right)^{\gamma-1} \exp(-r/r_m). \quad (5.2)$$

Another quantity characterizing cloud microphysics is the liquid water content (LWC , $g \cdot \text{cm}^{-3}$), defined as follows:

$$LWC = \frac{4\pi\rho_w}{3} \int n(r)r^3 dr \quad (5.3)$$

where ρ_w ($g \cdot \text{cm}^{-3}$) is the density of water. The cloud droplet effective radius r_e and the liquid water content LWC can be related empirically to the single scattering albedo a , extinction coefficient k and the asymmetry factor g , in the following forms of parameterization (*Hu and Stamnes, 1993*):

$$k/LWC = a_1 r_e^{b_1} + c_1 \quad (5.4)$$

$$1 - a = a_2 r_e^{b_2} + c_2 \quad (5.5)$$

$$g = a_3 r_e^{b_3} + c_3. \quad (5.6)$$

Cloud optical depth is defined as

$$\tau = \int_{z_1}^{z_2} k dz \quad (5.7)$$

where z_1 is the cloud base and z_2 is the top. The liquid water path is simply $LWP = LWC(z_2 - z_1)$. The cloud liquid water content LWC is explicitly used in the radiative transfer model, but it cannot be directly retrieved from satellite data. However, the optical depth, τ , can be estimated, and as mentioned previously the cloud optical depth is proportional to LWP and inversely proportional to the effective radius in the visible.

The principles for cloud retrieval over dark surfaces like ocean and tundra, and bright surfaces like snow and ice will be discussed separately.

5.1.2 Water Cloud over Ocean or Tundra

Figure 5.1 shows that the reflected solar radiance in channel 1 depends primarily on the cloud optical depth (upper panel), and the reflected solar radiance in channel 3 depends primarily on the effective radius (lower panel) when the cloud is sufficiently thick ($\tau > 3$). This can be explained by the fact that the magnitude of the imaginary index of refraction of liquid water in channel 3 (about 10^{-3}) is much larger than that in channel 1 (about 10^{-9}). This results in much stronger liquid water absorption in channel 3 than in channel 1. Therefore, the reflected radiance of channel 3 is sensitive to cloud droplet size and is approximately proportional to

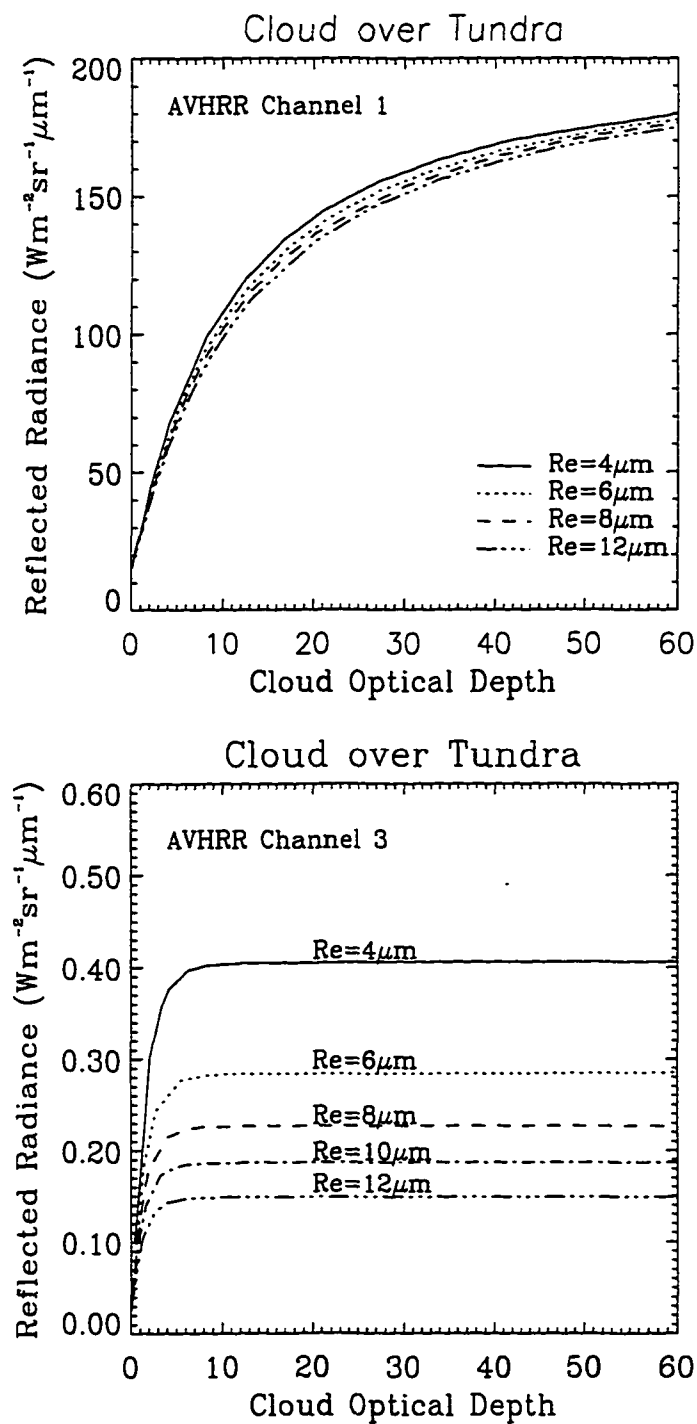


Figure 5.1 Reflected radiance for (a) AVHRR channel 1, and (b) AVHRR channel 3 for various effective radius as a function of cloud optical depth. Calculations are for the azimuth angle of $\phi=50^\circ$, satellite zenith angle $\theta=10^\circ$ and solar zenith angle $\theta_0=60^\circ$, respectively. Lambertian visible surface albedo is 0.1.

droplet radius. The sensitivity is larger than at 1.6 or 2.2 μm (an order of magnitude less absorption at 2.2 μm than at 3.2 μm) where the thermal contribution to the radiance is negligible. Figure 5.1 also indicates that multiple solutions occur when τ is small.

In channel 3, however, the thermal radiation emitted by ground and cloud layers is comparable to the reflected solar radiance for typical cloud particle size encountered. Figure 5.2 plots simulated radiances in channel 3 as a function of optical depth in the case of (1) no thermal radiation, (2) with ground thermal radiation, (3) with cloud thermal radiation, and (4) with both ground and cloud thermal radiation. This figure illustrates that the contribution of ground thermal radiation is large when cloud optical depth is less than 10, and that the contribution of cloud thermal radiation is obvious when optical depth is greater than 2. The effect of ground thermal radiation together with cloud thermal radiation is profound even in the case of a thin cloud (optical depth less than 1). Therefore, we have to take into account the thermal component by including the thermal channel at 11.0 μm (channel 4) for inferring cloud top temperature, as discussed below.

The brightness temperature of AVHRR channel 4 as a function of cloud optical depth is plotted in Figure 5.3 for various cloud top temperature, effective radius, and ground temperatures. Channel 4 brightness temperature converges to ground temperature when cloud is thin and τ is close to zero since ground surfaces can be roughly treated as a black body in channel 4. The brightness temperature converges to cloud top temperature when the cloud is thick since the emissivity of a thick cloud is nearly equal to 1. This property makes channel 4 an ideal channel for retrieval of cloud top temperature. For cloud containing large droplets

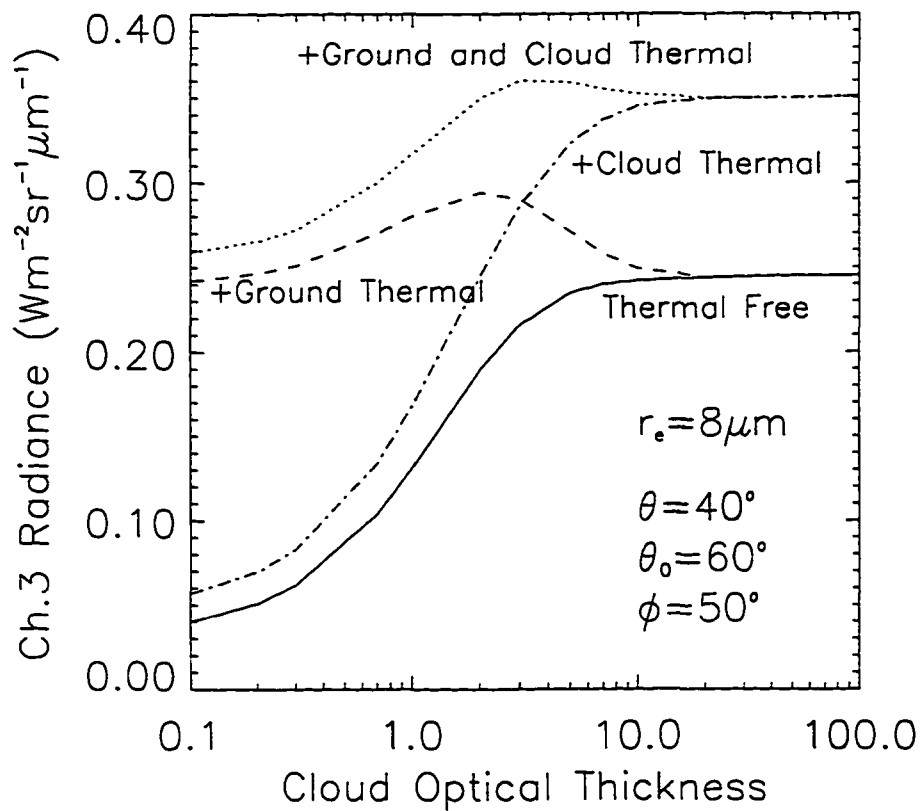


Figure 5.2 Simulated radiances of AVHRR channel 3 as a function of cloud optical depth in the case of (1) no thermal radiation, (2) with ground thermal radiation, (3) with cloud thermal radiation, and (4) with both ground and cloud thermal radiation, for a surface temperature $T_g=288.2$ K, cloud top temperature $T_c=275.2$ K, and surface albedo $A_g=0.0$.

(effective radius greater than $10 \mu\text{m}$), the channel 4 brightness temperature has little to do with cloud particle size. When cloud optical depth is greater than 5, the channel 4 brightness temperature is not sensitive to ground temperature.

In summary, through measurements of AVHRR channel 1, 3 and 4 we can retrieve cloud optical depth, effective radius and cloud top temperature of water clouds over ocean and tundra in the Arctic.

5.1.3 Water Cloud over Snow or Ice

For clouds over highly-reflecting surfaces like snow and ice, the radiance in AVHRR channel 1 is no longer primarily a function of cloud optical depth. Figure 5.4 shows that ground reflectance significantly contributes to the radiance measured by satellites in channel 1, and that the reflected radiation in channel 1 is not sensitive to cloud optical depth when surface albedo is large. This can be explained by the strong multiple reflection between cloud base and underlying snow/ice surface.

However, the channel 2 radiance depends primarily on cloud optical thickness for cloud over snow/ice, as shown in Figure 5.5 (upper panel). The lower panel indicates that the reflected radiance in channel 3 is primarily a function of effective radius for cloud over snow or ice, which is similar to the case of cloud over ocean and tundra. This is because the albedo of a snow surface drops sharply in near-infrared wavelength.

Similarly, the thermal radiation in channel 3 can be estimated by using the thermal channel at $11.0 \mu\text{m}$ (channel 4) for inferring cloud top temperature. In summary, through measurements of AVHRR channel 2, 3 and 4 we can retrieve

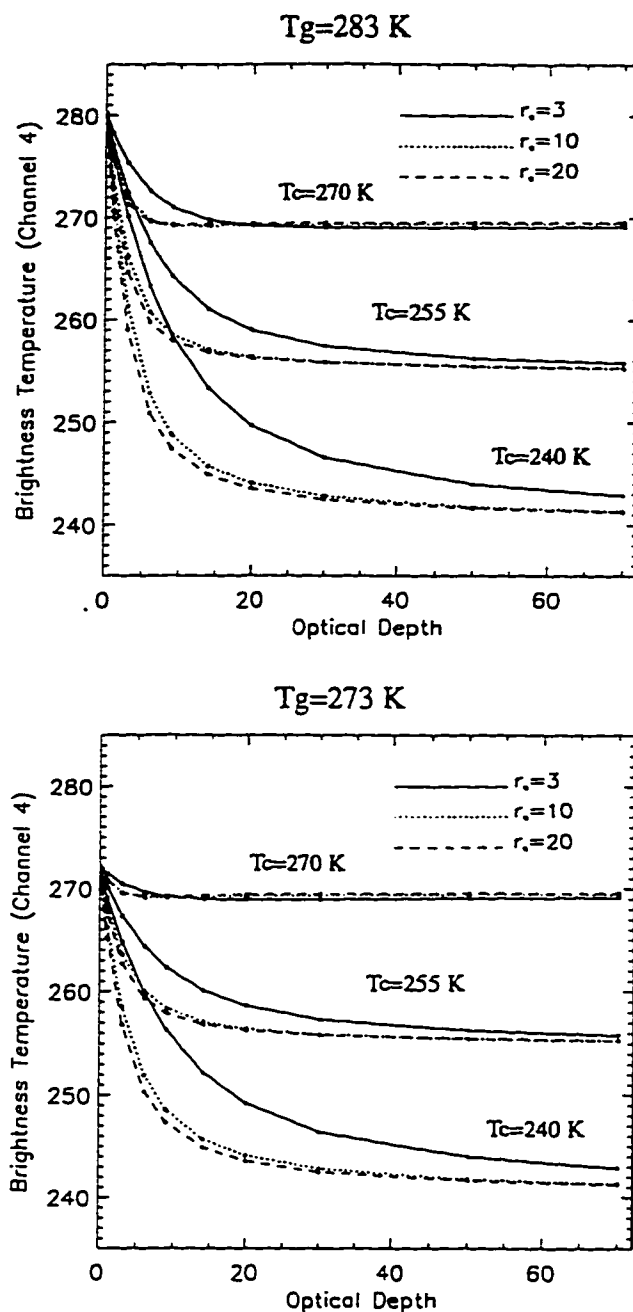


Figure 5.3 Brightness temperature of AVHRR channel 4 for various cloud top temperature and effective radius as a function of cloud optical depth for a surface temperature of 273 K (lower panel) and 283 K (upper panel).

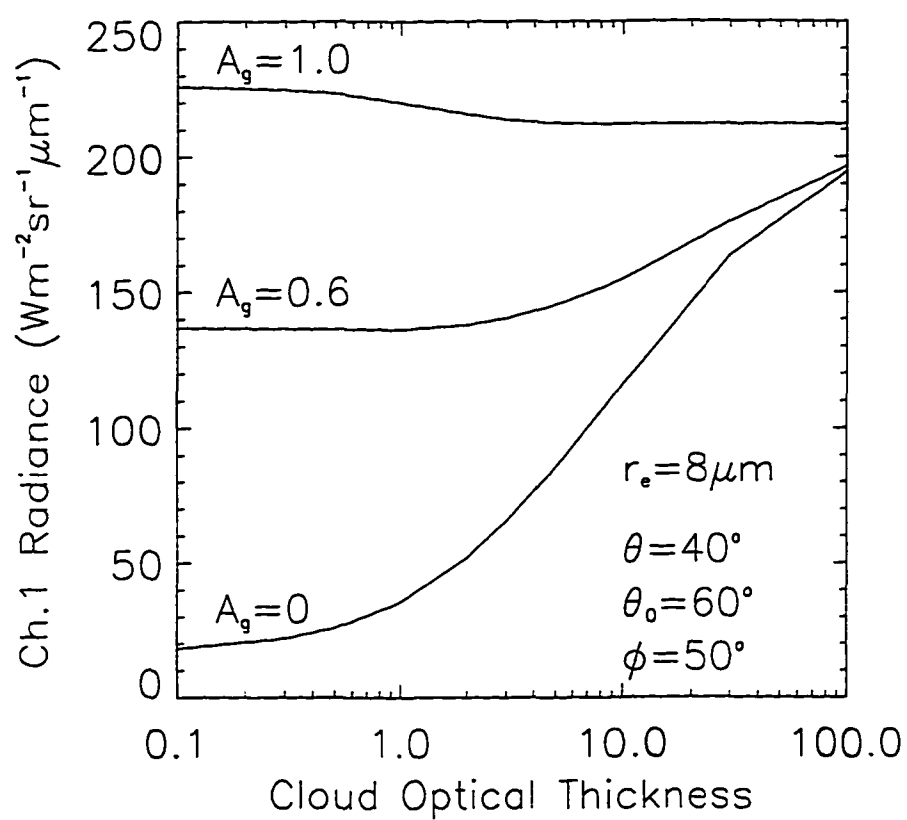


Figure 5.4 Simulated radiances of AVHRR channel 1 as a function of cloud optical depth and surface albedo A_g .

optical depth, effective radius and cloud top temperature of water cloud over snow and ice in the Arctic.

Key (1995) assumed snow as a Lambertian reflector. It is found that multiple solutions occur when solar zenith angle is large. Figure 5.6 indicates that accounting for bidirectional reflectance of snow does improve the quality of the retrieval algorithm as compared with the Lambertian approximation.

5.2 Description of Retrieval Algorithm

We use lookup tables to maintain accuracy of the retrieval and save computation time. The retrieval is implemented by finding the best match between the measured satellite radiance for the pixel being analyzed in the AVHRR image and an entry in the lookup table. Lookup tables are generated by radiative transfer calculations. Two different retrieval procedures are designed for two different surface types: ocean/tundra and snow/ice.

5.2.1 Water Cloud over Ocean or Tundra

To reduce the size of the lookup tables, first we need to know to what quantities the reflected radiation in the AVHRR channels are most sensitive. According to *Han et al.* (1994), cloud effective radius is important for the solar reflectance in channel 3 only, and cloud top temperature (T_c) is important for thermal radiation in channel 3 and channel 4, but not for solar reflectance in channel 1 and channel 3. The effect of T_c on channel 1 and channel 3 solar reflectance is determined by gaseous absorption and Rayleigh scattering above the cloud top since a change in cloud

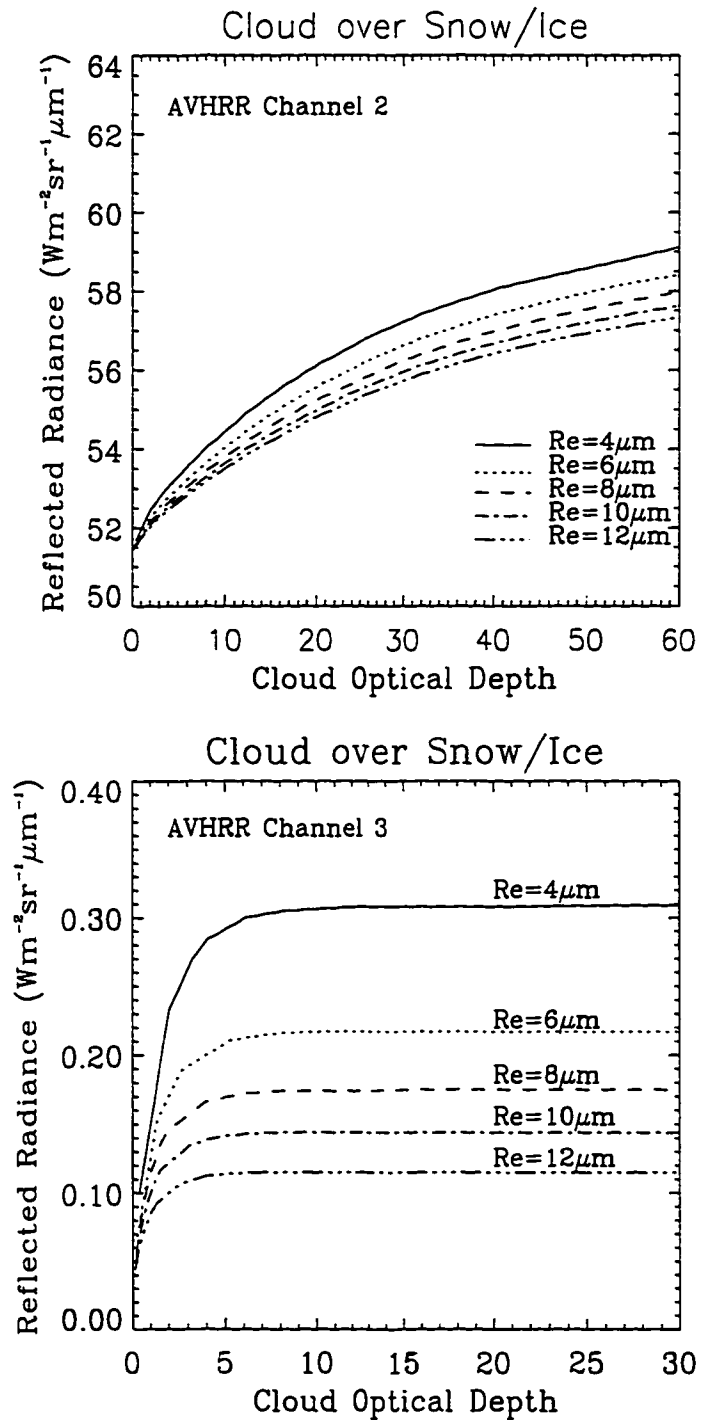


Figure 5.5 Reflected radiance for (a) AVHRR channel 2, and (b) AVHRR channel 3 for various effective radius as a function of cloud optical depth. Calculations are for the azimuth angle of $\phi=50^\circ$, satellite zenith angle $\theta=10^\circ$ and solar zenith angle $\theta_0=70^\circ$, respectively. Snow grain size is assumed to be $100\mu m$ which corresponds to a surface visible albedo of 0.95.

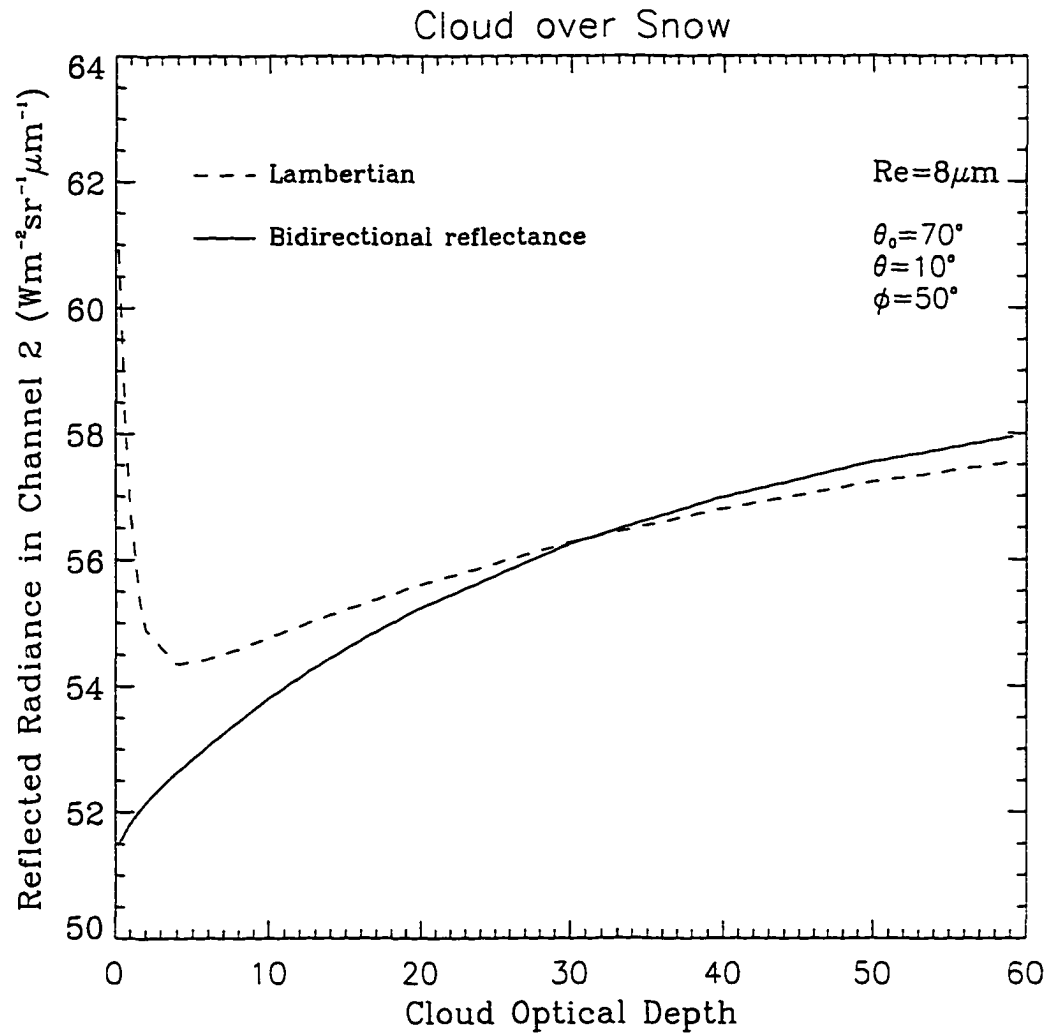


Figure 5.6 Reflected radiance in AVHRR channel 2 as a function of cloud optical depth. Calculations are for the azimuth angle of $\phi=50^\circ$, satellite zenith angle $\theta=10^\circ$ and solar zenith angle $\theta_0=70^\circ$, respectively. Snow grain size is assumed to be $100 \mu\text{m}$ which corresponds to a surface albedo of 0.87 in AVHRR channel 2. Solid line represents the calculations from the model that accounts for bidirectional reflectance of snow, and dotted line represents the calculations from the model that assumes Lambertian reflector for snow. Cloud effective radius is $8 \mu\text{m}$.

top temperature implies a change in cloud top height, and hence a change in the amount of gas above the cloud top. In channel 1, variation of the gas amount above the cloud top changes the Rayleigh scattering contribution slightly. In channel 3 the variation of water vapor amount changes the solar radiation absorbed by water vapor above the cloud top. Only the air above the cloud absorbs or scatters radiation observed by satellites because water clouds have large albedo at visible wavelengths and are strong absorbers at $3.7 \mu\text{m}$, so that not much sunlight can reach the gas under the cloud. Cloud optical depth is important for the solar reflectance in channel 1, and channel 3 when the cloud is thin, which is illustrated in Figure 5.1. The thermal component of channel 3 is also sensitive to cloud optical depth, and channel 4 radiance is sensitive to τ when the cloud is thin, as demonstrated in Figure 5.3. Since ground reflectance significantly contributes to the radiance measured by satellites in channel 1 (shown in Figure 5.4), accurate estimation of surface albedo in channel 1 is needed. Surface ground temperature has little effect on channel 4 brightness temperature when the cloud is thick, and can be determined by channel 4 brightness temperature from a clear sky pixel (shown in Figure 5.3).

Four tables are generated for retrieval of cloud over tundra. They are Table 1': channel 1 radiance as a function of surface albedo for clear sky, Table 1: channel 1 radiance as a function of cloud optical depth and surface albedo for the specific field), Table 3: channel 3 radiance as a function of cloud optical depth, effective radius, cloud top temperature, and ground temperature, and Table 4: channel 4 radiance as a function of cloud optical depth, effective radius, cloud top temperature, and ground temperature. Dependences of the radiances on solar zenith

angle, satellite viewing angle, and relative azimuth angle between the Sun and the satellite are also taken into account in all the tables.

Figure 5.7 is a flow chart of the retrieval algorithm for cloud over ocean or tundra. First of all, a clear-sky image is selected to determine the surface albedo A_g of the tundra surface from Table 1' and the observed channel 1 radiance $R_{sat,ch1}$. For ocean surfaces, the albedo remains nearly constant when solar zenith angle is less than 60° . Thus it is fixed to be 0.06, which is also used for cloud retrieval at mid and low-latitudes (*Platnick and Valero, 1995*).

In step 2, one assumes that the surface albedo under cloudy skies is about the same as when the clear sky image was taken. The surface albedo obtained in step 1 together with channel 1 radiance in the cloudy image is then used to compute cloud optical depth τ from Table 1.

In step 3, a value for cloud effective radius r_e is obtained from Table 3 with the cloud optical depth obtained in step 2, an initial value of cloud top temperature T_c which is assumed to be equal to the brightness temperature in channel 4, the observed channel 3 radiance $R_{sat,ch3}$, and the ground temperature T_g as input of Table 3. The ground temperature T_g can be found through channel 4 brightness temperature at nearby clear pixels.

In step 4, a value for cloud top temperature T'_c is obtained from Table 4 with the cloud optical depth obtained from step 2, effective radius obtained in step 3, and observed channel 4 radiance $R_{sat,ch4}$ as input. If the difference between this improved estimate for cloud top temperature and the initial value $\Delta T_c = |T_c - T'_c|$ is large, we have to go back to step 2 with the improved T'_c as the new initial value of cloud top temperature to get a new set of cloud effective radius and cloud top

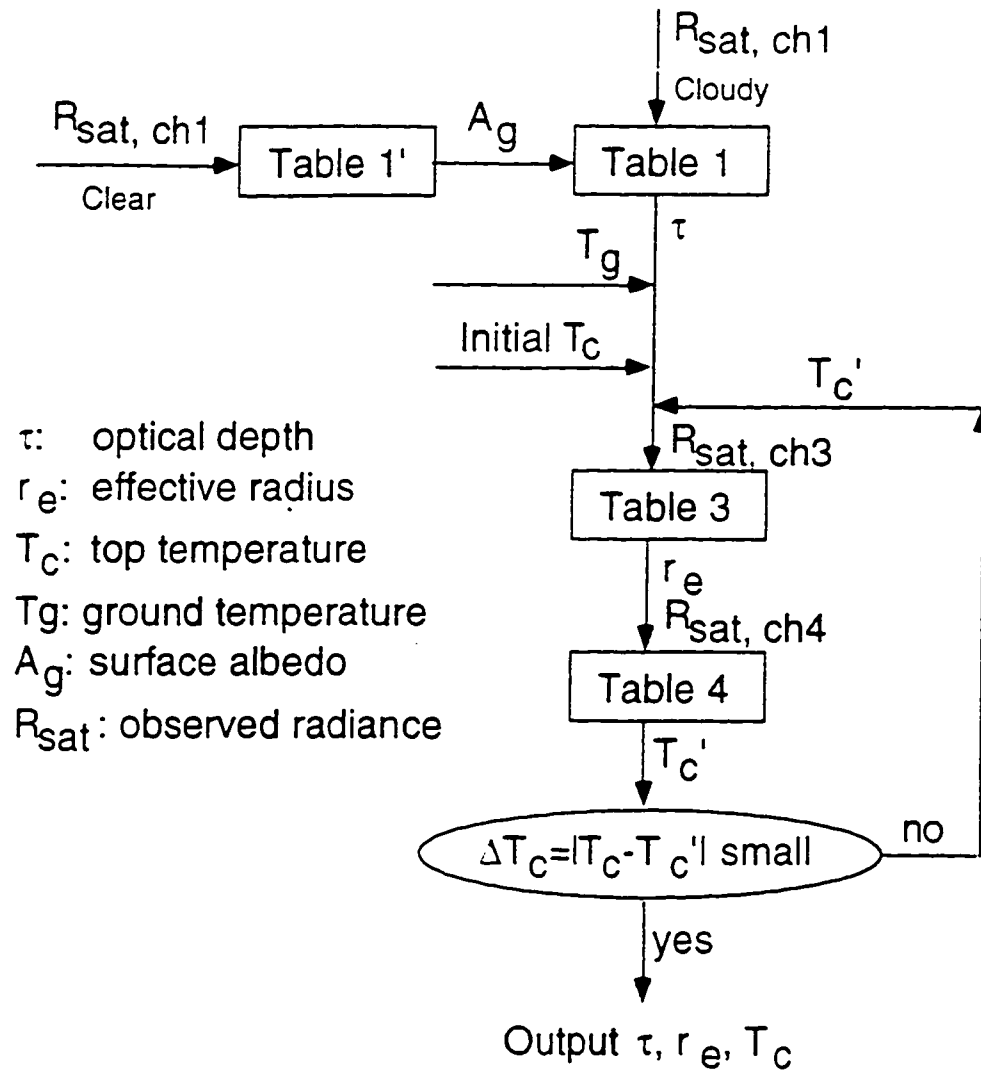


Figure 5.7 Flow chart of retrieval algorithm for water cloud over ocean and tundra. Note that A_g is fixed to be 0.06 for ocean.

temperature. The iteration ends when ΔT_c is less than 0.1. The three parameters τ , r_e , and T_c are then obtained through steps 1 and 2, and the iteration of steps 3 and 4. Generally, the iteration converges after two or three rounds.

5.2.2 Water Cloud over Snow or Ice

As in to the case of cloud over tundra, four tables are prepared for the retrieval of cloud parameters over snow or ice. They are Table 2': channel 2 radiance as a function of snow grain size under clear sky, Table 2: channel 2 radiance as a function of cloud optical depth, effective radius and snow grain size, Table 3: channel 3 radiance as a function of cloud optical depth, effective radius, cloud top temperature, and ground temperature, Table 4: channel 4 radiance as a function of cloud optical depth, effective radius, cloud top and ground temperatures. The dependences of the radiances in channel 2, 3 and 4 on solar zenith angle, satellite viewing angle and relative azimuth angle between the Sun and satellites are also taken into account in these tables. Making these lookup tables takes more computational time than those for the case of cloud over ocean and tundra since a larger stream number is necessary for the radiative transfer computations to account for the bidirectional reflectance of the snow/ice surfaces.

A flow diagram of the retrieval algorithm for cloud over snow and ice is shown in Figure 5.8. The procedure is quite similar to that for cloud over ocean and tundra with some important differences. As the first step, the grain size of the underlying snow surface is retrieved from a clear-sky channel 2 image and Table 2'.

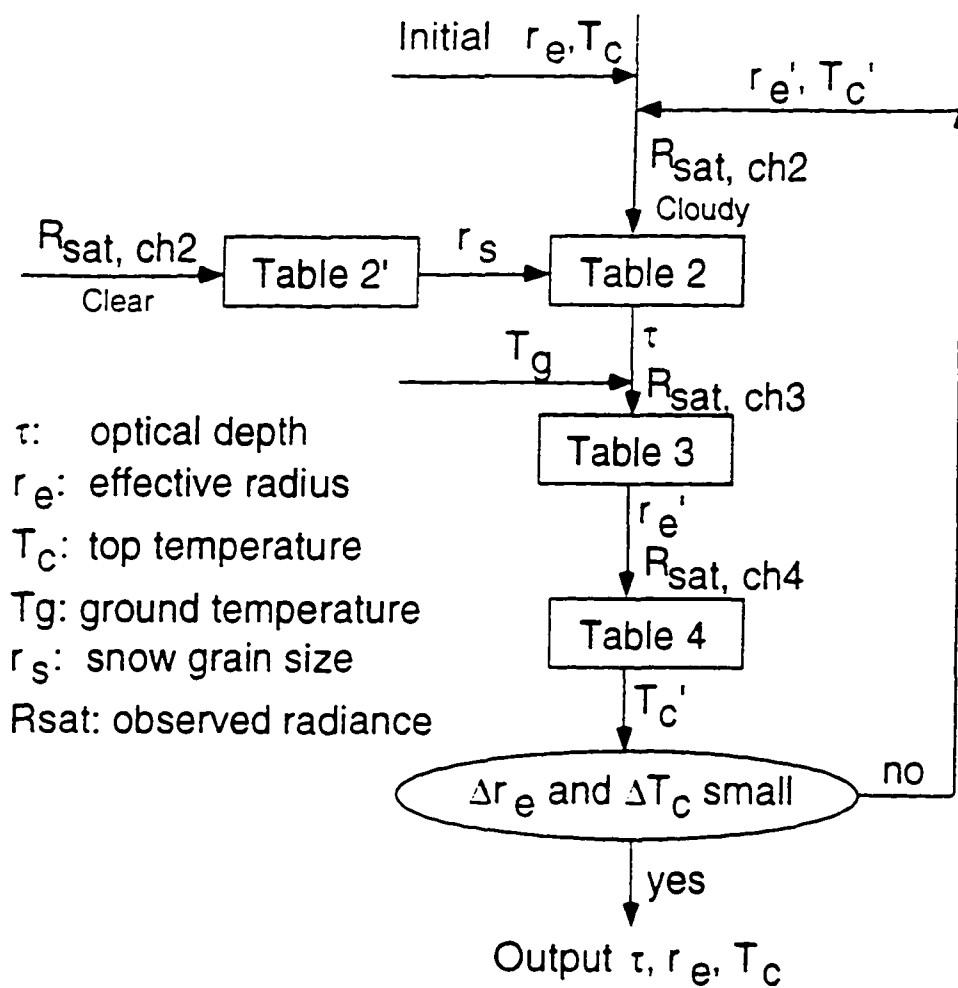


Figure 5.8 Flow chart of retrieval algorithm for water cloud over snow and ice.

In step 2, an estimated value of cloud optical depth is obtained from Table 2 with an initial value of cloud effective radius and observed channel 2 radiance in the cloudy sky as input. Note that this may not be the final retrieval result for optical depth.

In step 3, an estimated value of cloud effective radius is obtained from Table 3 with the cloud optical depth estimated in step 2, an initial value of cloud top temperature (brightness temperature in channel 4), ground temperature, and observed channel 3 radiance as input.

In step 4, an estimated value of cloud top temperature is obtained from Table 4 with the cloud optical depth estimated in step 2, effective radius estimated in step 3, ground temperature, and observed channel 4 radiance as input.

If differences between the estimated values and the given initial values are large, we will go all the way back to step 2 and repeat steps 2, 3 and 4 with the estimated value replacing the initial values. This iteration ends when the differences are small ($\Delta r_e < 0.1$ and $\Delta T_c < 0.1$). The iteration usually converges after three or four rounds, which is one or two times more than that for cloud over ocean and tundra.

5.3 Uncertainty Analysis

5.3.1 Uncertainty in the Retrieval of Optical Depth

Part of the error in the retrieved cloud optical depth comes from the error in the surface albedo. The upper panel of Figure 5.9 shows the sensitivity of the retrieved optical depth to the error in surface albedo for cloud over tundra or

ocean. Consider a surface albedo $A_g = 0.06$ with an uncertainty of ± 0.04 . The retrieved cloud optical depth is larger if $A_g = 0.10$ than if $A_g = 0.06$, and the difference between the two is a function of the cloud optical depth itself. This function is shown by the line above the zero error line. On the other hand, the retrieved cloud optical depth is smaller if $A_g = 0.02$ than if $A_g = 0.06$. The difference as a function of τ is represented by the other line in the upper panel of Figure 5.9. The plot shows that the resulting error in the cloud optical depth is small (below 20%) when $\tau > 3$. However, the error can be very large when $\tau < 3$, for example, the error is 60-70% when $\tau = 1$.

The major error source for the retrieval of optical depth is uncertainty in the observed radiances. The lower panel of Figure 5.9 shows the sensitivity of the retrieved cloud optical depth to uncertainties in channel 1 radiance for cloud over tundra or ocean. Suppose channel 1 radiance is 5% too large. The resulting error in the cloud optical depth incurred by this 5% error in channel 1 radiance is a function of the cloud optical depth itself, which is represented by a line in the lower panel of Figure 5.9. The other three lines in the plot have similar meanings. When cloud optical depth is larger than 2, a 5% error in channel 1 radiance may result in an error of around 10% in the optical depth. When the cloud is very thin ($\tau < 2$), the error can be quite large.

For cloud over snow or ice, the sensitivity of the retrieved optical depth to the snow grain size and channel 2 radiance is shown in Figure 5.10. The upper panel of Figure 5.10 shows variations in the retrieved τ for a variation of $100 \mu\text{m}$ in the snow grain radius as a function of τ itself. The larger the optical depth, the smaller is the resulting variation. When $\tau > 3$, the variation is below 20%. The error in

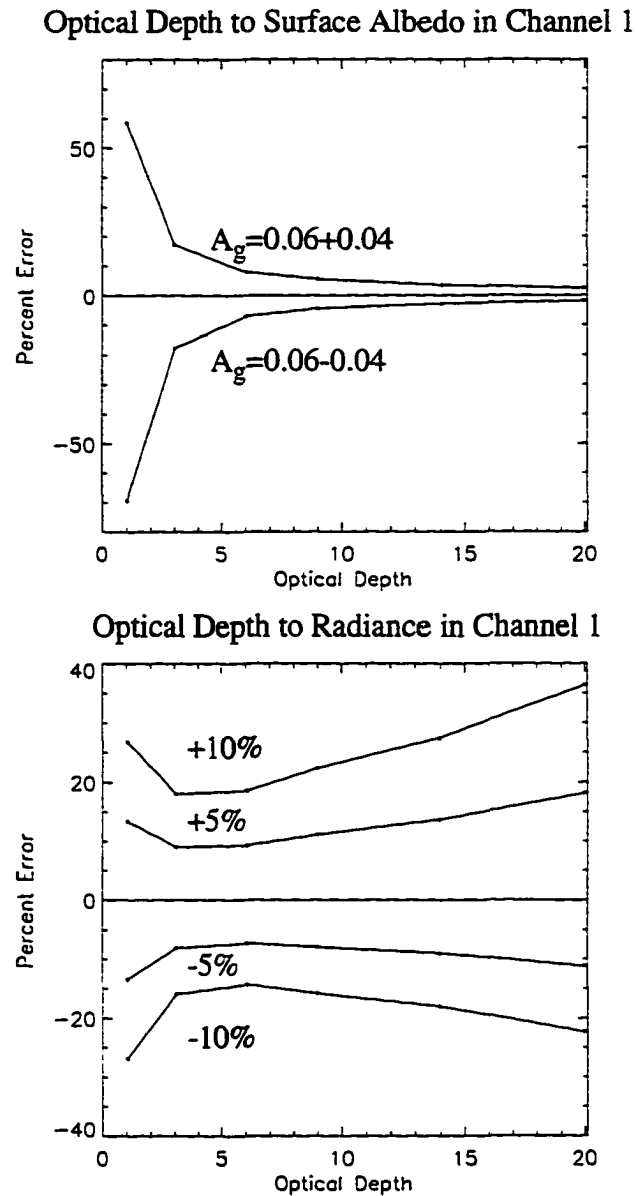


Figure 5.9 Error in retrieval of cloud optical depth over ocean and tundra as a function of optical depth for an uncertainty in surface albedo of 0.06 ± 0.04 (upper panel), and a $\pm 5\%$ or $\pm 10\%$ error in measured AVHRR channel 1 cloud radiance (lower panel).

retrieved optical depth can be very large when the value of optical depth is small ($\tau < 3$).

The lower panel of Figure 5.10 shows the resulting error in the cloud optical depth for a given error in channel 2 radiance. When $\tau > 3$, the error in optical depth is mostly below 40% for a 4% error in the channel 2 radiance. The error can be over 100% when $\tau < 3$. Figure 5.10 also shows that retrieved cloud optical depth over snow is much more sensitive to cloud top radiance than that over ocean or tundra.

5.3.2 Uncertainty in the Retrieval of Effective Radius

Surface reflectance has little effect on the retrieval of effective radius because snow, ocean and tundra all have very low albedo in channel 3. Uncertainties in channel 3 radiance are the primary source of uncertainty in the retrieved cloud effective radius. Since the algorithms for cloud retrieved over tundra/ocean and over snow/ice both use channel 3 radiance and the same principle to retrieve the effective radius, their uncertainties may be the same. It is found through model calculations that a $\pm 10\%$ error of the channel 3 radiance may result in an error of around $\mp 10\%$ on the retrieved effective radius when the effective radius is larger than $3 \mu\text{m}$ for optically thick clouds ($\tau > 6$). When the effective radius is smaller than $3 \mu\text{m}$, the error of the retrieved value can be very large.

There exist other error sources in the retrieved cloud effective radius, as discussed by *Han et al.* (1994). They include uncertainties caused by horizontal inhomogeneity of the cloud, multilayered cloud structure, cirrus and aerosol con-

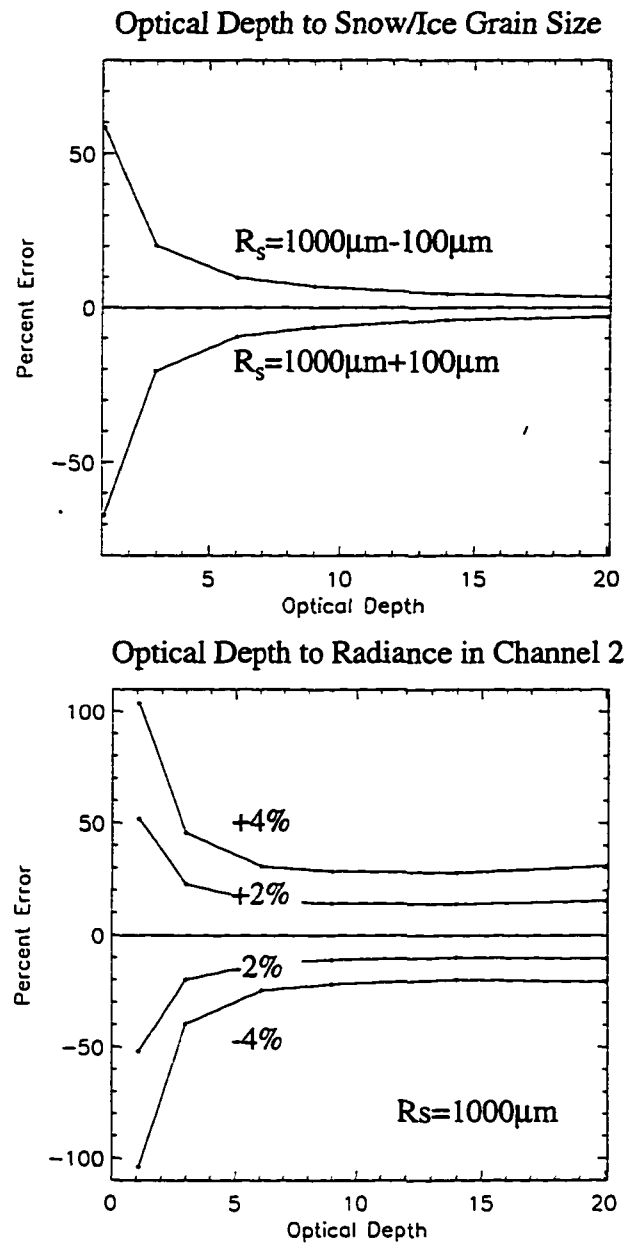


Figure 5.10 Error in retrieval of cloud optical depth over snow and ice as a function of optical depth for an uncertainty in snow/ice grain size of $1000 \pm 100 \mu\text{m}$ (upper panel), and a $\pm 2\%$ and $\pm 4\%$ error in measured AVHRR channel 2 cloud radiance (lower panel).

tamination and random errors.

The retrieval scheme of cloud top temperature used in our study is similar to that used in the International Satellite Cloud Climatology Project (ISCCP). Uncertainties in ISCCP-retrieved cloud top temperature are caused by the treatment of water vapor effects, cloud effects, and the homogeneity of the cloud, as discussed by *Han et al.* (1994). The uncertainties associated with water vapor effects are small since the amount of water vapor decreases rapidly with altitude, so that not much of the water vapor is above the cloud top. Errors caused by the inhomogeneity of the cloud are also small because of the similarity of brightness temperatures of low-level clouds and clear sky, according to *Han et al.* (1994).

The investigation by *Key and Haeffliger* (1991) indicated that the attenuation of upwelling infrared radiation in the polar atmosphere is small because of the low atmospheric humidity. Either of channel 4 or 5 alone could be used to derive ice surface temperature. Failure to account for atmospheric correction can result in an ice surface temperature underestimate of 1.5-2.1 K in channel 4 and 1.9-3.2 K in channel 5.

In summary, the major error for both optical depth and effective radius comes from the uncertainty in cloud top radiance which in turn comes from uncertainties in calibrations of AVHRR sensors and radiative transfer calculations. For thick clouds with large value of optical depth and $r_e > 3\mu\text{m}$, the retrieval results have small errors and are reliable. However, the error can be very large for thin clouds when $\tau < 3$ and $r_e < 3\mu\text{m}$.

5.4 Applications and Results

To demonstrate the utility of our retrieval algorithms, we have analyzed AVHRR images taken over the North Slope of Alaska and the Chukchi Sea, and compared the results with ground-based measurements at Barrow, Alaska.

5.4.1 Data

We have used NOAA-11 AVHRR High Resolution Picture Transmission (HRPT) data with a spatial resolution of 1.1 km at nadir. Since the AVHRR sensors of channels 1 and 2 have been degrading in orbit, the post-launch calibration coefficients by *Rao and Chen* (1995) are adopted to convert the raw count recorded by AVHRR sensors to radiance, as follows:

$$R_1 = 0.5496(C_{10}(1) - 40) \exp(0.33 \times 10^{-4}d) \quad (5.8)$$

$$R_2 = 0.3680(C_{10}(2) - 40) \exp(0.55 \times 10^{-4}d). \quad (5.9)$$

Here R_1 and R_2 are calibrated radiances of channels 1 and 2, respectively, in units of $Wm^{-2}sr^{-1}\mu m^{-1}$, d is the day from launch, $C_{10}(1)$ and $C_{10}(2)$ are measured signals in 10-bit counts for channels 1 and 2, respectively. *Rao and Chen* (1995) also reported that the accuracy in the radiance calculated using equations (5.8) and (5.9) is on the order of a few per cent.

According to NOAA calibration procedures described in section 2.2.2, the calibration error of channel 4 is about 0.12 K around 300 K and larger at lower temperature, about 1-2 K at 250 K. The uncertainty in channel 3 calibration is similar to that of channel 4.

Solar irradiance measurements at the surface are available for Barrow, Alaska (71°18' N, 156°47' W) (shown in Figure 5.11) by NOAA CMDL. Broadband downwelling irradiance is measured over the wavelength range 0.3 - 2.8 μm . The measurement is hourly-averaged. The uncertainty in the measurements is less than 2% for solar zenith angle smaller than 60° as stated in section 2.3.

Radiosonde sounding data at Barrow are obtained at the National Weather Service (NWS) Office. These data provide profiles of pressure, temperature, dew point temperature, wind speed and wind direction up to 6-8 km.

5.4.2 Testing

There are no *in-situ* data of cloud optical depth or effective radius available for testing. However, we approach this problem by testing higher level parameters, the solar downwelling irradiance at the surface. There are no direct observation of cloud top temperature. However, we can derive cloud top temperature from radiosonde sounding data, and compare them with the retrieval results.

For cloud over tundra, Figure 5.12 plots satellite estimated downwelling irradiance versus ground-based CMDL measurements. The irradiance is an integration for the whole solar spectral band. The ground-based observations are made in Barrow, Alaska. The satellite estimates are obtained by using retrieved cloud parameters as input. Therefore, testing of the downwelling irradiance is an indirect validation of the retrieved cloud parameters. Good agreement is found. The standard deviation over the 17 data points is found to be 19.1%, and the bias is very small at 5.8 Wm^{-2} . The deviation is partly due to temporal and spatial mismatch

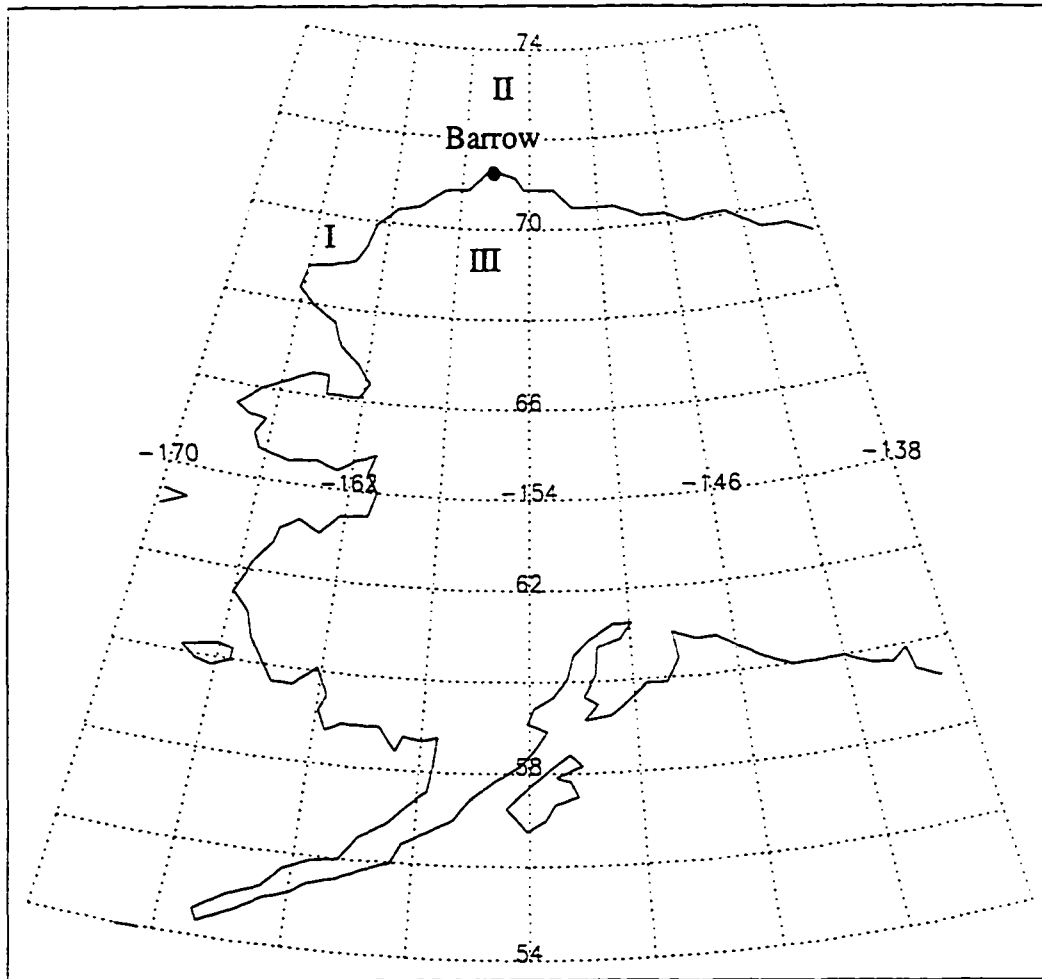


Figure 5.11 Cloud properties are retrieved in three different areas of $1^\circ \times 1^\circ$ each. Areas I, II, and III have ocean, snow/ice, and tundra as their underlying surface, respectively. The black point indicates the location of Barrow, Alaska where ground observations are made and the data are used for validation.

between the satellite and ground observations. Note that the ground observation is hourly averaged.

Figure 5.13 is similar to Figure 5.12 except that it is for the cases with clouds over snow. The satellite estimates agree well with the ground observations. The bias over the 12 data points is small, at 5.1 Wm^{-2} , about the same magnitude as the cases with clouds over tundra. The standard deviation is larger, at 32.1%, which indicates a larger error for the cloud retrieval over snow than over tundra.

Figure 5.14 is an example that illustrates how well one can determine cloud top and its temperature from localized radiosonde sounding data. The temperature profile T and dew point temperature profile T_d in the left panel are observed directly, and relative humidity RH in the right panel is derived by

$$RH = \frac{svp(T)}{svp(T_d)} \quad (5.10)$$

where svp represents saturation vapor pressure

$$svp(T) = 6.1078 \exp\left(\frac{T(19.846 - T(9.4027 \times 10^{-3} - 3.4442 \times 10^{-5}T))}{T + 273.0}\right). \quad (5.11)$$

Theoretically, the cloud top occurs at the bottom of the temperature inversion layer, and the relative humidity is close to 100% in cloud layers. In Figure 5.14, the relative humidity is high all the way up to the height of 2.8 km. At the same altitude, a temperature inversion occurs. The cloud top should be located right at the bottom of the temperature inversion layer. In Figure 5.14, the dashed line represents the cloud top where the temperature is found to be -20.3° C . From satellite retrieval, the cloud top temperature is -20.1° C , which corresponds to a cloud top height of 2.6 km according to the sounding temperature profile. The

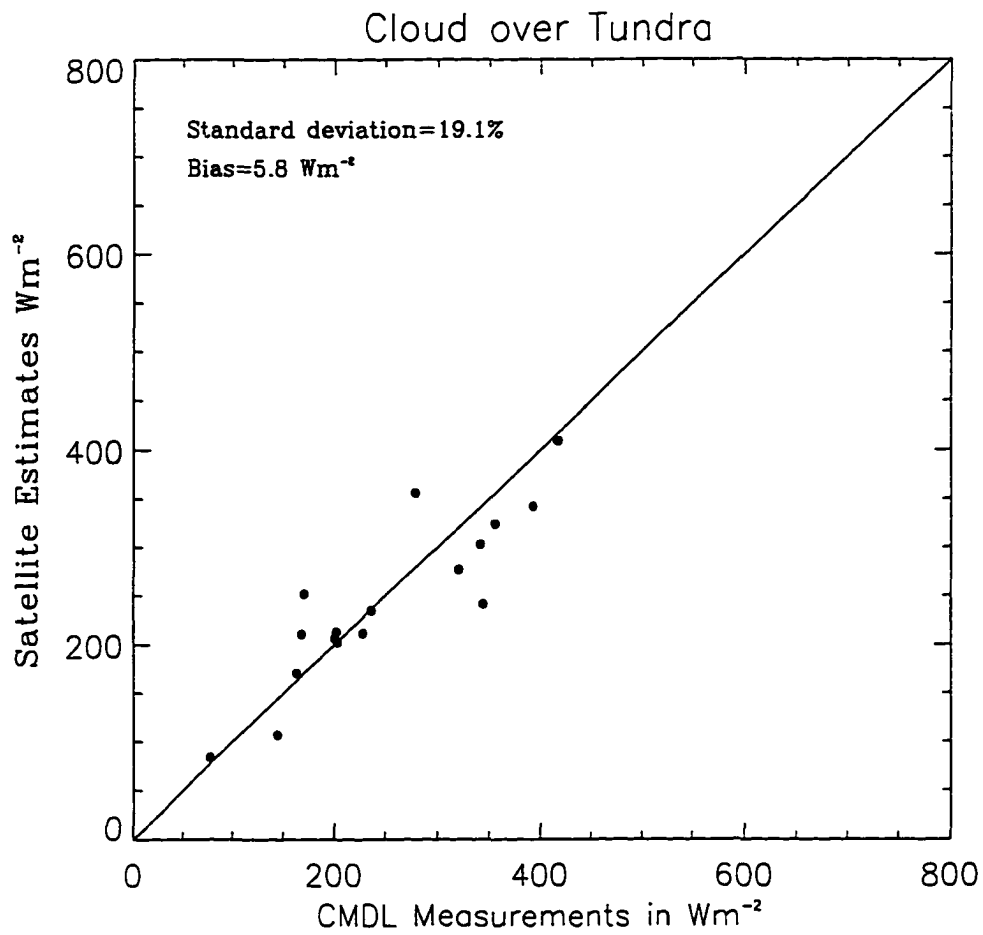


Figure 5.12 Scatter plot of satellite estimates versus ground-based CMDL measurements for solar downwelling irradiance over tundra. The satellite estimates of solar irradiance use the retrieved cloud parameters as input.

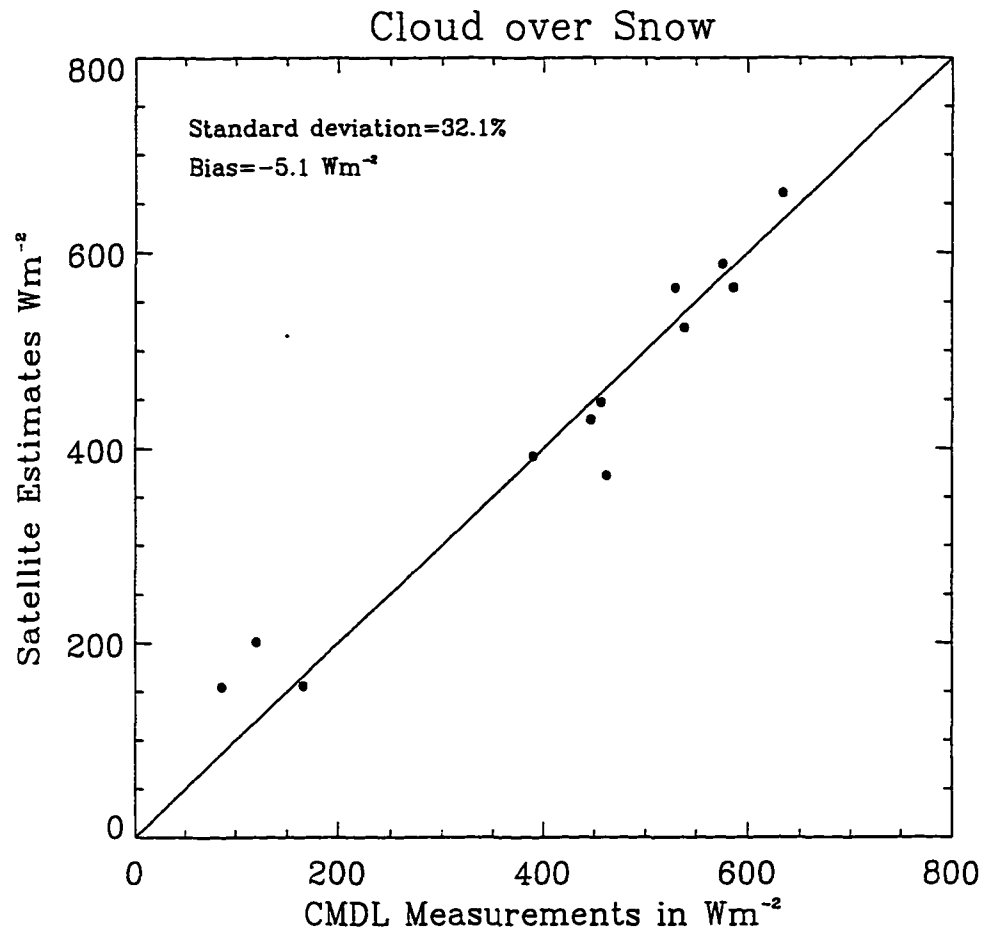


Figure 5.13 Same as Figure 5.12 but for clouds over snow.

retrieved cloud top temperature from satellite observation is very close to the value obtained from the sounding profiles.

Figure 5.15 summarizes such a validation for 9 different cases. The horizontal axis is the cloud top temperature estimated from sounding profiles, while the vertical axis is the corresponding value obtained from satellite remote sensing. There is very good agreements between the two. The standard deviation is found to be only 2.4° C, and the bias is 0.03° C. *Rossow et al.* (1989) found that the error from cloud top temperature retrieval is about $2\text{-}3^{\circ}$ C, which is about the same as our result. It should be mentioned that all the 9 cases used in Figure 5.15 have snow as the underlying surface. Cases with tundra as the underlying surface agree even better with the ground based sounding results.

5.4.3 Retrieval Results

We select two AVHRR observations that cover all the three areas shown in Figure 5.11. One of the observations is made at 2313 UTC 27 July 1992 with all clear sky. The other observation is made at 0013 UTC 23 July 1992 with mostly cloudy sky. The two observations are about 5 days apart and with small variation in solar zenith angle between the two images. The clear-sky observation is used to infer surface properties, albedo for tundra and grain size for snow. We assume that the surface properties are basically unchanged during the 5 days so that they can be used as input to retrieve cloud properties using the cloudy-sky observations.

Figure 5.16 displays the retrieval results for area I with ocean as its underlying surface. The solar zenith angle is around 53° . The surface albedo in channel 1 is

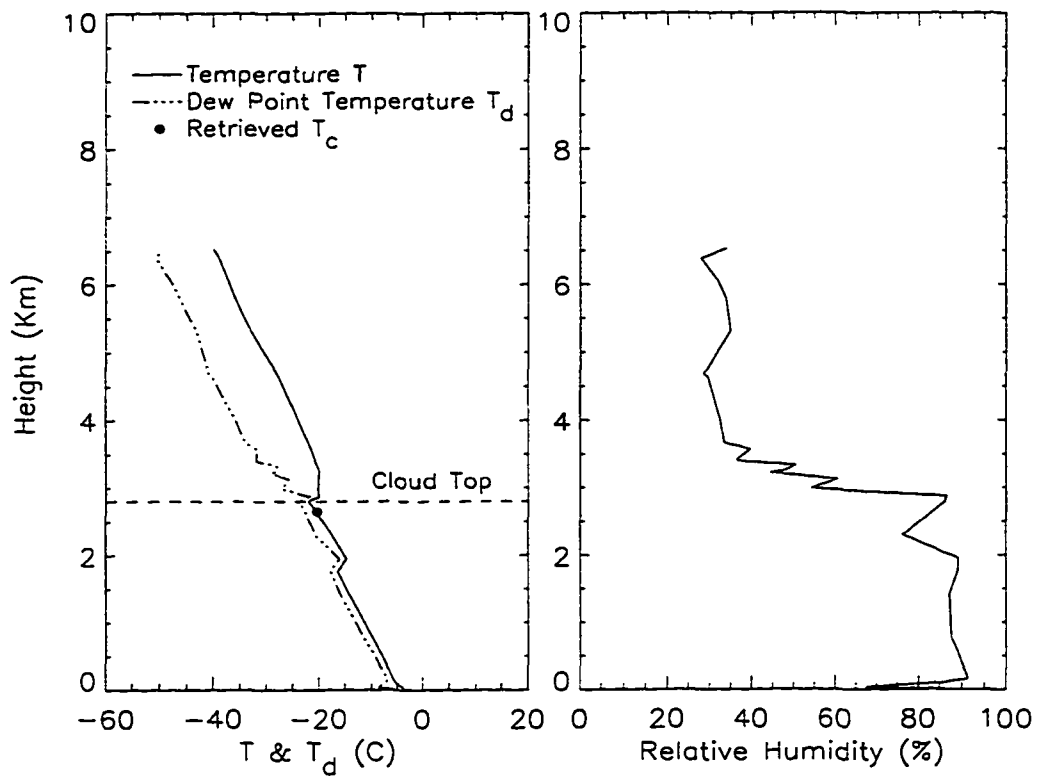


Figure 5.14 Profiles of temperature (solid line in the left panel), dew point temperature (triple-dot line in the left panel), and relative humidity (solid line in the right panel) at 0000 UTC 24 September 1992. The dashed line indicates the cloud top obtained from temperature inversion and relative humidity variation. The black point indicates the cloud top temperature obtained from the satellite estimate.

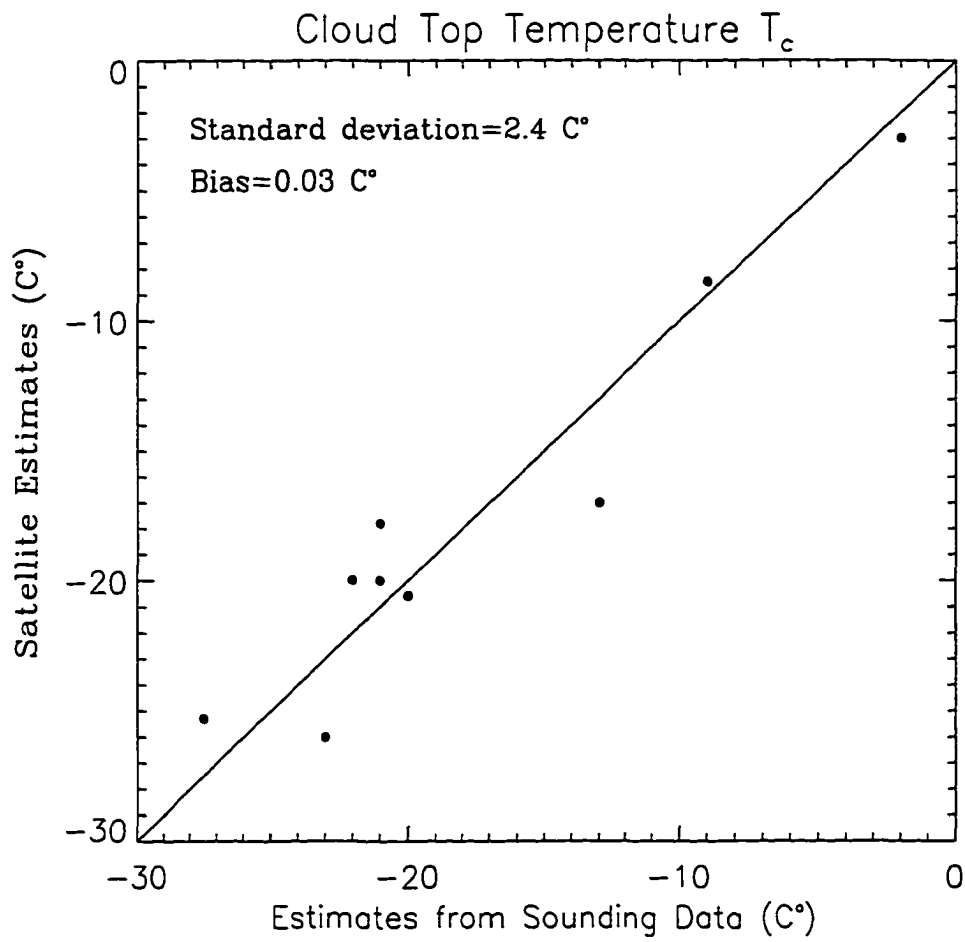


Figure 5.15 Scatter plot of satellite estimates versus ground-based sounding results for cloud top temperature.

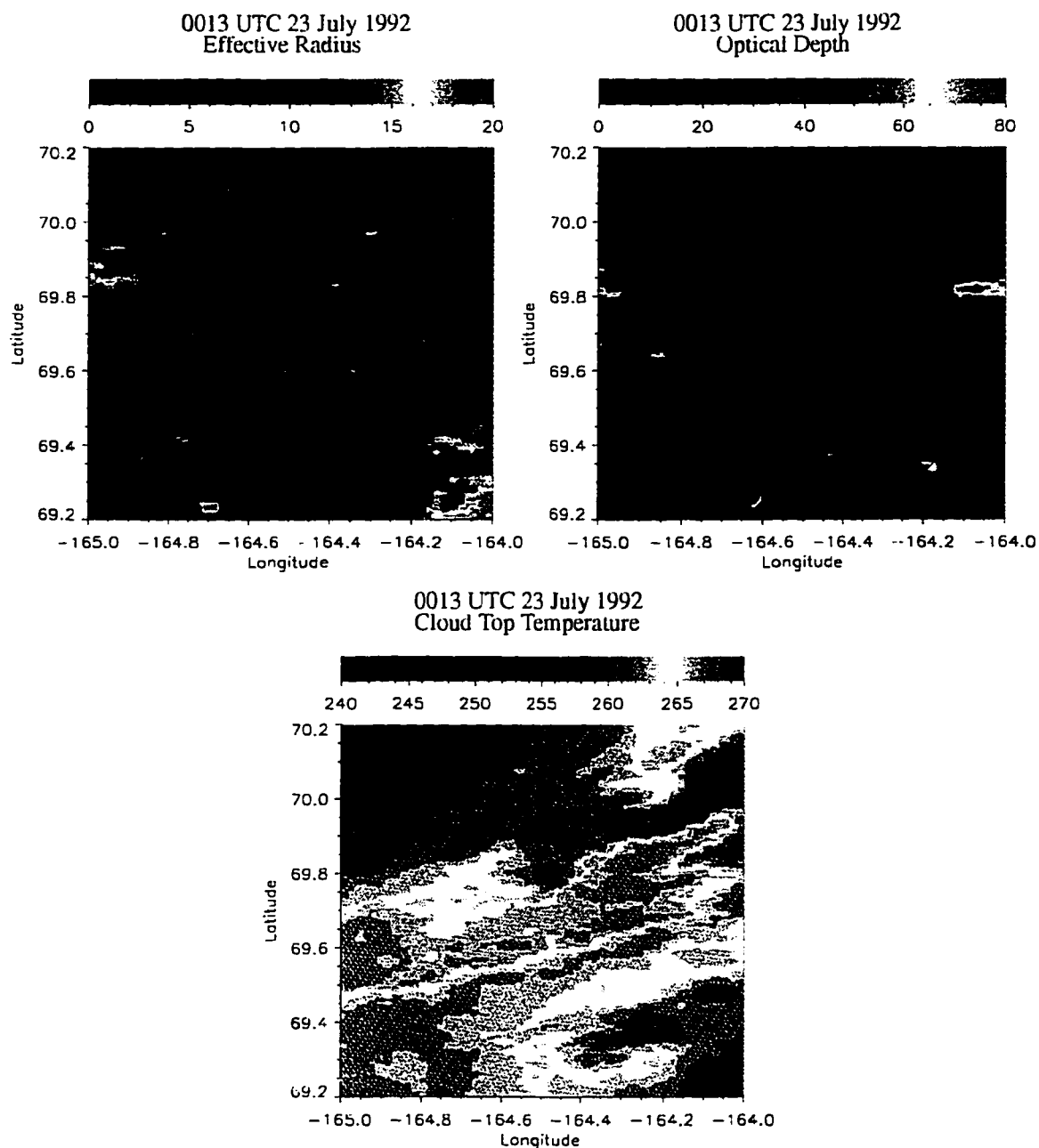


Figure 5.16 Derived images of cloud optical depth, effective radius (in μm), and cloud top temperature (in K) for area I as shown in Figure 5.11. The three images are derived from a cloudy image at 0013 UTC 23 July 1992. The underlying surface is ocean.

assumed to be 0.06. From the plot for cloud optical depth in the upper-right panel of Figure 5.16, it can be found that the area is completely covered with cloud, and the cloud is fairly thick in most of the area with an optical depth between 15 and 50. In a couple of regions, the cloud is extremely thick with a optical depth of about 70 and as large as 80. The cloud droplet size is shown in the upper-left panel of Figure 5.16. The droplet radius ranges from $5 \mu\text{m}$ to $15 \mu\text{m}$ in most of the area. Large droplet radius occurs in the lower-right corner of the area where the droplet radius is close to 18. A weak anti-correlation is found between the cloud optical depth and the droplet size. In the region of large cloud optical depth, the cloud droplet size tends to be small specifically for this case, but the relationship is not strong. From channel 4 brightness temperature of a neighboring area, the sea surface temperature is assumed to be uniform at 277 K. The lower panel of Figure 5.16 shows the retrieved cloud top temperature. The temperature is lower at the cloud top than at the surface of the ocean, lying mostly between 260 K to 270 K.

For area II with snow/ice as the underlying surface, the retrieval results are shown in Figure 5.17. The upper-left panel shows the snow grain size. Since it is July when ground temperature is around 0°C , the snow grain size is very large (nearly melting snow), around $1000 \mu\text{m}$. The plot for cloud optical depth indicates that the sky is partly cloudy in this area. Note that the black regions are cloud-free and the corresponding optical depth is zero. The cloud optical depth is below 13 in most of the area, while in some other regions it is up to 55. The cloud droplet radius mostly lies between $5 \mu\text{m}$ and $12 \mu\text{m}$. The cloud over the upper-left corner of the area has a large value of droplet radius, around $18 \mu\text{m}$. There seems to be

no clear correlation between the droplet size and the optical depth. The ground skin temperature is around 274 K. The retrieved cloud top temperature is found to be mostly around 267-271 K, slightly lower than the temperature of the ground. In some regions, the cloud top has a temperature about the same as the ground, which indicates a weak temperature inversion over the snow/ice underlying surface even in mid-summer.

Figure 5.18 has the same format of Figure 5.17, but it shows retrieval results for area III with tundra as its underlying surface. The channel 1 albedo (upper-left panel) is around 0.05 for the tundra surface when the solar zenith angle is 53° . Tundra surface albedo increases with the increase of solar zenith angle. The cloud is thin with optical depth smaller than 10 in most of the cloudy region. The plots for the cloud optical depth and droplet size show a positive correlation. The tundra skin temperature is relatively high in summer, about 293 K based on the brightness temperature in channel 4 from nearby clear pixels. The retrieved cloud top temperature is generally around 267 K, similar to that over the ocean. The dark areas indicate clear sky. In the areas neighboring clear sky where cloud is thin, the cloud top temperature is as high as 290 K, close to ground skin temperature.

Figure 5.19 displays the scatter plots of retrieved cloud effective radius versus optical depth for the three areas with different types of underlying surface. Based on a near-global survey of water cloud effective droplet radii, *Han et al.* (1994) found that cloud droplet radii generally increase with optical thickness for optically thinner clouds ($\tau < 20$) and decrease for optically thicker clouds. This picture is also evident in Figure 5.19. Over ocean, where τ overall is greater than 18, there is a slightly negative correlation between the two quantities. Over tundra, where τ

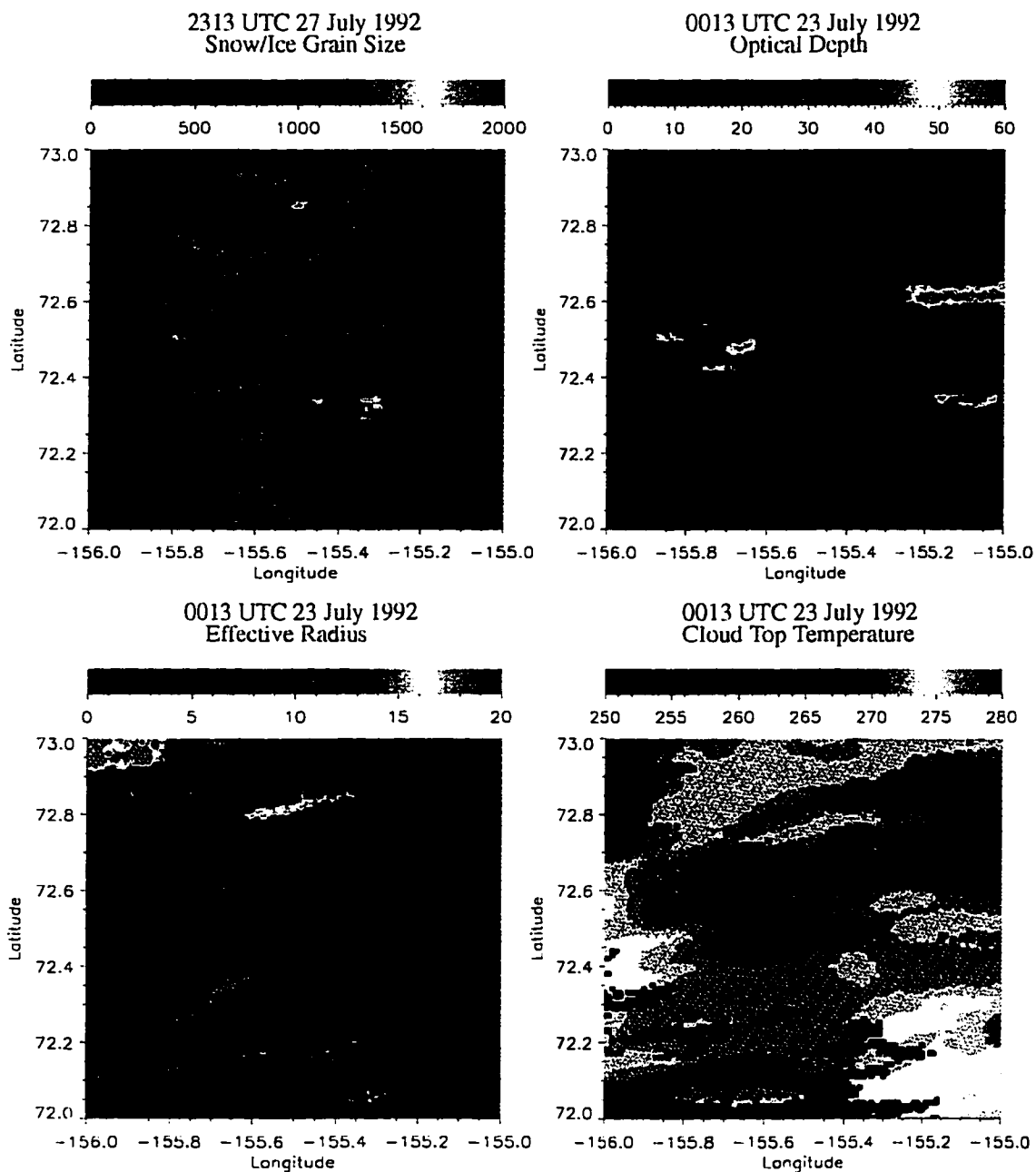


Figure 5.17 Derived images of snow grain size in (μm), cloud optical depth, effective radius (in μm), and cloud top temperature (in K) for area I as shown in Figure 5.11. The snow grain size is derived from a clear-sky satellite image at 2313 UTC 27 July 1992. The remaining three images are derived from a cloudy images at 0013 UTC 23 July 1992. The underlying surface is snow/ice. The black areas in the plots of optical depth, effective radius and top temperature represent clear sky.

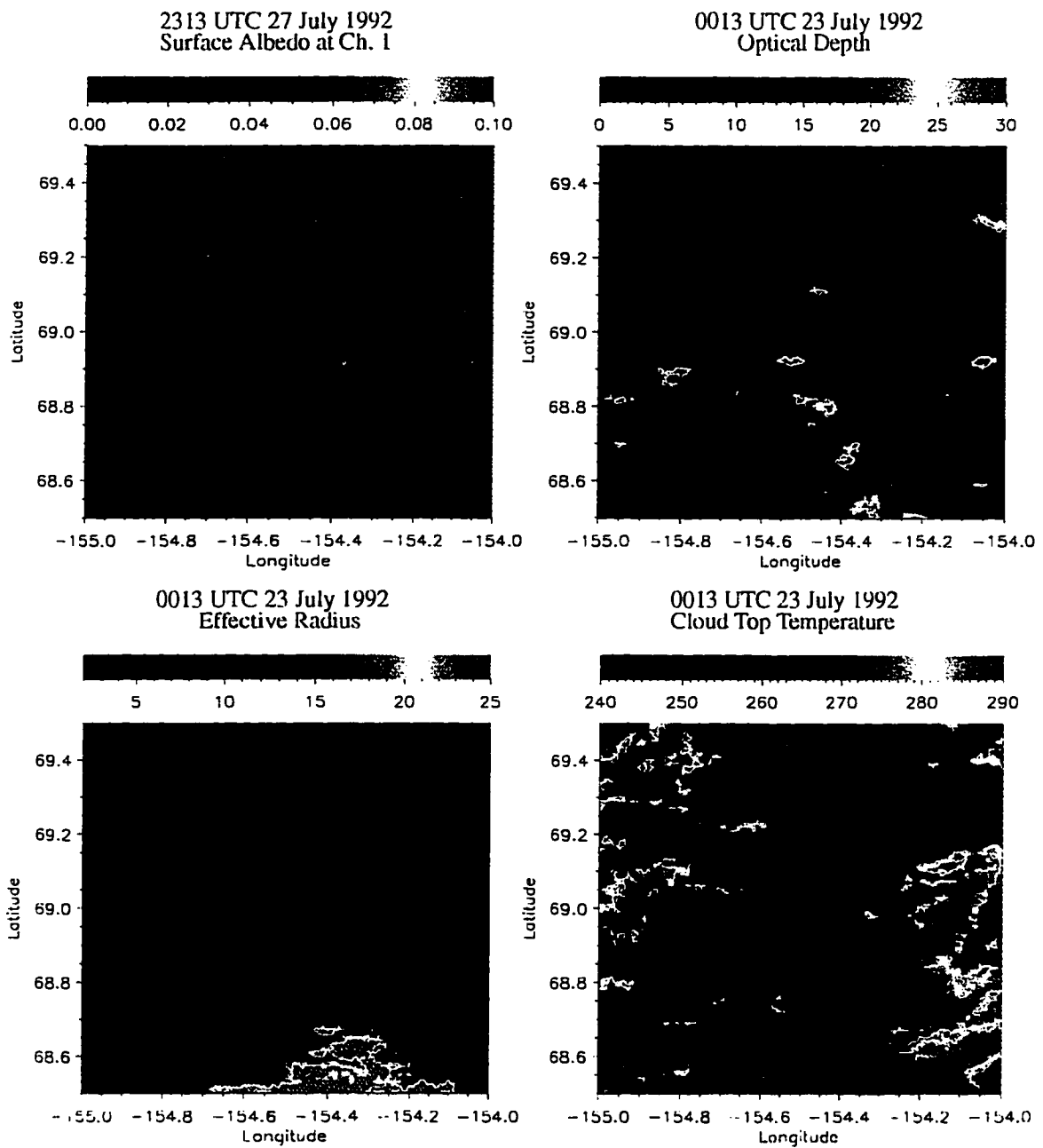


Figure 5.18 Same as Figure 5.16 except it is for area III with tundra as underlying surface and the upper-left panel represents surface albedo in channel 1.

overall is less than 20, there is a clearly positive correlation between the two. Over snow/ice τ has a wider range than over ocean and tundra, ranging from 3 to 60. There is a positive correlation between cloud droplet radius and optical thickness when $\tau < 20$ and a very weak negative correlation when $\tau > 20$ over snow/ice. The above relationship between cloud optical depth and effective radius indicates that both cloud optical depth and effective radius are needed to model cloud effects on radiation. Moreover, *Curry and Herman (1985)* compared aircraft observations to radiative transfer calculations and found that a single-parameter representation, such as liquid water path, did not work because of the variability of cloud particle sizes.

The frequency distribution of effective radius is shown in Figure 5.20 for the three different types of underlying surfaces. Over tundra, the effective radius concentrates between 4 and 11 μm , with the peak value of 18% at $r_e = 7 \sim 8 \mu\text{m}$. Over the ocean, the droplet size lies mostly between 6 and 12 μm with a peak value of close to 25% occurring at $r_e = 9 \sim 10 \mu\text{m}$. Over snow/ice, the effective radius is mostly between 5 and 12 μm , and the peak value of 17% occurs at $r_e = 10 \sim 11 \mu\text{m}$. From the three cases shown, we can see that effective radius for cloud over ocean is generally larger than cloud over land (tundra), which is also found in mid and low-latitudes (*Han et al., 1994*). The retrieved cloud effective radius is generally smaller than in mid and low-latitudes. This may be explained by the low atmospheric humidity in the Arctic. The near-global survey of effective radii in liquid water clouds using the International Satellite Cloud Climatology Project (ISCCP) by *Han et al. (1994)* also reveals that the mean cloud droplet radii changes from smaller values in the dry season (January) to larger values in

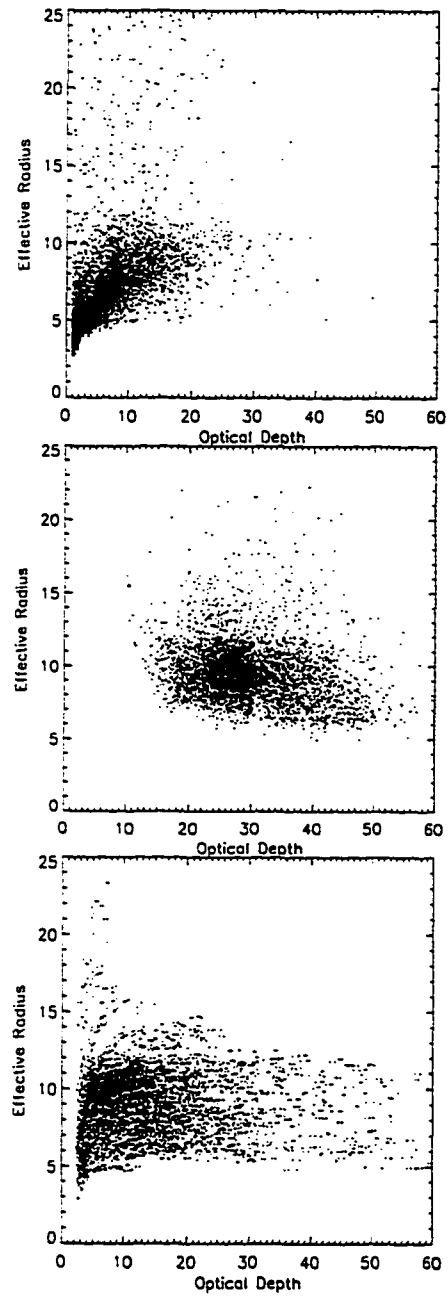


Figure 5.19 Scatter plots of retrieved cloud effective radius versus optical depth for areas I, II, and III with ocean (middle), snow (lower), and tundra (upper) as underlying surfaces, respectively.

the wet season (July). This behavior is consistent with an association of more frequent rainfall from low clouds with larger droplet sizes (*Albrecht, 1989*) and reduced CCN abundances due to precipitation scavenging (*Leitch et al., 1983*).

5.5 Summary

In this chapter, two algorithms are developed to retrieve cloud parameters. The basic features of the algorithms may be summarized as follows:

(1) One algorithm is developed for retrieval of clouds over dark surfaces like tundra and ocean. This algorithm is suitable for low and mid-latitude areas and some areas in high latitudes. It uses AVHRR images in channels 1, 3, and 4 to retrieve cloud optical depth, effective radius, and cloud top temperature.

(2) The other algorithm is for retrieval of clouds over bright surfaces like snow and ice. This algorithm is specifically designed for arctic regions where large scale snow cover exists most of the time throughout a year. This algorithm uses AVHRR images in channels 2, 3, and 4.

(3) Both algorithms are based on a comprehensive radiation model including a multi-stream radiative transfer code, DISORT, which handles multiple scattering processes accurately and efficiently.

(4) Bidirectional reflection is taken into account in the algorithm designed to retrieve clouds over bright snow/ice surfaces. As indicated from Figure 5.6, the bidirectional reflection function for snow/ice deviates significantly from that of a Lambert reflector, i.e. an isotropic reflector. Accounting for bidirectional reflectance of snow does improve the quality of the retrieval algorithm as compared

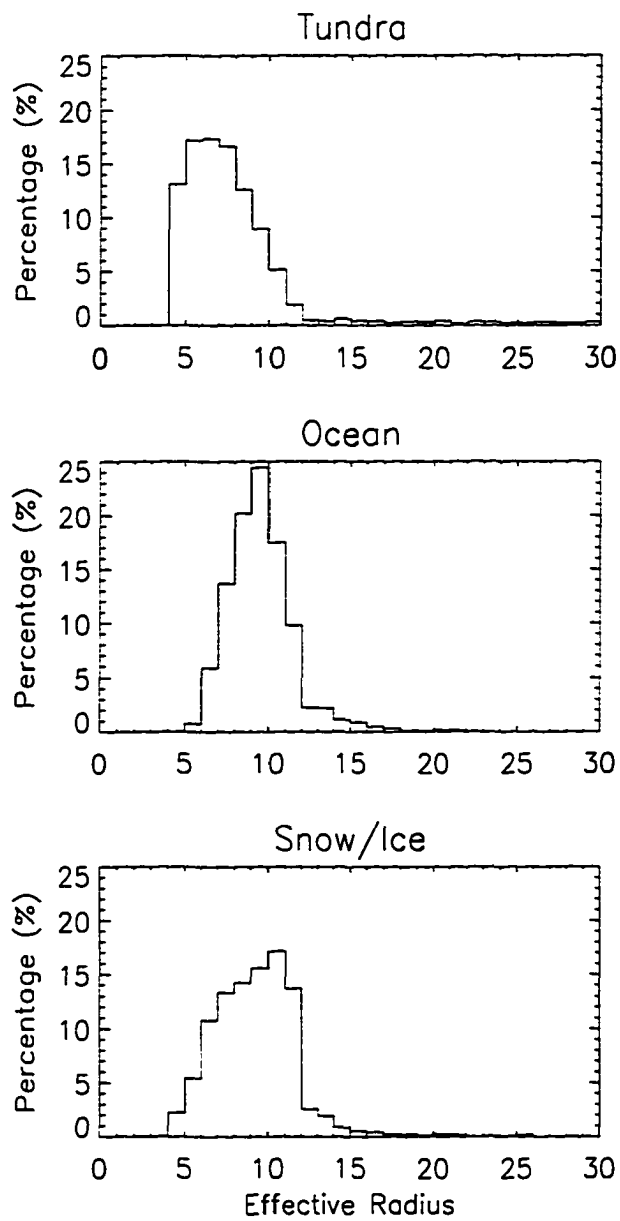


Figure 5.20 Frequency distributions of cloud effective radius (in μm) based on the data shown in Figure 5.15-5.17 for tundra, ocean, and snow as underlying surfaces, respectively.

with the Lambertian approximation.

(5) The surface albedo is accurately retrieved with both algorithms. For the tundra case, the surface albedo is retrieved through AVHRR channel 1 radiance observed under clear sky conditions. For bright snow/ice surfaces, the snow grain size is retrieved through AVHRR channel 2 radiance under clear sky conditions.

(6) From a careful sensitivity analysis, it is found that the retrieval results are reliable for clouds with optical depth $\tau > 3$ and effective radius $r_e > 3\mu m$. When $\tau < 3$ or $r_e < 3\mu m$, a small error in the radiance observation and surface reflectance may result in very large errors in the retrieval results.

(7) The quality of the retrieval results from the algorithm applicable to bright surfaces is more sensitive to uncertainties in the observed radiance and the radiative transfer model than those for dark surfaces.

To test the algorithms, the retrieved cloud parameters are used in the radiative transfer model to compute downwelling radiance at the surface, and the results are compared with ground-based irradiance measurements obtained at the NOAA CMDL facility in Barrow, Alaska. The retrieved cloud top temperature is also compared to cloud top temperature derived from ground-based radiosonde sounding data. These comparisons show that:

(1) From 17 cases of clouds over tundra, the bias is small, being 5.8 Wm^{-2} , which indicates a good agreement between the retrieval results and ground observations.

(2) From 12 cases of clouds over snow/ice, the bias is -5.1 Wm^{-2} , which shows a good agreement between the retrieval and observations. The higher standard deviation than for the tundra cases indicates larger error in the retrieved cloud

parameters.

(3) From the 9 cases for comparison of cloud top temperature, the standard deviation and bias are 2.4°K and 0.03°K , respectively, which shows a good agreement between the retrieval cloud top temperature and the sounding data.

To illustrate the utility of our retrieval algorithms, we have analyzed AVHRR images taken over the North Slope of Alaska and the Chukchi Sea for various types of underlying surfaces to retrieve surface reflectance and cloud parameters. These results show that

(1) For a tundra surface (area III), channel 1 albedo is around 0.05 when solar zenith angle is about 53° . Snow grain radius is found to be around $1000\ \mu\text{m}$ for the specific time and location (area II).

(2) It is found that water cloud droplet radii generally increase with optical thickness for optically thinner clouds ($\tau < 20$) and decrease for optically thicker clouds. From the cases shown in this study, clouds over the ocean have a slightly negative correlation between these two quantities. Clouds over the tundra have a clearly positive correlation between the two. Cloud over snow/ice, for which τ has a wider range than for ocean and tundra, have a positive correlation between the τ and r_e when $\tau < 20$ and a very weak negative correlation when $\tau > 20$.

(3) In the specific case selected for cloud parameter retrieval, the effective radius of clouds over tundra lies between 4 and $11\ \mu\text{m}$, with a peak value of 18% at $r_e = 7 \sim 8\ \mu\text{m}$. Over the ocean, the droplet size is slightly larger, lying between 6 and $12\ \mu\text{m}$ with a peak value close to 25% occurring at $r_e = 9 \sim 10\ \mu\text{m}$, which is consistent with that in mid and low-latitudes. Over snow/ice, the effective radius lies between 5 and $12\ \mu\text{m}$, and the peak value of 17% occurs at $r_e = 10 \sim 11$

μm . The retrieved cloud effective radius is generally smaller than at mid and low-latitudes.

Chapter 6

Summary and Discussion

The main contributions of this study may be summarized as follows:

(1) A numerical model based on a rigorous multiple scattering code (DISORT) is developed to compute the bidirectional reflectance of planetary surfaces. This model is compared to Hapke's model which assumes an isotropic phase function for multiple scattering based on the two-stream approximation. In our formulation, the phase function and the number of streams can be arbitrary, so that these restrictions that apply to Hapke's model are entirely recovered. In our numerical model, the opposition effect is taken into account in the same way as in Hapke's analytical bidirectional reflectance model. The comparison of the bidirectional reflectance obtained by the two models shows a significant difference when the single scattering albedo is large and the phase function is strongly forward-peaked, which is the case for snow/ice surfaces. Therefore, our model allows for a more realistic treatment of the snow/ice surfaces which are present persistently in the Arctic.

(2) An algorithm is developed to retrieve broadband surface albedo and solar irradiances from satellite observed narrowband radiances. The algorithm is different from the traditional methods based on empirical anisotropic corrections. Instead, it relies on a comprehensive radiative transfer model in which radiative transfer simulations are carried out by the DISORT code applicable to a plane-parallel atmosphere. The surface property is adjusted in the model calculation until the resultant TOA radiance matches the satellite observations. No *ad hoc* “anisotropic correction” is necessary. Bidirectional reflectance is accounted for when the underlying surface is covered by snow.

(3) The retrieved surface albedo and surface irradiances are compared with ground-based observations. In general, there is good agreement between the retrieval results and the observations. It is found that accounting for the bidirectional reflectance of the underlying snow surface significantly improves the quality of the overall retrieval results. For a snow surface, accounting for the bidirectional reflectance appears to give a significant advantage over the Lambertian assumption that is commonly adopted.

(4) Two algorithms are developed for retrieval of cloud optical depth, effective radius, and cloud top temperature. One of algorithms is for clouds over dark surfaces such as tundra and ocean. It is suitable for high latitudes as well as low- and mid-latitudes. The other algorithm is for clouds over bright surfaces like snow and ice. This algorithm takes bidirectional reflection into account for the underlying surface, which yields better quality than the Lambertian approximation. At center of both algorithms is a comprehensive radiation model including a multi-stream radiative transfer code (DISORT). It is found through a careful sensitivity study

that the algorithms are reliable when the clouds optical depth is larger than 3 and the cloud effective radius is larger than $3 \mu\text{m}$.

(5) To test the algorithms for retrieval of cloud parameters, the retrieved cloud parameters are used in the radiative transfer model to compute downwelling radiance at the surface, and the results are compared with ground based observations. It is found that good agreement exists between the two, which is an indirect test of our cloud retrieval algorithms.

(6) To illustrate the utility of the cloud retrieval algorithms, we analyze AVHRR images taken over the North Slope of Alaska and the Chukchi Sea for various types of underlying surfaces to retrieve the cloud parameters. It is found for the limited set of data analyzed that the cloud effective radius generally increases with optical thickness for optically thinner clouds ($\tau < 20$) and decreases for optically thicker clouds ($\tau > 20$). In the case selected in chapter 5, the cloud effective radius in the Arctic is found to be slightly smaller than the average effective radius reported for low- and mid-latitudes. Clouds over the ocean seem to have a larger average droplet size than clouds over tundra, while the average droplet size of clouds over snow/ice lies between those of clouds over ocean and over tundra.

It should be noted that the theoretical basis of all the physical models and retrieval algorithms developed in this study is DISORT, a rigorous numerical multiple scattering code. DISORT includes all physical processes such as scattering, absorption, thermal emission, and incident external sources at the upper boundary, as well as bidirectional reflection and thermal emission at the lower boundary. DISORT's ability to return radiance and flux at multiple user-defined levels, zenith and azimuth angles imply that it can return a lot of information in a single execu-

tion. DISORT is an accurate radiative transfer algorithm that can handle arbitrary scattering phase function and number of streams. It is a numerically stable code that is well-tested (*Stamnes et al*, 1988). All the retrieval algorithms developed in this study are based on complete physical models, and none of the empirical corrections that are commonly used in previous studies are adopted in this thesis.

It should also be mentioned that the retrieval algorithms for cloud parameters developed in chapter 5 are applicable only to plane-parallel, single water cloud layer. In the presence of multiple cloud layers, the physical process is more complicated, and needs further studies. In the presence of ice clouds, which occur quite frequently in the winter in the Arctic, a more advanced algorithm is necessary. These complications and challenges should be addressed in future studies.

Future work should also include direct testing of the cloud retrieval algorithms by using aircraft measurements of cloud properties such as those collected in the BASE (Beaufort and Arctic Storms Experiment) and those planned in conjunction with SHEBA (Surface HEat Budget of the Arctic Ocean) and the NASA's FIRE-III experiment to be conducted in collaboration with DOE's North Slope of Alaska Atmospheric Radiation Measurement (ARM) Program. These field campaigns will allow us to quantify better retrieval accuracies for individual parameters as well as the combined accuracy of radiative flux estimates.

Satellite remote sensing may provide global scale observations while ground-based observations are generally localized to small areas, but they may provide very reliable direct measurements with high temporal resolution. The retrieval algorithms for surface albedo and cloud parameters developed in chapters 4 and 5 are all based on satellite observations such as AVHRR images in several channels.

They are all tested against ground-based observations which are known to be reliable.

The retrieval algorithms developed in this thesis can be utilized to study the cloud and surface properties and radiation energy budget in arctic region as well as the entire globe. There is an abundant satellite remote sensing image database available. By applying the algorithms to this huge database we may enhance our understanding of the radiative energy balance on a global scale.

References

- Ahmad, S. P., and D. W. Deering, A simple analytical function for bidirectional reflectance, *J. Geophys. Res.*, *97*, 18,867, 1992.
- Albrecht, B. A., Aerosols, cloud microphysics and fractional cloudiness, *Science*, *245*, 1227-1230, 1989.
- Arking, A., and J. D. Childs, Retrieval of cloud cover parameters from multispectral satellite images, *J. Climate Appl. Meteor.*, *24*, 322, 1995.
- Asano, S., On the discrete ordinates method for the radiative transfer, *J. Meteor. Soc. Japan*, *53*, 92, 1975.
- Barnsley, M. J., A. H. Strahler, K. P. Morris, and J-P. Muller, Sampling the surface bidirectional reflectance distribution function (BRDF): 1. Evaluation of current and future satellite sensors, *Remote, Sens. Rev.*, *8*, 271, 1994.
- Blanchet, J. and R. List, Estimation of optical properties of arctic haze using a numerical model, *Atmos.-Ocean*, *21*, 444-465, 1983.
- Brest, C. L. and W. B. Rossow, Radiometric calibration and monitoring of NOAA AVHRR data for ISCCP, *Int. J. Remote Sensing*, *13*, 235-273, 1992.
- Chandrasekhar, C., *Radiative Transfer*, Oxford Univ. Press, 1960.
- Curran, and M. L. Wu, Skylab near-infrared observations of clouds indicating super-cooled liquid water droplets, *J. Atmos. Sci.*, *39*, 635, 1982.
- Curry, J. A., and G. F. Herman, Infrared radiative properties of summertime arctic stratus clouds, *J. Appl. Meteor.*, *24*, 525-538, 1985.
- De Abreu, R. A., J. Key, J. A. Maslanik, M. C. Serreze and E. F. LeDrew, Comparison of in situ and AVHRR-derived broadband albedo over Arctic sea ice, *Arctic*, *47*, 288-297, 1994.
- Durkee, P. A., Observations of aerosol-cloud interactions in satellite-detected visible and near-infrared radiance, *Proc. Symposium on the Role of Clouds in Atmospheric Chemistry and Global Climate*, American Meteorological Society, Anaheim, CA, 157, 1989.

- Dutton, G. E. and J. R. Christy, Solar radiative forcing at selected locations and evidence for global lower tropospheric cooling following the eruptions of El Chichón and Pinatubo, *Geophys. Res. Lett.*, *19*, 2313-2316, 1992.
- Esposito, L., Extensions to the classical calculation of the effect mutual shadowing in diffuse reflection, *Icarus*, *39*, 69, 1979.
- Foot, J. S., Some observations of the optical properties of clouds I, Stratocumulus, *Quart. J. Roy. Meteor. Soc.*, *114*, 129, 1988.
- Foot, J. S., P. Hignett, and C. G. Kilsby, Investigations into errors associated with upward-facing pyranometers fitted to the MRF Hercules, *MRF Internal Note No. 31*, 1986.
- Forster, P. M. F. and K. P. Shine, A comparison of two radiation schemes for calculating ultraviolet radiation, *Q. J. R. Meteor. Soc.*, *121*, 1113-1131, 1995.
- Grenfell, T. C. and D. K. Perovich, Spectral albedos of sea ice and incident solar irradiance in the southern Beaufort Sea, *J. Geophys. Res.*, *89*, 3573-3580, 1984.
- Han, Q., W. B. Rossow, and A. A. Lacis, Near-global survey of effective droplet radius in liquid water clouds using ISCCP data, *J. Climate*, *7*, 465, 1994.
- Han, W., Z. Jin and K. Stamnes, A model study on predicting surface bidirectional reflectances, *EOS (Am. Geophys. Union)*, 1993.
- Hansen, J. E., and J. B. Pollack, Near-infrared light scattering by terrestrial clouds, *J. Atmos. Sci.*, *27*, 265, 1970.
- Hapke, B., A theoretical photometric function for the lunar surface, *J. Geophys. Res.*, *68*, 4571, 1963.
- Hapke, B., Bidirectional reflectance spectroscopy, 1. Theory, *J. Geophys. Res.*, *86*, 3039, 1981.
- Hapke, B., Bidirectional reflectance spectroscopy, 3. Correction for macroscopic roughness, *Icarus*, *59*, 41, 1984.
- Hapke, B., Bidirectional reflectance spectroscopy, 4. The extinction coefficient and the opposition effect, *Icarus*, *67*, 264, 1986.
- Hapke, B., *Theory of Reflectance and Emittance Spectroscopy*, Cambridge Univ. Press, 1993.
- Hu, Y. X., and K. Stamnes, An accurate parameterization of the radiative properties of water clouds suitable for use in climate models, *J. Climate*, *6*, 728, 1993.
- Kaufman, Y. J. and B. N. Holben, Calibration of the AVHRR visible and near-IR bands by atmospheric scattering, ocean glint, and desert reflection, *Int. J. Remote Sensing*, *14*, 21-52, 1993.
- Key, J., The Cloud and Surface Parameter Retrieval (CASPR) System for Polar AVHRR, Version 1.0: User's Guide, Department of Geography, Boston University, Boston, 73pp,

- 1996.
- Key, J., Retrieval of cloud optical depth and particle effective radius at high latitudes using visible and thermal satellite data, *Passive Infrared Remote Sensing of Clouds and the Atmosphere 3*, 1995.
- Key, J., and M. Haefliger, Retrieval of ice surface temperature, outgoing longwave radiation, and cloud cover from AVHRR data, *World Climate Research Program, Sea Ice and Climate*, edited by E. Raschke, H. Cattle, P. Lemke, and W. Rossow, appendix C, p. 22, 1991.
- Kidwell, K. B., NOAA polar orbiter data users guide. NOAA/NESDIS/NCDC, Washington, D.C., 20233, U.S.A., 1995.
- King, M. D., Determination of the scaled optical thickness of clouds from reflected solar radiation measurements, *J. Atmos. Sci.*, *44*, 1734, 1987.
- Lauritson, L. G., Nelson, G. J., and F. W. Porto, Data Extraction and Calibration of TIROS-NOAA Radiometers, *NOAA Tech. Memo NESS*, 107, 1979.
- Leaitch, W. R., J. W. Strapp, H. A. Wiebe, and G. A. Isaac, Measurements of scavenging and transformation of aerosol inside cumulus. *Precipitation Scavenging, Dry Deposition, and Resuspension*, H. R. Pruppacher, R. G. Semonin and W. G. N. Slinn, Eds., Elsevier, 53-66, 1983.
- Li, Z., H. G. Leighton, M. Kasuhiko, and T. Takashima, Estimation of SW flux absorbed at the surface from TOA reflected flux, *J. Climate*, *6*, 317-370, 1993.
- Li, S., A model for the anisotropic reflectance of pure snow, Master dissertation, Department of Geography, Univ. of California, Santa Barbara, 1992.
- Liou, K. N., A numerical experiment on Chandrasekhar's discrete-ordinate method for radiative transfer, Application to cloudy and hazy atmosphere, *J. Atmos. Sci.*, *30*, 1303, 1973.
- Lubin, D., P. Ricchiazzi, C. Gautier, and R. H. Whritner, A method for mapping Antarctic surface ultraviolet radiation using multispectral satellite imagery, *Amer. Geophys. Union Antarct. Res. Ser.*, *62*, 53-81, 1994.
- McClatchey, R. A., R. W. Fenn, J. E. A. Selby, F. E. Volz, and J. S. Garing, Optical properties of the atmosphere. Air Force Cambridge Rep. AFCRL-71-0279, 85 pp, 1971.
- Myneni, R. B., and E. T. Kanemasu, The hot-spot of vegetation canopies, *J. Quant. Spectrosc. Radiat. Transfer*, *40*, 165, 1988.
- Mugnai, A., and W. J. Wiscombe, Scattering of radiation by moderately nonspherical particles, *J. Atmos. Sci.*, *37*, 1291, 1980.
- Nakajima, T., and M. D. King, Determination of the optical thickness and effective particle radius of clouds from reflected solar radiation measurements, Part I, theory, *J. Atmos. Sci.*, *47*, 1873, 1990.

- Nakajima, T., M. D. King, J. D. Spinhirne and L. F. Radke, Determination of the optical thickness and effective particle radius of clouds from reflected solar radiation measurements, Part II, Marine stratocumulus observations, *J. Atmos. Sci.*, *48*, 728, 1991.
- Nakajima, T. Y., and T. Nakajima, Wide-area determination of cloud microphysical properties from NOAA AVHRR measurements for FIRE and ASTEX regions, *J. Atmos. Sci.*, *52*, 4043, 1995.
- Penndorf, R., Tables of the refractive index for standard air and the Rayleigh scattering coefficient for the spectral region between 0.2 and 20 μm and their application to atmospheric optics. *Opt. Soc. Am.*, *47*, 176-182, 1957.
- Pinker, R. T., and I. Laszlo, Modeling surface solar irradiance for satellite applications on a global scale, *J. Appl. Meteor.*, *31*, 194-211, 1992.
- Pinty, B., M. M. Verstraete, and R. E. Dickinson, A physical model for predicting bidirectional reflectances over bare soil, *Remote Sens. Environ.*, *27*, 273, 1989.
- Platnick, S., and S. Twomey, Determining the susceptibility of cloud albedo to change in droplet concentration with the Advanced Very High Resolution Radiometer, *J. Appl. Meteor.*, *33*, 334, 1994.
- Platnick, S., and F. P. J. Valero, A validation study of a satellite cloud retrieval during ASTEX, *J. Atmos. Sci.*, *52*, 2985, 1995.
- Rao, C. R. N. and J. Chen, Inter-satellite calibration linkages for the visible and near-infrared channels of the Advanced Very High Resolution Radiometer on the NOAA-7, -9, and -11 spacecraft, *Int. J. Remote Sensing*, *16*, 1931-1942, 1995.
- Rawlins, F., and J. S. Foot, Remotely sensed measurements of stratocumulus properties during FIRE using the C130 aircraft multichannel radiometer, *J. Atmos. Sci.*, *47*, 2488, 1990.
- Rosow, W. B., L. C. Gardner, and A. A. Lacis, Global seasonal cloud variations from satellite radiation measurements, Part i, Sensitivity of analysis, *J. Climate*, *2*, 419, 1989.
- Roujean, J. L., M. Leroy, A. Podaire, and P. Y. Deschamps, Evidence of surface reflectance bidirectional effects from a NOAA/AVHRR multi-temporal data set, *Int. J. Remote Sensing*, *13*, 685, 1992.
- Sabins, F. F., Jr., *Remote Sensing Principles and Interpretation*, 1987.
- Samuelson, R. E., The thermal radiation field emitted by anisotropically scattering cloudy planetary atmospheres, *Icarus*, *10*, 258-273, 1969.
- Saunders, R. W., The determination of broad band surface albedo from AVHRR visible and near-infrared radiances, *Int. J. Remote Sensing*, *11*, 49-67, 1990.
- Saunders R. W., and J. A. Barnes, Intercomparison flights of pyranometers and pyge-

- ometers on the c-130, *MRF Internal Note No. 56*, 1991.
- Shaw, G., Atmospheric turbidity in the polar regions, *J. Appl. Meteor.*, *21*, 1080-1088, 1982.
- Shettle E. P. and R. W. Fenn, Models of atmospheric aerosols and their optical properties, in Agard Conference Proceedings No. 183, *Optical Propagation in the Atmosphere*, AGARD-CP-183, NTIS, ADA 028615, 1976.
- Stamnes, K., The theory of multiple scattering of radiation in plane parallel atmospheres, *Rev. Geophys.*, *24*, 299, 1986.
- Stamnes, K., and R. A. Swanson, A new look at the discrete ordinate method for radiative transfer calculations in anisotropically scattering atmospheres. *J. Atmos. Sci.*, *38*, 387, 1981.
- Stamnes, K., and H. Dale, A new look at the discrete ordinate method for radiative transfer calculations in anisotropically scattering atmospheres. II: Intensity Computations, *J. Atmos. Sci.*, *38*, 2696, 1981.
- Stamnes, K., and P. Conklin, A new multi-layer discrete ordinate approach to radiative transfer in vertically inhomogeneous atmospheres, *J. Quant. Spectrosc. Radiat. Transfer*, *31*, 273, 1984.
- Stamnes, K. and S.-C. Tsay, Optimum spectral resolution for computing atmospheric heating and photodissociation rates, *Planet. Space Sci.*, *38*, 807-820, 1990.
- Stamnes, K., S. C. Tsay, W. Wiscombe, and K. Jayaweera, Numerically stable algorithm for discrete-ordinate-method radiative transfer in multiple scattering and emitting layered media, *Applied Optics*, *24*, 2502, 1988.
- Stuhlmann, R. and P. Bauer, Retrievals of radiation from satellite data and aircraft measurements, in 'Workshop on Polar Radiation Fluxes and Sea-Ice Modelling, November 5-8, 1991, Bremerhaven, Germany', 29-40, Appendix C.
- Suttles, J. T., R. N. Green, P. Minnis, G. L. Smith, et al., Angular radiation models for earth atmosphere system, *NASA reference Publication 1184*, 143, 1988.
- Taylor, V. R. and L. L. Stowe, Atlas of reflectance patterns for uniform earth and cloud surfaces (NIMBUS-7/ERB-61 days). NOAA Technical Report NESDIS 10. 66p. 1984.
- Teillet. P. M., P. N. Slater, Y. Ding, R. P. Santer, R. D. Jackson, and M. S. Moran, Three methods for the absolute calibration of the NOAA AVHRR sensors in-flight. *Remote Sens. Environ.*, *31*, 105-120, 1990.
- Thomas, G. E., and K. Stamnes, *Radiative Transfer in Atmosphere and Ocean*, Cambridge Univ. Press, in press, 1996.
- Tsay S.-C., and M. D. King, Remote sensing and retrieval of surface bi-directional reflectance, *Eighth Conference on Atmospheric Radiation*, 406, 1994.
- Tsay, S.-C., K. Stamnes and K. Jayaweera, Radiative energy budget in the cloudy and

- hazy Arctic, *J. Atmos. Sci.*, *46*, 1002-1018, 1989.
- Tsay, S.-C., K. Stamnes and K. Jayaweera, Radiative transfer in stratified atmospheres: development and verification of a unified model, *J. Quant. Spectrosc. Radiat. Transfer*, *43*, 133-148, 1990.
- Turco, R. P., R. C. Whitten and O. B. Toon, Stratospheric aerosols: observation and theory, *Rev. Geophys. and Space Phys.*, *20*, 233-279, 1982.
- Twomey, S., and T. Cocks, Spectral reflectance of clouds in the near-infrared: Comparison of measurements and calculations. *J. Meteor. Soc. Japan*, *60*, 583, 1982.
- Twomey, S., and T. Cocks, Remote sensing of cloud parameters from spectral reflectance in the near-infrared, *Beitr. Phys. Atmos.*, *62*, 172, 1989.
- Valero, F. R. J., T. P. Ackerman and W. J. Y. Gore, Radiative effects of the arctic haze, *Geophys. Res. Lett.*, *10*, 1184-1187, 1983.
- van de Hulst, H. C., *Light Scattering by Small Particles*, John Wiley, New York, 1957.
- Verstraete, M. M., B. Pinty, and R. E. Dickinson, A physical model of the bidirectional reflectance of vegetation canopies, 1, Theory, *J. Geophys. Res.*, *95*, 11,755, 1990.
- Wang, P. and J. Lenoble, Comparison between measurements and modelling of UV-B irradiance for clear sky - a case study, *Appl. Opt.*, *33*, 3964-3971, 1994.
- Warren, S. G., Optical properties of snow, *Rev. Geophys. Space Phys.*, *20*, 67-89, 1982.
- Warren, S. G. and W. J. Wiscombe, A method for the spectral albedo of snow. 2: Snow containing atmospheric aerosols, *J. Atmos. Sci.*, *37*, 2734-2745, 1980.
- Warren, S. G., T. C. Grenfell, and P. C. Mullen, Optical properties of Antarctic snow, *Antarct. J. U. S.*, *21*, 247-248, 1986.
- Wiscombe, W. J. and S. G. Warren, A model for the spectral albedo of snow. 1: Pure snow, *J. Atmos. Sci.*, *37*, 2712-2733, 1980.
- Zeng, J., R. McKenzie, K. Stamnes, M. Wineland and J. Rosen, Measured UV spectra compared with discrete ordinate method simulations, *J. Geophys. Res.*, *99*, 23019-23030, 1994.